

Exclusive scattering off the deuteron

Dissertation
zur Erlangung des Doktorgrades
des Department Physik
der Universität Hamburg

vorgelegt von
Daniela Amrath
aus Viersen

Hamburg 2007

Gutachter der Dissertation:	Dr. M. Diehl Prof. Dr. J. Bartels
Gutachter der Disputation:	Dr.M.Diehl Prof. Sigl
Datum der Disputation:	11. Dezember 2007
Vorsitzender des Prüfungsausschusses:	Dr. H. D. Rüter
Vorsitzender des Promotionsausschusses:	Prof. Dr. G. Huber
Dekan der Fakultät MIN:	Prof. Dr. A. Frühwald

Abstract

Exclusive processes are a special class of processes giving insight into the inner structure of hadrons. In this thesis we consider two exclusive processes and compute their total cross sections as well as the beam charge and beam polarization asymmetries for different kinematical constraints. These calculations offer the opportunity to get access to the nonperturbative GPDs. Theoretically they can be described with the help of models. The first process we investigate contains a GPD of the pion, which is basically unknown so far. We include different models and make predictions for observables that could in principle be measured at HERMES at DESY and CLAS at JLab. The second process we consider is electron-deuteron scattering in the kinematical range where the deuteron breaks up into a proton and a neutron. This can be used to investigate the neutron, which cannot be taken as a target due to its lifetime of approximately 15 minutes. For the calculation of the electron-deuteron cross section we implement models for the proton and neutron GPDs. Once there are experimental data available our calculations are ready for comparison.

Zusammenfassung

Exklusive Prozesse sind Prozesse, die einen Einblick in die innere Struktur von Hadronen ermöglichen. In dieser Arbeit betrachten wir zwei exklusive Prozesse und berechnen deren totale Wirkungsquerschnitte, sowie Asymmetrien bezüglich der Ladung und der Polarisation des Elektronen- (Positronen-) Strahls für verschiedene kinematische Bedingungen. Durch diese Rechnungen erhält man einen direkten Zugang zu den GPDs. Dabei handelt es sich um nicht perturbative Objekte, die man mit Hilfe von Modellen beschreiben kann. Der erste Prozess, den wir untersuchen enthält eine Pion GPD, welche bisher theoretisch wie experimentell weitestgehend unbekannt ist. Wir untersuchen verschiedene Modelle um Vorhersagen für Observablen zu machen, welche man prinzipiell bei HERMES am DESY und CLAS am JLab messen kann. Im zweiten Prozess betrachten wir Elektron-Deuteron Streuung in einem kinematischen Bereich, in dem das Deuteron in ein Proton und ein Neutron aufbricht. Dieser Prozess kann zur Untersuchung des Neutrons benutzt werden, welches auf Grund seiner kurzen Lebensdauer von etwa 15 Minuten, nicht als Target zur Verfügung steht. Für die Berechnung des Elektron-Deuteron Streuquerschnitts verwenden wir Modelle für die Proton und Neutron GPDs. Sobald experimentelle Daten zur Verfügung stehen, können unsere Ergebnisse mit diesen verglichen werden.

Contents

Introduction	1
1 General framework	7
1.1 Basic kinematics and scattering processes	7
1.1.1 Elastic scattering	7
1.1.2 Deep inelastic scattering and parton distribution functions	9
1.1.2.1 Factorization in inclusive processes	13
1.1.2.2 Evolution in inclusive processes	13
1.1.3 Hard exclusive scattering processes	14
1.1.3.1 A few words on factorization and evolution in exclusive processes	15
2 Generalized parton distribution functions	17
2.1 Definition of GPDs	17
2.1.1 Nucleon GPDs	17
2.1.2 Pion GPD	19
2.2 Limits	19
2.3 Form factors and polynomiality	20
2.4 Double distributions	22
2.5 Access to GPDs via DVCS and weak currents	25
2.5.1 Deeply virtual Compton scattering	25
2.5.2 Weak current hadronic amplitude in deeply virtual scattering	28
2.5.3 Total scattering amplitude	29
2.5.4 DVCS and Bethe–Heitler	35
2.5.5 Isospin	35
3 Scattering off a virtual pion	39
3.1 The $ep \rightarrow e' \pi \gamma n$ process	40
3.1.1 Electron-proton center-of-mass frame	40
3.1.2 Kinematics for the $\pi \gamma \rightarrow \pi' \gamma'$ subprocess	45
3.2 Four particle phase space integral	47
3.3 The $e\pi \rightarrow e' \pi' \gamma$ subprocess	51
3.3.1 Kinematics for the electron-pion subprocess	51
3.3.2 Squared amplitude of $e\pi \rightarrow e' \pi' \gamma$	52
3.3.2.1 DVCS amplitude	53
3.3.2.2 Backward scattering and transition distribution amplitudes	54
3.3.2.3 Bethe–Heitler amplitude	55

3.3.2.4	Interference term	56
3.4	Hadronic part of $ep \rightarrow e' \pi \gamma n$	57
3.5	Differential cross section for the process $ep \rightarrow e' \pi \gamma n$	58
3.6	Models for the pion GPD	58
3.6.1	Pion PDFs	60
3.6.2	Pion form factor	61
3.7	Experimental extraction	63
3.8	Theoretical and kinematical cuts for HERMES and CLAS	64
3.8.1	Pion and photon in the proton laboratory frame	67
3.9	Results for the cross section and measurable asymmetries	68
3.9.1	Results for HERMES	68
3.9.2	Results for JLab	70
4	Electron deuteron scattering	79
4.1	Basic properties of the deuteron	79
4.1.1	Magnetic moment of the deuteron	80
4.1.2	Electric quadrupole moment of the deuteron	81
4.2	Deuteron in exclusive processes	81
4.2.1	Kinematics	81
4.2.2	Deuteron GPDs	82
4.2.3	Deuteron form factors	83
4.2.4	Helicity amplitudes	84
4.3	Deuteron wave function	85
4.3.1	Deuteron potential	86
4.3.1.1	Argonne v_{18} potential	87
4.4	Deuteron state	88
4.5	Electron-deuteron cross section	90
4.6	Modeling nucleon GPDs	94
4.6.1	Unpolarized nucleon PDFs	94
4.6.2	Polarized nucleon PDFs	95
4.6.3	Nucleon Compton form factors	95
4.7	Theoretical and kinematical cuts for CLAS	96
4.8	Cross section results	97
5	Summary and outlook	103
A	Light-cone coordinates	105
B	Spherical harmonics	106
C	Details for PDF fits	107
	Bibliography	109
	Acknowledgements	119

Introduction

In an early picture of the beginning of the last century the atom is described as having a central small, but heavy nucleus surrounded by a light electron cloud. Evidence for that was given by Rutherford's scattering experiments, where α -particles are scattered off gold atoms. The theory describing the electromagnetic interaction between the electrons and the nucleus is Quantum Electrodynamics (QED). In scattering experiments similar to Rutherford scattering it was shown that the nucleus itself has a substructure and is composed of protons and neutrons. The proton [1, 2] was discovered first, followed by its charge-neutral partner, the neutron [3]. Both particles have spin- $\frac{1}{2}$ and can be treated as two different (isospin) states of the same particle, the nucleon.

After the discovery of the nucleons further particles were discovered, namely the positron (1932, [4]) and the muon (1937, [5, 6]) belonging to the class of leptons, followed by two mesons which were the pion (1947, [7]) and the kaon (1947, [8]). To further study reactions between elementary particles and produce new particles huge accelerators were build. Nowadays we know several hundred "elementary" particles.

It is now the aim of the theory of elementary particles to describe all arising phenomena relevant for these particles. Electric and magnetic properties can be described very well by the Maxwell equations. Moreover, gravitation and the electromagnetic force are known from classical physics. Two new forces were discovered arising from the weak and strong interactions. The weak interaction is for example responsible for the radioactive β -decay or proton-proton fusion in the sun and the strong interaction is responsible for example for the α -decay and nuclear forces.

Gravitation does not play a role in elementary particle physics since it is very weak, 10^{36} times weaker than the electromagnetic force. Both of these two forces have an infinite range whereas the weak and strong forces act over a short range only. The interaction range of the weak force is 10^{-18} m and of the strong force 10^{-15} m.

Particles are classified according to the interactions they take part in. Gravitation and the weak force act on all known particles. Those particles that also interact strongly are called hadrons. Hadrons themselves are divided into two subclasses – baryons, like the proton or the neutron which have a half-integer spin and mesons, like the pion or the kaon which have an integer spin.

The history of the strong interaction has its origin in the measurement of the magnetic moment of the proton using molecular hydrogen by Stern, Esterman and Frisch (see for example [?, ?]). At that time the electron, the photon and the proton were the only known elementary particles. It was a great triumph of the Dirac theory making a correct prediction for the magnetic moment of the electron within experimental errors. Using the knowledge of the Dirac theory a magnetic moment of the proton was predicted. Experiments were made by Stern *et al.*, but they did not measure the predicted value exactly. This showed that the proton

unlike the electron must have an inner structure. The deviation from the point-like structure can be measured and described by two functions, called form factors, giving the electric and magnetic distribution inside the proton. Two further form factors are given for the neutron. A new interaction had to be responsible for that. In addition to the two known interactions, gravity and the electromagnetic interaction, the strong interaction was introduced.

From deep inelastic electron-nucleon scattering (DIS) it arose that the nucleon is composed of point-like particles. It was Feynman who suggested the existence of this point-like particles inside the nucleon in order to be able to explain the DIS experiments [9]. These objects, which he called partons, were later on identified with quarks and gluons.

The quantum field theory describing the microscopic structure of strong interactions is Quantum Chromodynamics (QCD) [10]. It is a non-Abelian gauge theory and is used to explain the forces between hadrons as well as atomic nuclei. The theory is formulated in terms of quantum fields of quarks and gluons which are assumed to be the elementary constituents of the hadrons [11, 12, 13].

The strong interaction does not distinguish between protons and neutrons, which means the strong force is charge independent. If we neglect small mass differences of 1 – 5 MeV we see that protons and neutrons as well as the pions, π^+ , π^- and π^0 have the same mass, which means that they are degenerate states. In analogy to the hydrogen atom where degenerate states that differ only in the magnetic quantum number are ascribed to angular momentum invariance, it is obvious that the almost equality of the masses leads to an invariance group. In analogy to the spin this group is called isospin. The proton and the neutron build an isospin doublet while the three pions build an isospin triplet.

Another milestone in the evolution of the knowledge of the strong interaction came from particles showing a strange behavior: they are produced via the strong interaction but they decay via the weak interaction. This led to a new quantum number, strangeness. The strong and the electromagnetic interaction conserve strangeness, while the weak interaction violates strangeness. In addition to that hypercharge was defined, which is the sum of strangeness and baryon number. With isospin and hypercharge one had found a generating invariance group for the strong interaction. But this was not satisfying because no connection could be made between the properties of mesons and baryons. The decisive breakthrough was made by Gell-Mann and Ne'man [14, 15]. They classified hadrons according to the flavor SU(3)-group. For exact SU(3)-invariance all particles within a SU(3)-multiplet must have the same mass. The order of magnitude of the symmetry breaking was about 20% which was small enough to calculate these effects perturbatively. A great success of this theory was the prediction of the Ω^- which was discovered in 1964 [16]. The quark theory predicted that either quarks do not exist as free particles or particles do exist in nature which have a fractional charge. Until today there is no indication of fractional charge. But the quarks lead to another riddle. The Ω^- for example has spin- $\frac{3}{2}$ and is the lightest particle consisting of three strange quarks, each quark having spin- $\frac{1}{2}$. For reasonable potentials the spatial wave function is symmetric and the orbital angular momentum is zero. To obtain the spin of $\frac{3}{2}$ all quark spins have to be aligned leading to a total symmetric wave function for the Ω^- . But this contradicts the Pauli exclusion principle since the Ω^- is a fermion. Gell-Mann introduced a new degree of freedom for the quarks, called color. According to that each quark exists in three colors. Rotations in the color-space also build a SU(3)-group. Color SU(3) plays the fundamental role in the strong interaction [17].

In 1974 a new particle, the J/ψ , was discovered [18]. It has a mass of roughly 3.1 GeV and a width of only 60 keV, which can be explained in QCD by introducing a further quark, called

charm (c) quark. The J/ψ is a bound state of $c\bar{c}$. The charm quark was already predicted by Glashow [19] having a charge of $\frac{2}{3}$ like the up quark. Up (u) and down (d) quarks are those quarks the nucleons are composed of. Another quark entered the game when Υ was discovered [20] which is a $b\bar{b}$ state. Since then the b quark is known as the bottom or beauty quark. Theoretically it was supposed that one more quark should exist. This is the t quark, called top or truth quark. It has a mass of 174 GeV which is of the order of the mass of a gold atom. It took 18 more years until it was discovered in 1995 at the Fermi National Accelerator Laboratory [21].

In the same way, as the photon is a gauge field mediating the electromagnetic interaction between charged particles in the Abelian theory of QED, the non-Abelian gauge field mediates the color interaction in QCD. This non-Abelian field binds the quarks together and is therefore called gluon. Gluons carry color charge, in contrast to the charge-neutral photon, and can thus interact with each other, even in the absence of quarks. A fundamental characteristic of QCD is that quarks and gluons are not observed as free states. This experimental fact is called confinement. The composed hadrons are all color neutral. The first direct experimental evidence of gluons was found in 1979 when three-jet events were observed at the electron-positron collider PETRA at Deutsches Elektronen-Synchrotron (DESY) [?].

Among many achievements, the discovery of asymptotic freedom is very important [22, 23, ?]. The effective coupling constant α_s of QCD depends on the momentum transfer Q^2 of the photon, $\alpha_s = \alpha_s(Q^2)$. In contrast to the coupling constant α_{em} in QED, α_s decreases with Q^2 . This means that at hard scales (small distances) with $Q^2 \gg 1 \text{ GeV}^2$ the coupling α_s becomes very small, $\alpha_s \ll 1$. Therefore one can calculate observables by means of perturbation theory due to the small coupling, so the calculation can be performed in a straight forward way [24, 25]. At this energy scale the hadrons can be pictured to be composed of quasi-free partons, which is known as asymptotic freedom.

One of the most significant predictions of perturbative QCD is the scaling of the structure functions in deep inelastic scattering [26, 9], where the momentum transfer Q^2 and the energy transfer ν of electrons are very large while the ratio Q^2/ν is kept fixed. Bjorken claimed that the structure functions depend only on the ratio rather than on the two independent variables Q^2 and ν . This picture is known as Bjorken scaling [27]. Forthwith after his proposal this behavior was experimentally confirmed [28]. To understand this scaling behavior we assume that the projectile electrons scatter off almost free point-like partons. In DIS the momentum transfer Q^2 is large, so that the spatial resolution of the target nucleon is high. Therefore Bjorken scaling implies that the partons seem to be free and point-like when they are observed with high spatial resolution. Corrections to the Bjorken scaling introduce a logarithmic Q^2 -dependence. Bjorken scaling and its violations are very well established for electron-proton scattering.

However, if we turn our attention to a region where the energy scale is low, around 1 GeV^2 , which is the scale of a typical hadronic mass, the situation changes. The coupling becomes large, the powerful perturbation theory cannot be applied and the simple picture of a hadron in terms of QCD degrees of freedom does not hold anymore. Moreover, it is still unknown how quarks and gluons bind into hadrons. To unravel this puzzle a nonperturbative approach is inevitable.

Hard processes are the main experimental tool to investigate the inner structure of the hadrons. In these scattering experiments a target hadron is probed by an electron (or by a muon or a neutrino beam). The advantage of a lepton beam is that the lepton has no inner structure and does not interact strongly. A complication arises in hard scattering because hard

and soft parts enter the game. The quark interaction with the projectile at large momentum transfers can be described perturbatively in many hard processes while the quark structure of the target hadron is a nonperturbative object. Factorization theorems state that it is possible for several processes to separate the hard and the soft parts [29, 30, 31]. It was proven that the cross section for example for inclusive deep inelastic scattering and Drell-Yan (DY) processes or the physical amplitude for example in the case of deeply virtual Compton scattering (DVCS) [32] and hard exclusive meson production [30] can be represented in terms of a convolution of perturbatively calculable coefficient functions and nonperturbative objects. The soft, nonperturbative part is represented by parton distribution functions (PDFs) in inclusive processes and by generalized distribution functions (GPDs) in exclusive processes. The PDFs can be interpreted as probability functions describing how the momenta of the partons are distributed inside the nucleon. GPDs embody PDFs and form factors as limiting cases and contain a wealth of information on the quark and gluon structure of the nucleons. PDFs and GPDs are defined as hadronic matrix elements of partonic operators. A precise definition will be given in the course of this thesis. Although one cannot calculate PDFs and GPDs from QCD directly, factorization opens a door for the understanding of the hadronic substructure.

As mentioned, GPDs provide information on the inner structure of hadrons which cannot be accessed by inclusive measurements. GPDs and their behavior in deeply virtual Compton scattering were systematically investigated by the Leipzig group [33]. They developed a unified framework to describe the Dokshitzer-Gribov-Lipatov-Altarelli-Parisi (DGLAP, [34, 35, 36, 37, 38]) and Efremov-Radyushkin-Brodsky-Lepage (ERBL, [39, 40, 41]) evolution. When Ji and Radyushkin underlined the non-forward nature of parton distributions appearing in DVCS [32, 42, 43] and meson production [30] a large interest in GPDs started. In their publications it was shown that GPDs are connected to PDFs and form factors. GPDs have access to the total angular momentum carried by the partons. Up to now it is not completely solved to what extent the different partons contribute to the spin of the nucleon. GPDs offer an opportunity to further solve this spin puzzle. Moreover, a proof of factorization for meson electroproduction was given by Collins. A further key property of GPDs is that they provide the possibility to see the nucleon in a three dimensional picture, investigated by Burkardt [44].

The task is now to constrain GPDs. This is challenging since GPDs cannot be calculated perturbatively. Hence one has to resort to models or lattice calculations and fit them to available experimental data. But since observables contain not GPDs themselves but convolutions of GPDs with coefficient functions one faces a tremendously difficult problem of deconvolution. Furthermore high luminosities are required because the exclusive cross sections are rather small and detectors must be capable to ensure that the final state was exclusive.

In the following we provide a general framework in the first chapter. We introduce elastic and inelastic scattering processes.

In the second chapter we introduce the generalized parton distribution functions and show their connection to measurable objects. These can be parton distributions in a forward limit or form factors. Since GPDs are nonperturbative objects we exhibit a model approach. The concept of double distributions, as being the most important ansatz for modeling GPDs, will be given in detail. Eventually we will calculate the scattering amplitude of some exclusive processes. One exclusive process is DVCS where an electron emits a virtual photon which scatters off one parton inside the proton leading to a final state consisting of the scattered electron, a real photon and a recoil proton. In addition to that well-known process we will

replace the virtual photon by the different weak gauge bosons, which are the W^\pm and the Z^0 and unfold the differences in these reactions. By means of isospin symmetry quark distribution functions can be related to each other. This leads to combinations of spin and flavor quark distributions, which are important to finally determine the single quark distributions.

The third chapter deals with the process of electron-proton scattering $ep \rightarrow e\gamma\pi n$ where in a subprocess the virtual photon scatters off a virtual pion which is emitted from the proton. After introducing the relevant kinematics we show the complete calculation of this process. This includes the subprocess of deeply virtual Compton scattering off a pion which can be calculated as the similar process of DVCS off a proton. The computation of DVCS includes GPDs, therefore we will introduce models for the pion GPD. In the end we will give results for the cross sections depending on the chosen kinematical constraints. We will study the process for two experiments, HERMES at DESY and CLAS at Jefferson National Laboratory (JLab).

In Chapter four we take the deuteron into account. We calculate the process $ed \rightarrow e\gamma pn$. First we briefly discuss basic properties of the deuteron and introduce its GPDs and form factors as well as the deuteron wave function. Finally we obtain the differential cross section. The calculation of this electron-deuteron scattering process gives a direct access to nucleon GPDs, especially to the neutron GPD, which is not known very well. Thus we implement a model for these GPDs. We will give numerical results for the cross section for the CLAS detector at JLab after the planned 12 GeV upgrade.

Chapter 1

General framework

In this Chapter we outline some fundamental properties of scattering processes. We start by introducing form factors which parametrize the hadronic current in the cross section of elastic scattering processes. In a next step we consider inelastic scattering where parton distribution functions appear. These functions will be defined and discussed. Furthermore we will briefly mention factorization and evolution. In the last part of this chapter we will draw our attention to exclusive scattering processes.

1.1 Basic kinematics and scattering processes

One of the most important tools to get information on the hadron structure are scattering experiments. These experiments take place in large particle accelerators where such high energies can be achieved, that even the nucleon structure can be resolved. Many models can be compared to the extracted data from the experiments, helping to learn more about the inner structure of hadrons.

A very clean way of probing the nucleon structure is using an electron beam, because the electron is a point-like particle and interacts by means of the well-understood electromagnetic force. Therefore, electron-nucleon scattering plays a crucial role in the investigation of the nucleon structure.

1.1.1 Elastic scattering

We start here considering the simplest case of elastic scattering, where an electron scatters off a spinless particle as for example an atom. The information on the electromagnetic structure of a spinless target is contained in a form factor $F(Q^2)$. The four-momentum transfer between the initial and final electron is $q = p_e - p_{e'}$. Since q^2 is negative we use $Q^2 = -q^2$. The form factor is defined through the deviation from the elastic scattering cross section to the Mott cross section, which describes the scattering off the spin- $\frac{1}{2}$ electron off a spinless point charge with internal charge density distribution,

$$\frac{\sigma(Q^2)}{\sigma(Q^2)|_{\text{Mott}}} = |F(Q)|^2, \quad (1.1)$$

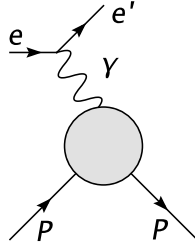


Figure 1.1: Elastic scattering of an electron off a proton. The blob is described by the nucleon form factors.

where the Mott cross section is given by

$$\sigma(Q^2)|_{\text{Mott}} = \left(\frac{Ze^2}{2E_e} \right)^2 \frac{\cos^2 \frac{\theta}{2}}{\sin^4 \frac{\theta}{2}}. \quad (1.2)$$

Here E_e is the incident electron energy, Z the atomic number of the target and θ the scattering angle in the rest frame of the target.

In a next step we consider a spin- $\frac{1}{2}$ particle, like the proton or the neutron being the target as shown in Fig. 1.1. To calculate the cross section we need the hadronic current, which has the general structure

$$J^\mu = \bar{u}(p')(p^\mu \Gamma_1 + p'^\mu \Gamma_2 + \gamma^\mu \Gamma_3)u(p), \quad (1.3)$$

where $\bar{u}(p')$ and $u(p)$ are the Dirac spinors of the nucleon and Γ_i are scalars that depend on the only nontrivial scalar Q^2 . The structure of the hadronic current has to be determined, conserving the Lorentz structure of the current. A term $\gamma_5 \gamma^\mu$ is ruled out due to parity conservation. It follows from current conservation $q_\mu J^\mu = 0$ that Γ_1 is equal to Γ_2 and $\Gamma_3 = 0$. Hence the only possible combination is $(p+p')^\mu$. Using the Gordon decomposition the hadronic current can be expressed as a linear combination of γ^μ and $\sigma^{\mu\nu} q_\nu$, with $\sigma^{\mu\nu} = \frac{i}{2}[\gamma^\mu, \gamma^\nu]$. The current can finally be parametrised in terms of two form factors $F_1(Q^2)$ and $F_2(Q^2)$

$$\bar{u}(p')\Gamma^\mu u(p) = \bar{u}(p') \left[F_1(Q^2)\gamma^\mu + \frac{1}{2m_N} F_2(Q^2) i\sigma^{\mu\nu} q_\nu \right] u(p), \quad (1.4)$$

where m_N is the mass of the nucleon [45]. The general coefficients $F_1(Q^2)$ and $F_2(Q^2)$ are called Dirac and Pauli form factors, respectively. They contain information about the electromagnetic structure of the nucleon.

In the static limit $Q^2 = 0$ the Dirac and Pauli form factors of the nucleon are normalized according to $F_1^p(0) = 1$, $F_1^n(0) = 0$, $F_2^p(0) = \kappa_p$ and $F_2^n(0) = \kappa_n$. $F_1^{p/n}(0)$ gives the charge of the nucleon and $F_2^{p/n}(0)$ its anomalous magnetic moment. The anomalous magnetic moments of the proton and the neutron are given by

$$\kappa_p = \mu_p - 1 = 1.792847351(28) \mu_N, \quad (1.5)$$

$$\kappa_n = \mu_n = -1.9130427(5) \mu_N, \quad (1.6)$$

both given in units of the nuclear magneton-units $\mu_N = \frac{e\hbar}{2m_N}$ [46]. In general it is more illuminating to use linear combinations of F_1 and F_2

$$G_E(Q^2) = F_1(Q^2) - \tau F_2(Q^2), \quad (1.7)$$

$$G_M(Q^2) = F_1(Q^2) + F_2(Q^2), \quad (1.8)$$

with $\tau = \frac{Q^2}{4m_N^2}$. The index E labels the electric and M the magnetic form factor, respectively. These functions are the so-called Sachs form factors. In the Breit frame, defined by $\vec{p}_p = -\vec{p}_{p'}$ the form factors G_E and G_M are related to the nucleon charge and magnetic momentum. They can be used to measure the electromagnetic size of the proton and the neutron. The values at $Q^2 = 0$ are

$$G_{E_p}(0) = 1, \quad G_{M_p}(0) = \mu_p, \quad (1.9)$$

$$G_{E_n}(0) = 0, \quad G_{M_n}(0) = \mu_n. \quad (1.10)$$

A technique to separate values for G_E^2 and G_M^2 is the Rosenbluth separation, therefore the electron-nucleon cross section measurements are needed for different electron scattering angles at a fixed value for Q^2 [46]. For $Q^2 < 2 \text{ GeV}^2$ the parametrizations for G_{E_p} , G_{M_p} and G_{M_n} are in excellent agreement with the available data in this Q^2 range

$$G_{E_p}(Q^2) = G_D(Q^2), \quad (1.11)$$

$$G_{M_n}(Q^2) = \mu_n G_D(Q^2), \quad (1.12)$$

$$G_{M_p}(Q^2) = \mu_p G_D(Q^2), \quad (1.13)$$

$$G_D(Q^2) = \frac{1}{(1 + Q^2/0.71 \text{ GeV}^2)^2}, \quad (1.14)$$

where $G_D(Q^2)$ is the dipole form factor.

An illustration of the quality of the dipole fits for G_{E_p} , G_{M_p} and G_{M_n} is given in [46] and is shown in Fig. 1.2.

F_1 and F_2 can be experimentally determined as functions of Q^2 . The electric form factor of the neutron is measured via electron-deuteron scattering. Preceded by a series of experiments, Glaster *et al* [47] measured elastic electron-deuteron cross sections up to $Q^2 = 0.6 \text{ GeV}^2$. Their fit is given by

$$G_{E_n}(Q^2) = -\frac{\tau\mu_N}{1 + 5.6\tau} G_{E_p}(Q^2). \quad (1.15)$$

The latest experiment measuring the electron-deuteron cross section having data up to $Q^2 = 0.7 \text{ GeV}^2$ by Platchkov *et al* [48] has significantly smaller uncertainties than all experiments before and the authors suggest the form

$$G_{E_n}(Q^2) = -a \frac{\tau\mu_N}{1 + b\tau} G_{E_p}(Q^2), \quad (1.16)$$

where a and b depend on the potential of the deuteron wave function.

1.1.2 Deep inelastic scattering and parton distribution functions

Hard processes are the most important tool to further investigate the inner structure of nucleons as well as other hadrons. These processes are divided into inclusive, semi-inclusive and

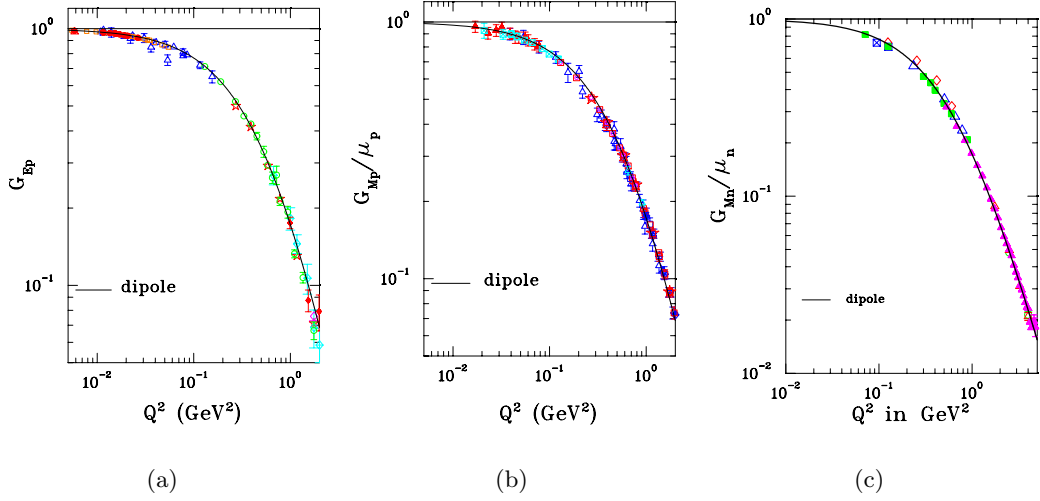


Figure 1.2: Quality of dipole fits, taken from [46], for a) $G_{E_p}(Q^2)$ including data from Refs. [49, 50, 51, 52, 53, 54, 55, 56, 57, 58] in the range $0.005 - 2 \text{ GeV}^2$, for b) $G_{M_p}(Q^2)$ including data from Refs. [49, 50, 52, 53, 54, 59, 60] and for c) $G_{M_n}(Q^2)$ including data from Refs. [61, 62, 63, 64, 65, 66, 67]

exclusive processes. In the inclusive case the nucleon can break up, starting from a certain threshold energy and decays, due to energy-momentum conservation, into an arbitrarily number of particles where only the scattered electron is detected while in the semi-inclusive case further particles are detected in coincidence. In exclusive processes all final-state particles have to be detected in coincidence, see Fig. 1.3.

We consider the process where an electron with momentum p_e is scattering off a proton with momentum p_p . In the one-photon approximation the electron emits a virtual photon of momentum p_q which scatters off a quark within the proton. Corrections due to multi-photon exchange are suppressed by α_{em} and will be neglected in this work. In the deep inelastic regime we consider the momentum transfer between the electrons, Q^2 , and $\nu = \frac{p_p \cdot p_q}{m_p}$, which

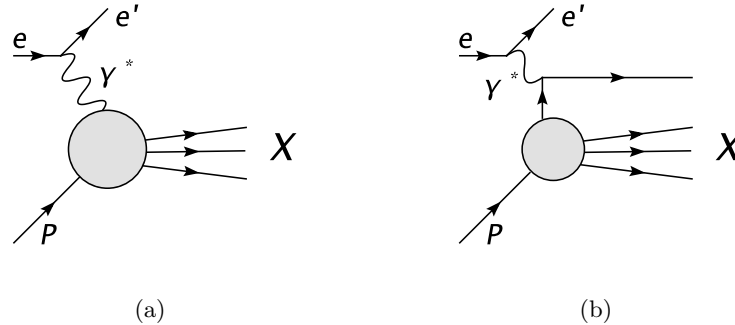


Figure 1.3: Inclusive scattering and its partonic picture. In the Bjorken limit the cross section can be approximated by the cross section of scattering off a parton convoluted with the PDF.

is connected to the energy loss of the electron in the proton rest frame, to be large compared to all other quantities. Unlike in elastic scattering there are two independent variables

$$Q^2 \quad \text{and} \quad \nu. \quad (1.17)$$

The invariant mass W of the final state system is connected to Q^2 and ν by

$$W^2 = (p_p + p_q)^2 = m_p^2 + 2m_p\nu - Q^2, \quad (1.18)$$

with $m_p = 938.3$ MeV. These two variables can be replaced by the dimensionless variables

$$x_B = \frac{Q^2}{2p_p p_q} \quad \text{and} \quad y = \frac{p_p \cdot p_q}{p_p \cdot p_e}. \quad (1.19)$$

The allowed range for the y is $0 < y < 1$ and for the Bjorken variable $0 < x_B < 1$ where elastic scattering corresponds to $x = 1$. The inclusive reaction $ep \rightarrow e'X$ is governed by Q^2 and ν and depends in the so-called Bjorken limit

$$Q \rightarrow \infty, \nu \rightarrow \infty \quad \text{and} \quad x_B \text{ fixed} \quad (1.20)$$

mainly on x_B . This feature was already known from scattering of point-like particles as electrons and muons and was the first hint that the nucleon is build of smaller point-like particles, so-called partons.

The general form of the cross section in leading order in α_{em} is given by

$$\frac{d\sigma}{d\Omega dE_{e'}} = \frac{\alpha^2}{Q^4} \frac{E_{e'}}{E_e} L_{\mu\nu} W^{\mu\nu}. \quad (1.21)$$

The leptonic tensor $L_{\mu\nu}$ can be calculated by means of perturbative QED and one obtains

$$L_{\mu\nu} = 2((p_{e'})_\mu (p_e)_\nu + (p_{e'})_\nu (p_e)_\mu - \delta_{\mu\nu} (p_e \cdot p_{e'} - m_e^2) + i\epsilon_{\mu\nu\rho\sigma} q^\rho q^\sigma). \quad (1.22)$$

The hadronic tensor $W^{\mu\nu}$ cannot be derived from first principles. It can be written in way without any information about the final state X which is in accordance with the experimental situation for inclusive measurements,

$$W^{\mu\nu} = \frac{1}{4m_p} \int \frac{d^4x}{2\pi} e^{iqx} \langle p_p, s_p | [J^\mu(x), J^\nu(x)] | p_p, s_p \rangle. \quad (1.23)$$

The non-perturbative hadronic tensor contains the quark-quark correlation function [68, 69]. The most general form of the two-quark correlation function is

$$\Phi_{ij}(k, p_p, s_p) = \frac{1}{(2\pi)^4} \int d^4\xi e^{ik\xi} \langle p_p, s_p | \bar{\psi}_j(0) \psi_i(\xi) | p_p, s_p \rangle. \quad (1.24)$$

Here p_p and s_p denote the momentum and the spin of the proton and k the momentum of the quark inside the nucleon. This quark-quark correlation function is a Dirac matrix and can therefore be decomposed in the basis of Dirac structures ($\mathbf{1}$, γ_5 , γ^μ , $\gamma^\mu \gamma_5$, $i\sigma^{\mu\nu} \gamma_5$) and a combination of the Lorentz vectors k , p_p and Lorentz pseudovector s_p .

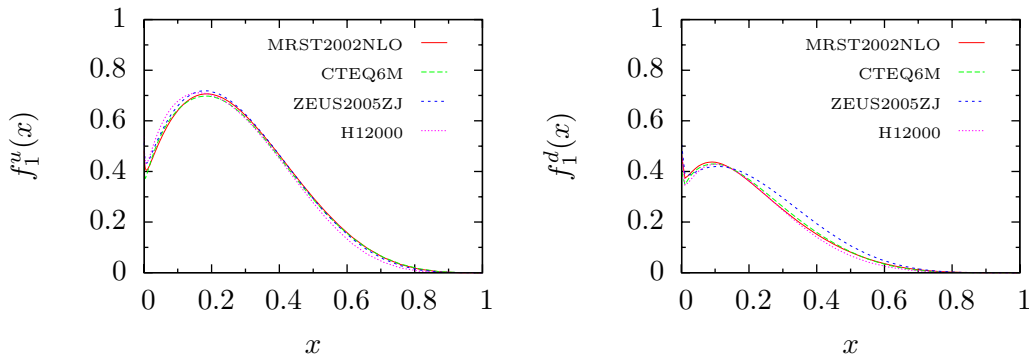


Figure 1.4: Quark distribution functions for different parametrizations for a) u quarks and b) d quarks in the proton at an input scale of $Q^2 = 4 \text{ GeV}^2$, taken from the Durham HEP Databases. Q^2 of 4 GeV^2 is chosen since this belongs to a reasonable value which enters our cross section calculations in Chapter three and four.

The above definition holds in the light-cone gauge $A^+ = 0$ for the gluon field. In other gauges, in order to have colour gauge invariance of the correlator in Eq. 1.24, a gauge link \mathcal{U} has to be inserted between the two quark fields

$$\mathcal{U}(0, \xi) = \mathcal{P} \exp \left(-ig \int_0^\xi dz^\mu A_\mu(z) \right). \quad (1.25)$$

P denotes ordering along a path from 0 to ξ . It is not possible to calculate this correlation function by means of perturbative QCD. In order to calculate the correlation one has either to resort to models or lattice QCD.

The quark-quark correlation function can be parametrized in terms of parton distribution functions $q(x)$, $\Delta q(x)$ and $\delta q(x)$,

$$\begin{aligned} \Phi(x) &= \int d^2 \vec{k}_T dk^- \Phi(k, p_p, s_p) \Big|_{k^+ = xp_p^+} \\ &= \frac{1}{2} \left(q(x) \not{p}_+ + \lambda \Delta q(x) \gamma_5 \not{p}_+ + \delta q(x) \frac{\gamma_5 [\not{p}_{p,T}, \not{p}_+]}{2} \right). \end{aligned} \quad (1.26)$$

In inclusive lepton-hadron scattering the unpolarized distribution function $q(x)$ and the helicity function $\Delta q(x)$ can be obtained¹. These are twist-two functions. The twist of an operator is defined in the operator product expansion as the difference between the mass dimension of the operator and its spin. However it is common to use it in the sense that higher twist terms are suppressed by a factor $(M_N/Q^2)^{t-2}$ in comparison to the lowest twist $t = 2$. The only other twist two distribution function is the transversity function $\delta q(x)$. In a non-relativistic limit one has $\Delta q = \delta q$, which does not hold for the relativistic case, where only an upper limit can be given. The most important parton distribution for this thesis is $q(x)$. Therefore we show in Fig. 1.4 the u and d quark distributions of the proton for different parametrizations. Many different models exist in the literature, but as can be seen in the figure they have only minor deviation.

¹Other common notations for the functions $q(x)$, $\Delta q(x)$ and $\delta q(x)$ are $f_1(x)$, $g_1(x)$ and $h_1(x)$, respectively.

It is not possible to measure h_1 in inclusive deep inelastic lepton-hadron scattering. Measurements have to be made either in Drell-Yan (in the collision of two hadrons) or in semi-inclusive DIS. In order to obtain δq , which is a chiral-odd function it has to be combined with another chiral-odd function to achieve experimental access. Going to next order, twist-three level, more distribution functions, chiral-even as well as chiral-odd, appear [70, 71].

The individual distribution functions can be projected out. We define

$$\Phi^{[\Gamma]} \equiv \frac{1}{2} \text{Tr}(\Phi \Gamma), \quad (1.27)$$

where Γ represents a specific Dirac structure. With this definition the three leading twist distributions are given by

$$q(x) = \Phi^{[\gamma^+]}, \quad (1.28)$$

$$\Delta q(x) = \Phi^{[\gamma^+ \gamma^5]}, \quad (1.29)$$

$$\delta q(x) = \Phi^{[i\sigma^{i+} \gamma^5]}(x). \quad (1.30)$$

1.1.2.1 Factorization in inclusive processes

The electron-nucleon cross section can be factorized into a cross section that describes the scattering off a point-like parton, convoluted with a parton distribution function. Here we show how a cross section can be factorized in the case of deep inelastic scattering

$$\frac{d^2 \sigma_{eN \rightarrow e'X}}{dQ^2 dx_B} = \sum_a \int_x^1 d\xi f_{a/N}(\xi, \mu_F) \frac{d^2 \sigma_{ea \rightarrow e'a'}}{dQ^2 dx_B}(q^\mu, \xi P^\mu, \mu_F, \alpha_s(\mu_R)), \quad (1.31)$$

where power suppressed terms are neglected. The index a in the distribution function $f_{a/N}(\xi, \mu)$ labels the parton which can either be a quark of specific flavor or a gluon, while N classifies the hadron that takes part in the reaction. The partonic subprocess that depends on the hard scale can be calculated perturbatively in a series of the strong and the electromagnetic coupling constants, α_s and α_{em} . Two different divergencies appear in this calculation. Due to integrals over loop momenta the partonic subprocess is UV-divergent. These UV-divergencies are removed by renormalizing the strong coupling constant at a scale μ_R . Apart from that IR-divergences appear which correspond to the emission of soft or collinear partons. At a factorization scale μ_F these divergent parts can be absorbed into the redefinition of the bare distribution function. The possibility of factorizing a process has to be proven for each process [72, 73].

1.1.2.2 Evolution in inclusive processes

Parton functions are nonperturbative objects but their dependence on the factorization scale μ_F can be calculated in perturbative QCD. This is due to the fact that the electron-parton subprocess exhibits the μ_R -dependence which can be computed to a given order in perturbation theory. The cross section, which is an observable, has still to be independent of μ_R . If the PDF is known at an initial scale μ_0 it can be computed at any scale μ by means of evolution equations.

The virtual photon in deep inelastic scattering experiments acts as a local probe that resolves local distances being inversely proportional to its virtuality. Depending on Q^2 one

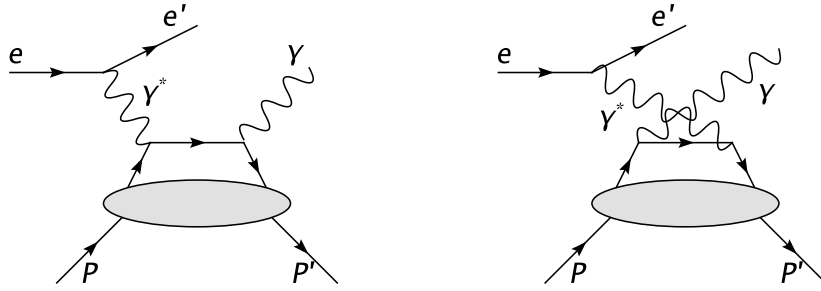


Figure 1.5: The two possible graphs for deeply virtual Compton scattering.

resolves different parton densities. Identifying Q^2 with the initial scale μ the quark densities in DIS are governed by the DGLAP equation [34, 35, 36, 37, 38]

$$\mu_F^2 \frac{d}{d\mu_F^2} q(x, \mu_F^2) = \int_x^1 \frac{dy}{y} P\left(\frac{x}{y}, \alpha_s(\mu_F^2)\right) q(y, \mu_F, \mu_R^2), \quad (1.32)$$

where $P\left(\frac{x}{y}, \alpha_s(\mu_F^2)\right)$ is the evolution kernel and $q(y, \mu_F, \mu_R^2)$ the parton distribution depending on the factorization and renormalization scales. This equation says that a quark of momentum fraction x , which is given on the left side of the equation, could have originated from a quark with a larger momentum fraction y , given on the right side of the equation, that has radiated a gluon and therefore lost some momentum. The probability of this gluon radiation is proportional to the evolution kernel. For gluons there is a strong rise of the PDF at small x for large μ_F , which is weaker for quarks.

The short and long distance parts are connected by the factorization scale μ_F . The kernel and the PDFs depend on the choice of the factorization scheme, which determines how the divergences are absorbed in the parton distributions. Physical observables are independent of the choice of the factorization scheme.

1.1.3 Hard exclusive scattering processes

A special class of reactions are hard exclusive processes. In this case all final-state particles have to be determined in coincidence. Much effort is invested to study this exclusive reactions intensively (see for an overview [74]).

One prominent example of exclusive scattering is deeply virtual Compton scattering depicted in Fig. 1.5 [32, 42]. In this reaction an electron emits a virtual photon which scatters off one quark of the proton. The final state consists of the scattered electron and proton and in addition of a real photon. This process is only scratched here, but will be considered in more detail in Sec. 2.5.1

$$e(p_e) + N(p_p) \rightarrow e'(p_{e'}) + \gamma(p_{q'}) + N'(p_{p'}). \quad (1.33)$$

The virtuality of the exchanged photon Q^2 is large $Q^2 \gg p_p^2$ while the momentum transfer between p_p and $p_{p'}$ is small. First experimental results can be found in [75, 76, 77, 78].

We present now kinematical variables that are commonly used,

$$t = \Delta^2 = (p_{p'} - p_p)^2, \quad (1.34)$$

$$P = \frac{p_p + p_{p'}}{2}. \quad (1.35)$$

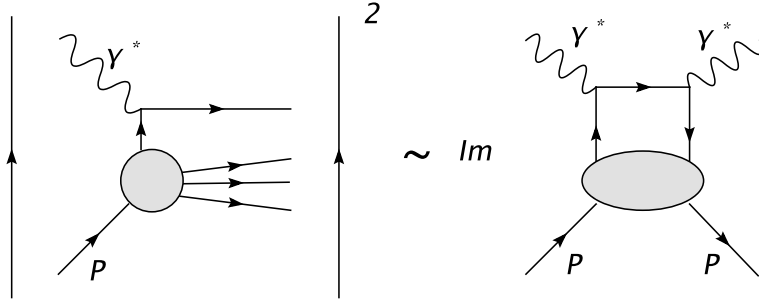


Figure 1.6: The optical theorem states that the cross section $ep \rightarrow e'X$ can be related to the imaginary part of the amplitude of the deeply virtual Compton forward scattering.

The plus-momentum transfer between the nucleons is defined as

$$\begin{aligned}\xi &= -\frac{\Delta \cdot n_-}{2P \cdot n_-} \\ &= \frac{p_p^+ - p_{p'}^+}{p_p^+ + p_{p'}^+},\end{aligned}\tag{1.36}$$

which is given in light-cone coordinates. These are defined in App. A. The kinematical variable ξ is commonly referred to as skewness and is defined in the interval $\xi \in [-1, 1]$. In the Bjorken limit it reduces to

$$\xi \approx \frac{x_B}{2 - x_B}.\tag{1.37}$$

The final-state proton has a different momentum than the initial state proton. This is in contrast to DIS experiments where the momenta are the same. In the case of DIS one can relate the forward scattering amplitude to the imaginary part of the cross section via the well-known optical theorem, which is shown in Fig. 1.6. The cross section can be parametrized in terms of PDFs. If we turn our attention to DVCS the situation changes. Due to the different proton momenta the scattering amplitude of DVCS looks more similar to the cross section of DIS and the amplitude is parametrized in terms of GPDs.

Apart from DVCS the final state can consist of a virtual photon, instead of the real one, called double deeply virtual Compton scattering. It can also consist of a meson, in this case the process is called hard exclusive meson production which is shown in Fig. 1.7. In that case a meson distribution amplitude is needed to describe the meson production.

1.1.3.1 A few words on factorization and evolution in exclusive processes

A problem is that QCD cannot be solved exactly. In high energy processes where large scales are present factorization theorems allow to write observables in terms of hard scattering and universal nonperturbative functions, that can be measured.

It was shown by Collins and Freund [29, 30], that factorization holds for the DVCS amplitude to all orders in perturbation theory up to power suppressed terms,

$$\mathcal{A}(\gamma^* p \rightarrow \gamma^* p) = \sum_i \int_{-1}^1 dx T^i(x, \xi, \rho, Q^2 - Q'^2) F^i(x, \xi, t),\tag{1.38}$$

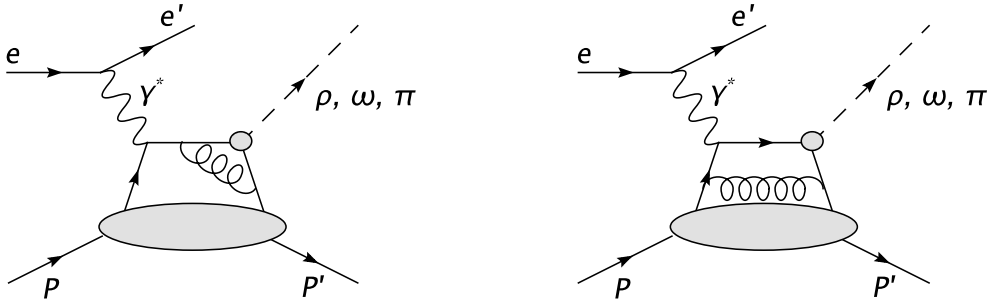


Figure 1.7: Hard exclusive meson production

where F contains the GPDs and T is the hard scattering kernel, see [29, 31, 30], hence the amplitude consists of a perturbative and a nonperturbative part. This factorization theorem also holds for the production of virtual photons. The measurement of GPDs rests on the factorization theorem.

For light meson electroproduction factorization is analogous. Collins provides a factorization theorem for hard exclusive meson production [31, 30]. The scattering amplitude can be written as

$$\mathcal{A}(\gamma^* p \rightarrow Mp) = \frac{1}{Q} \sum_{ij} \int_{-1}^1 dx \int_0^1 dz T^{ij}(x, \xi, z, Q^2) F^i(x, \xi, t) \phi^j(z), \quad (1.39)$$

including the meson distribution amplitude $\phi^j(z)$. The amplitude for meson production requires the photon and meson to be longitudinally polarized. All other contributions are suppressed by further powers of $1/Q$ at least.

As the PDFs also the GPDs depend on a factorization scale and can be evolved, but the situation is more complicated than in the DIS case. Evolution has to be considered independently in different regions. In Fig. 2.1 we have displayed the different support regions of GPDs. In the regions where either $x \in [\xi, 1]$ or $x \in [-\xi, -1]$ the evolution equations are similar to the DGLAP equations [34, 35, 36, 37, 38]. In the region $x \in [-\xi, \xi]$ the evolution is related to a meson distribution amplitude, which obeys the ERBL evolution equation [39, 40, 41] because the GPDs can be interpreted as the probability to find a quark-antiquark pair, which corresponds to a meson.

Chapter 2

Generalized parton distribution functions

In this chapter we take into account exclusive processes only. In the theoretical description of these processes we encounter matrix elements of quark and gluon operators, which cannot be computed perturbatively. They are parametrized in terms of generalized parton distribution functions which we define in this chapter.

We start with the nucleon GPDs and continue with a GPD for the pion. Moreover, we will discuss some basic properties of generalized parton distribution functions, while a more detailed description can be found in [79]. In the last section we will focus on deeply virtual Compton scattering as well as similar processes involving weak currents. These processes give access to GPDs.

2.1 Definition of GPDs

2.1.1 Nucleon GPDs

Exclusive processes like DVCS and the formalism of generalized parton distribution functions provide a broad range of information about the internal structure of hadrons. These functions are a generalization of parton distribution functions appearing in inclusive processes to functions describing exclusive reactions. GPDs depend on three kinematical variables rather than only on one, as parton distributions, and can therefore give access to a more than one dimensional picture of the hadron.

Besides virtual Compton scattering also hard exclusive meson production and the production of a virtual photon instead of a real one can be parametrized in terms of GPDs. Furthermore the virtual photon emitted from the electron in DVCS can be replaced by a boson of the weak interaction, namely a W^\pm or a Z^0 . These processes can also be described in terms of GPDs.

The leading twist decomposition in terms of GPDs of the bilocal light-cone matrix elements

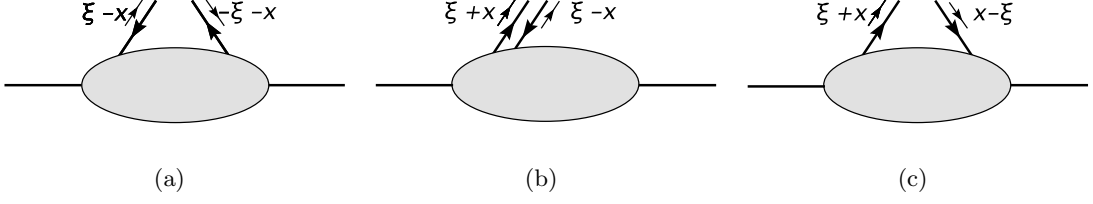


Figure 2.1: Parton interpretation of GPDs in three kinematical regions: a) $x \in [-1, -\xi]$, b) $x \in [-\xi, \xi]$ and c) $x \in [\xi, 1]$

of two quark operators for the vector and axial vector case are

$$\begin{aligned}
 F^q &= \frac{1}{2} \int \frac{dz^-}{2\pi} e^{ixP^+z^-} \langle p_{N'} | \bar{q}(-\frac{z}{2}) \gamma^+ q(\frac{z}{2}) | p_N \rangle \Big|_{z_\perp=z^+=0} \\
 &= \frac{1}{2P^+} \left[H^q(x, \xi, t) \bar{u}(p_{N'}) \gamma^+ u(p_N) + E^q(x, \xi, t) \bar{u}(p_{N'}) \frac{i\sigma^{+\nu} \Delta_\nu}{2m_N} u(p_N) \right], \quad (2.1)
 \end{aligned}$$

$$\begin{aligned}
 \tilde{F}^q &= \frac{1}{2} \int \frac{dz^-}{2\pi} e^{ixP^+z^-} \langle p_{N'} | \bar{q}(-\frac{z}{2}) \gamma^+ \gamma_5 q(\frac{z}{2}) | p_N \rangle \Big|_{z_\perp=z^+=0} \\
 &= \frac{1}{2P^+} \left[\tilde{H}^q(x, \xi, t) \bar{u}(p_{N'}) \gamma^+ \gamma_5 u(p_N) + \tilde{E}^q(x, \xi, t) \bar{u}(p_{N'}) \frac{i\gamma_5 \Delta^+}{2m_N} u(p_N) \right], \quad (2.2)
 \end{aligned}$$

where we omitted the polarization dependence of the hadrons for legibility [79]. The relativistic state $|p_N\rangle$ denotes the nucleon of four-momentum p_N , where the index N represents either a proton or a neutron. As in the definition of PDFs this definition is valid for the light-cone gauge where the gluon field fulfills the condition $A^+(x) = 0$. Otherwise a Wilson line along the light-like path has to be inserted between the quark fields. For further details see [80, 79]. Here $u(p_N)$ and $\bar{u}(p_{N'})$ are the Dirac spinors of the nucleon and m_N the nucleon mass. From Lorentz-invariance it follows that the GPDs H , \tilde{H} , E and \tilde{E} depend on t , x and ξ . By applying time reversal invariance one obtains $H(x, \xi, t) = H(x, -\xi, t)$. From the definition of the GPDs it can be seen that $(H(x, \xi, t))^* = H(x, -\xi, t)$, hence H must be real. The same applies to \tilde{H} , E and \tilde{E} .

For the functions defined in Eqs. 2.1 and 2.2 three different support regions are shown in Fig. 2.1. The variable x can be element of the interval $[\xi, 1]$. In this case a quark is emitted from the proton and reabsorbed after the scattering process where both momentum fractions $\xi + x$ and $x - \xi$ are positive. In addition x can be element of $[-1, -\xi]$. Here an antiquark is emitted and reabsorbed by the nucleon and both momenta are negative. These two regions are referred to as DGLAP regions [34, 35, 37]. Finally, for $x \in [-\xi, \xi]$, this can be interpreted as the emission of a quark-antiquark pair with $x + \xi > 0$ and $x - \xi < 0$ and is referred to as ERBL region, [39, 40, 41]. Altogether there is no net spin transfer on the parton side because in the DGLAP region the emitted and the absorbed parton has the same helicity and in the ERBL region the helicity of the emitted partons couples to zero.

Furthermore there are GPDs for the gluon. For sake of completeness we give their defini-

tion

$$\begin{aligned}
F^g &= \frac{i}{P^+} \int \frac{dz^-}{2\pi} e^{ixP^+z^-} \left\langle p_{N'} \left| G^{+\mu} \left(-\frac{z}{2} \right) \gamma^+ G_\mu^+ \left(\frac{z}{2} \right) \right| p_N \right\rangle \Big|_{z_\perp=z^+=0} \\
&= \frac{1}{2P^+} \left[H^g(x, \xi, t) \bar{u}(p_{N'}) \gamma^+ u(p_N) + E^g(x, \xi, t) \bar{u}(p_{N'}) \frac{i\sigma^{+\nu} \Delta_\nu}{2m_N} u(p_N) \right], \quad (2.3)
\end{aligned}$$

$$\begin{aligned}
\tilde{F}^g &= -\frac{i}{P^+} \int \frac{dz^-}{2\pi} e^{ixP^+z^-} \left\langle p_N \left| G^{+\mu} \left(-\frac{z}{2} \right) \gamma^+ \gamma_5 \tilde{G}_\mu^+ \left(\frac{z}{2} \right) \right| p_{N'} \right\rangle \Big|_{z_\perp=z^+=0} \\
&= \frac{1}{2P^+} \left[\tilde{H}^g(x, \xi, t) \bar{u}(p_{N'}) \gamma^+ \gamma_5 u(p_N) + \tilde{E}^g(x, \xi, t) \bar{u}(p_{N'}) \frac{\gamma_5 \Delta^+}{2m_N} u(p_N) \right], \quad (2.4)
\end{aligned}$$

where the gluon field strength is denoted by $G^{\mu\nu}(x)$.

When dealing with parton distribution functions of light quarks it is sometimes useful to use isoscalar and isovector combinations of the quark flavor GPDs

$$H^{I=0} = H^u + H^d, \quad (2.5)$$

$$H^{I=1} = H^u - H^d. \quad (2.6)$$

2.1.2 Pion GPD

After defining the nucleon GPDs we will now add the pion GPD parametrizing the blob in Fig. 2.2. We define

$$2P^+ H_\pi^q(x, \xi, t) = \int \frac{dz^-}{2\pi} e^{ixP^+z^-} \left\langle p_{\pi'} \left| \bar{\psi}^q \left(-\frac{z^-}{2} \right) \gamma^+ \psi^q \left(\frac{z^-}{2} \right) \right| p_\pi \right\rangle \Big|_{z_\perp=z^+=0}. \quad (2.7)$$

Again only in the light-cone gauge we can omit the gauge link as presented here. Because of parity invariance the functions corresponding to \tilde{H}^q and \tilde{H}^g are zero. For pions isospin invariance relates the π^+ , π^- and π^0 GPDs to the isosinglet combinations

$$H_{\pi^+}^{u+d} = H_{\pi^-}^{u+d} = H_{\pi^0}^{u+d} \quad (2.8)$$

and isotriplet combinations

$$H_{\pi^+}^{u-d} = -H_{\pi^-}^{u-d}, \quad (2.9)$$

$$H_{\pi^0}^{u+d} = 0, \quad (2.10)$$

where we used $H^{u\pm d} = H^u \pm H^d$. Aside from isospin invariance we can infer from charge conjugation

$$H_\pi^{u+d}(x, \xi, t) = -H_\pi^{u+d}(-x, \xi, t), \quad H_\pi^{u-d}(x, \xi, t) = H_\pi^{u-d}(-x, \xi, t) \quad (2.11)$$

that the isosinglet sector corresponds to $C = 1$ and the isotriplet one to $C = -1$.

2.2 Limits

To get a better physical access to GPDs we consider the forward limit $t \rightarrow 0$ where the initial and final state nucleon have the same momenta. By inserting Eq. 1.24 into Eqs. 1.28 and 1.29

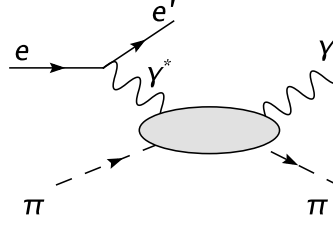


Figure 2.2: Deeply virtual scattering off a pion. The blob is parametrized by GPDs.

with the definition of the GPDs in Eq. 2.1 one can easily see that

$$H^q(x, 0, 0) = q(x), \quad \tilde{H}^q(x, 0, 0) = \Delta q(x) \quad x > 0, \quad (2.12)$$

$$H^q(-x, 0, 0) = -\bar{q}(-x), \quad \tilde{H}^q(-x, 0, 0) = -\Delta q(x) \quad x < 0. \quad (2.13)$$

The generalized parton distribution functions reduce to the ordinary helicity independent parton distribution $q(x)$ and the helicity dependent parton distribution $\Delta q(x)$. Since the GPDs E and \tilde{E} are multiplied by Δ in their definition there is no corresponding forward limit. The information of the GPDs in the forward limit can thus not be accessed in inclusive processes. Nevertheless it is common to indicate

$$E^q(x, 0, 0) = e^q(x), \quad (2.14)$$

which is connected to the angular momentum structure of the nucleon. For sake of completeness we give the forward limit of the gluons

$$H^g(x, 0, 0) = xg(x), \quad (2.15)$$

$$\tilde{H}^g(x, 0, 0) = x\Delta g(x). \quad (2.16)$$

2.3 Form factors and polynomiality

Another possibility to get access to observables connected to GPDs is given in this section. We show how to derive form factors and structure functions from GPDs and start from a decomposition of the nucleon current in terms of the form factors $F_1^q(t)$ and $F_2^q(t)$. For the structure functions the starting point is the energy-momentum tensor. The Noether theorem states that each symmetry of a system is connected to a conserved current. In the case of translation it is the energy momentum tensor which is decomposed in terms of the structure functions $A^{q,g}(t)$, $B^{q,g}(t)$, $C^{q,g}(t)$ and $\tilde{C}^{q,g}(t)$,

$$\langle P' | \bar{q}(0) \gamma^\mu q(0) | P \rangle = F_1^q(t) \bar{u}(p_{N'}) \gamma^\mu u(p_N) + F_2^q(t) \bar{u}(p_{N'}) \frac{i\sigma^{\mu\nu} \Delta_\nu}{2m_N} u(p_N), \quad (2.17)$$

$$\begin{aligned} \langle P' | T_{q,g}^{\mu\nu}(0) | P \rangle &= A_{q,g}(t) \bar{u}(p_{N'}) P^{\{\mu} \gamma^{\nu\}} u(p_N) + B_{q,g}(t) \bar{u}(p_{N'}) \frac{P^{\{\mu} i\sigma^{\nu\}} \Delta_\nu}{2m_N} u(p_N) \\ &+ C_{q,g}(t) \frac{\Delta^\mu \Delta^\nu - g_{\mu\nu} \Delta^2}{m_N} \bar{u}(p_{N'}) u(p_N) \\ &+ \tilde{C}_{q,g}(t) g^{\mu\nu} m_N \bar{u}(p_{N'}) u(p_N), \end{aligned} \quad (2.18)$$

see also [32, 79, 81]. If we recall the definition of the GPDs in Eq. 2.1 and set $z = 0$ the matrix element reduces to that of Eq. 2.17. When we then integrate over x one can read off the Pauli and Dirac form factors

$$\int_{-1}^1 dx H^q(x, \xi, t) = F_1^q(t), \quad (2.19)$$

$$\int_{-1}^1 dx E^q(x, \xi, t) = F_2^q(t), \quad (2.20)$$

for the flavor q . They can be related to the nucleon form factor via isospin symmetry

$$F_1^{u/p} = 2F_1^p + F_1^n, \quad (2.21)$$

$$F_1^{d/p} = 2F_1^n + F_1^p. \quad (2.22)$$

Similarly we find in the axial vector case

$$\int_{-1}^1 dx \tilde{H}^q(x, \xi, t) = g_A^q(t), \quad (2.23)$$

$$\int_{-1}^1 dx \tilde{E}^q(x, \xi, t) = g_P^q(t), \quad (2.24)$$

which are the pseudoscalar and axial nucleon form factors.

Lorentz and time-reversal invariance impose another constraint on GPDs. Therefore we introduce the Mellin moments which are x -integrals over the GPDs weighted with x ,

$$H_{n+1}^q(\xi, t) = \int_{-1}^1 dx x^n H^q(x, \xi, t), \quad (2.25)$$

$$E_{n+1}^q(\xi, t) = \int_{-1}^1 dx x^n E^q(x, \xi, t). \quad (2.26)$$

We have already seen the first Mellin moments for $n = 0$ in Eqs. 2.19 and 2.20, the form factors. One can show that the Mellin moments can be written as

$$H_{n+1}^q(\xi, t) = \sum_{\substack{i=0 \\ i \text{ even}}}^n A_{n+1,i}^q(t) (2\xi)^i + \text{mod}(n+1, 2) (2\xi)^{n+1} C_{n+1}^q(t), \quad (2.27)$$

$$E_{n+1}^q(\xi, t) = \sum_{\substack{i=0 \\ i \text{ even}}}^n B_{n+1,i}^q(t) (2\xi)^i - \text{mod}(n+1, 2) (2\xi)^{n+1} C_{n+1}^q(t), \quad (2.28)$$

where $\text{mod}(n+1, 2)$ is 1 for even n and 0 for odd n . Due to Lorentz-invariance the ξ -dependence on the right-hand side can only originate from factors of Δ^μ in the form factor decomposition. The x^n moments are polynomials in ξ of order $n+1$ and must be even due to time-reversal invariance. Thus there are important constraints from polynomiality. As can be seen very well from Eq. 2.28 the highest power of ξ in $H + E$ cancels.

A special role is played by the second Mellin moments

$$\int_{-1}^1 dx x H^q(x, \xi, t) = A^q(t) + 4\xi^2 C^q(t), \quad (2.29)$$

$$\int_{-1}^1 dx x E^q(x, \xi, t) = A^q(t) - 4\xi^2 C^q(t). \quad (2.30)$$

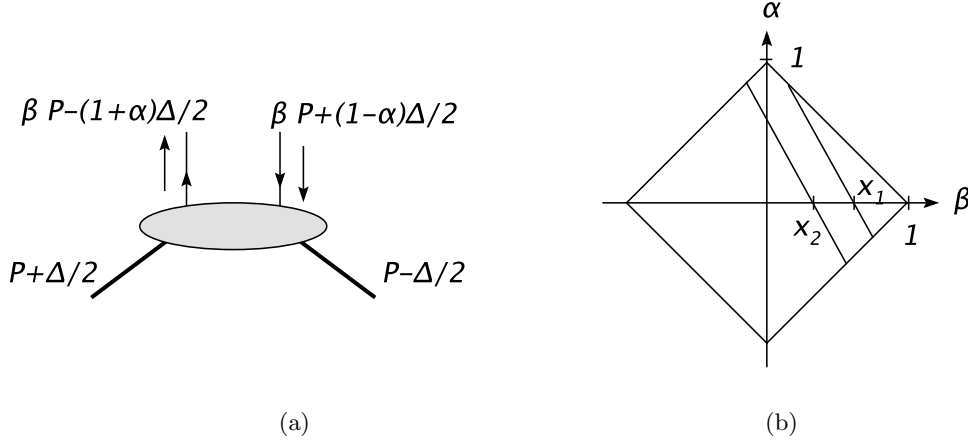


Figure 2.3: a) Shows the momenta associated with the partons and hadrons appearing in the double distribution and b) shows the corresponding support region of the double distribution

They enter the sum rule found by Ji [42]

$$2 \langle J_3^q \rangle = A^q(0) + B^q(0) = \lim_{t \rightarrow 0} \int_{-1}^1 dx x \left(H^q(x, \xi, t) + E^q(x, \xi, t) \right), \quad (2.31)$$

where $\langle J_3^q \rangle$ is the total angular momentum along z carried by quarks and antiquarks of flavor q of a proton polarized in the $+z$ direction. It connects the GPDs in their forward limit to the structure functions of the energy-momentum tensor of Eq. 2.18. This sum rule is a special case of the polynomiality relation from Eqs. 2.27 and 2.28. The same relation is given for the gluons

$$2 \langle J_3^g \rangle = A^g(0) + B^g(0). \quad (2.32)$$

Moreover,

$$J^q(0) + J^g(0) = \frac{1}{2} \quad (2.33)$$

shows that the angular momentum of the quarks and gluons adds up to one half. This is the only known nucleon spin decomposition on quark-gluon level. It is in agreement with the measurement of the value $1/2$ of the nucleon spin. But it is not possible to decompose these angular momenta further into a spin and orbital angular momentum part.

2.4 Double distributions

Double distributions are a parametrization of the non-diagonal matrix element of Eq. 2.1 defining the GPDs. According to [33] they are defined as

$$\begin{aligned}
& \left\langle p_{N'} \left| \bar{q} \left(-\frac{z}{2} \right) (z\gamma) q \left(\frac{z}{2} \right) \right| p_N \right\rangle \Big|_{z^2=0} \\
&= \bar{u}(p_{N'}) (z\gamma) u(p_N) \int d\beta d\alpha e^{-\beta(Pz)+i\alpha(\Delta z)/2} f^q(\beta, \alpha, t) \\
&+ \bar{u}(p_{N'}) \frac{i\sigma^{\mu\alpha} z_\mu \Delta_\alpha}{2m} u(p_N) \int d\beta d\alpha e^{-\beta(Pz)+i\alpha(\Delta z)/2} k^q(\beta, \alpha, t) \\
&+ \bar{u}(p_{N'}) \frac{\Delta z}{2m} u(p_N) \int d\beta d\alpha e^{i\alpha(\Delta z)/2} D^q(\beta, \alpha, t). \tag{2.34}
\end{aligned}$$

and are discussed in a detailed review in [82]. The last term, the so-called D -term was introduced by Polyakov and Weiss [83]. The support region for the two double distribution functions f^q and k^q is given by the rhombus $|\alpha| + |\beta| \leq 1$, which is shown in Fig. 2.3 b) and the one for the D -term by $|\alpha| \leq 1$. One can associate β with the momentum fraction x in a forward parton density and $(1 + \alpha)/2$ with the momentum fraction z in a meson distribution amplitude as shown in Fig. 2.3 a). A consequence of time-reversal invariance is that f^q and k^q have to be even in α and D^q has to be odd in α . A relation between the GPDs and the double distributions is given by

$$H^q(x, 0, 0) = \int d\beta d\alpha \delta(x - \beta - \xi\alpha) f^q(\beta, \alpha, t) + \text{sgn}(\xi) D^q\left(\frac{\xi}{x}, t\right), \tag{2.35}$$

$$E^q(x, 0, 0) = \int d\beta d\alpha \delta(x - \beta - \xi\alpha) k^q(\beta, \alpha, t) - \text{sgn}(\xi) D^q\left(\frac{\xi}{x}, t\right), \tag{2.36}$$

where the lines of integration are shown in 2.3 b). The D -term only contributes to the ERBL region. The double distributions play a prominent role in modeling GPDs, since Eqs. 2.35 and 2.36 satisfy polynomial constraints.

By integrating over the line $x = \beta$ one obtains the forward quark distribution

$$q(x) = \int_{x-1}^{1-x} d\alpha f^q(x, \alpha, 0). \tag{2.37}$$

Since we now have a simple connection to the known forward distribution function $q(x)$ it is obvious to use them in an ansatz as it was used in [74, 84]

$$f^q(\beta, \alpha) = q(\beta) h^q(\beta, \alpha), \tag{2.38}$$

with the profile function $h^q(\beta, \alpha)$ normalized to one

$$\int_{-1+|\beta|}^{1-|\beta|} d\alpha h^q(\beta, \alpha) = 1. \tag{2.39}$$

Note that this ansatz is very simple and does not include a t -dependence. The easiest way to include a t -dependence is to multiply by the form factor which depends on t only and gives automatically the right behavior for the forward limit. Two approaches will be shown in more detail in Sec. 3.6.

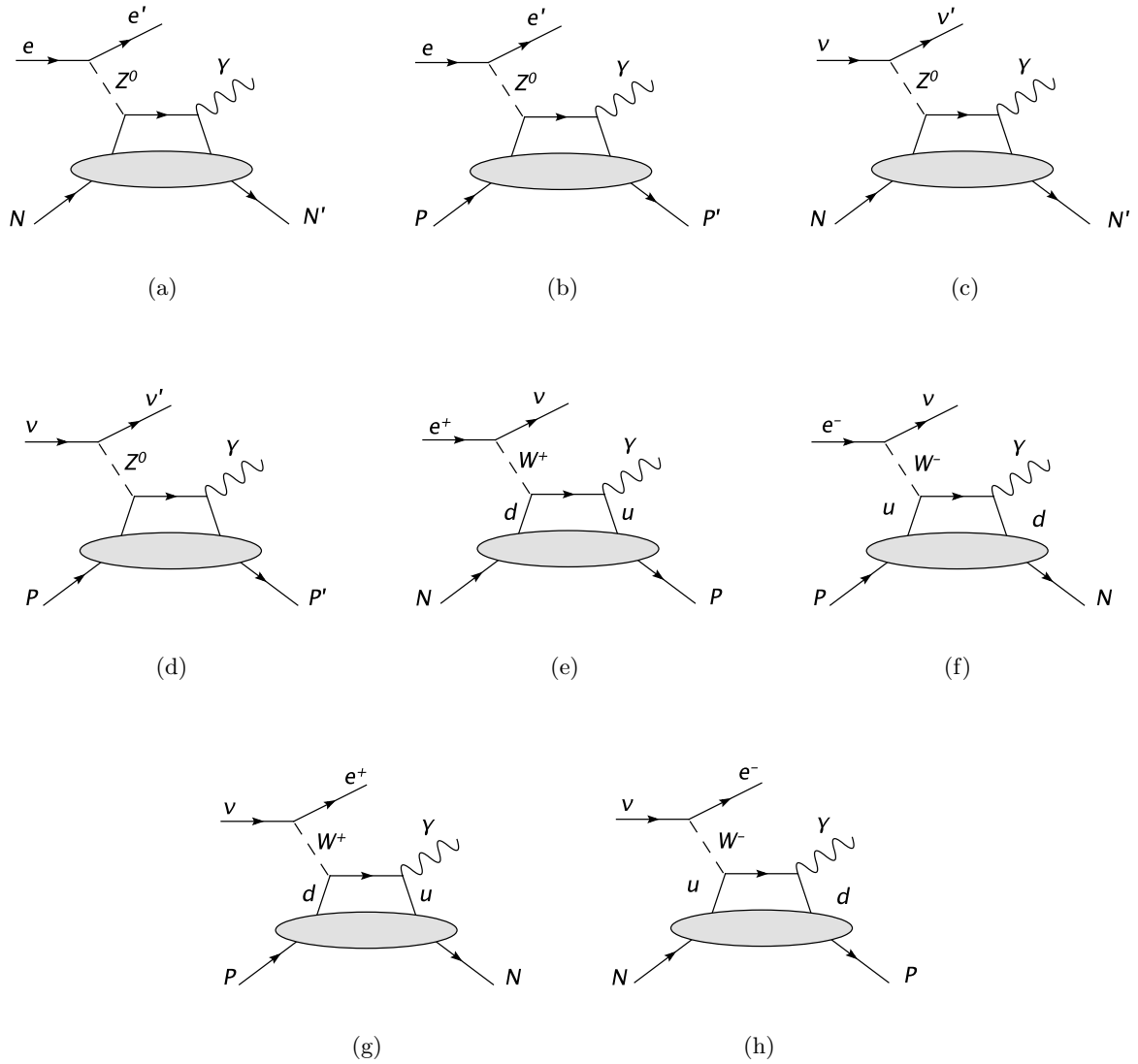


Figure 2.4: In this picture we show the different possible weak scattering processes for DVCS for different lepton beams. Depending on the beam and the charge of the nucleon target a W^\pm or the neutral Z^0 boson can be exchanged.

2.5 Access to GPDs via DVCS and weak currents

In the last chapter we have introduced GPDs which can be studied in DVCS. This process is shown in Fig. 2.5. In DVCS the electron beam emits a virtual photon. But it is also possible that an electron beam emits a W^- or a Z^0 boson, which are gauge bosons of the weak interaction. In addition to that there is a possibility of having a positron beam, where a γ , a W^- or a Z^0 can be emitted. And furthermore by taking a neutrino or antineutrino beam all three weakly coupling bosons can be emitted. Depending on the charge of the boson and the target (proton or neutron) the boson scatters off a certain quark inside the nucleon. Possible scattering processes are depicted in Fig. 2.4. We will consider only u and d quarks and antiquarks emitted and absorbed by the nucleon. All heavier quarks are neglected.

In this section we first derive the Compton amplitude for DVCS. This result can also be found in [32]. Hereafter, we repeat the calculation for those processes with W^+ , W^- or Z^0 as exchange particles instead of a photon, as for example a Z^0 scattering on a d quark inside the proton. In a next step we give the total scattering amplitude including the leptonic part and emphasize the polarization of the exchanged bosons. We will see that only certain combinations of initial- and final-state polarizations survive. Therefrom it follows that the amplitudes are proportional to different combinations of F^q and \tilde{F}^q from Eqs. 2.3 and 2.4 which contain the GPDs. To conclude we give two tables summarizing the different processes and their corresponding combinations of F^q and \tilde{F}^q including different pre-factors. These tables show the differences and how we can distinguish between the processes. They are given for positive (Tab. 2.1) and negative (Tab. 2.2) helicities of the boson. Finally we introduce isospin to show how the matrix elements of these processes can be related to each other. These relations depend on the isospin only.

2.5.1 Deeply virtual Compton scattering

Compton scattering played an important role in the history of physics. Scattering electrons off a charged object gave a first indication that the electromagnetic wave is quantized [85]. Exploring the structure of hadrons with Compton scattering shows that the spin-dependent part of the scattering amplitude at sufficiently low energy is ruled by the anomalous magnetic moment of the hadron. We consider here DVCS at tree level in QCD. The process is dominated by single-quark exchange and we will see that the amplitude can be expressed in terms of GPDs.

In DVCS the initial proton with momentum p_p absorbs a photon with momentum p_q producing a real final-state photon with momentum $p_{q'} = p_q - \Delta$ and a recoil proton with momentum $p_{p'} = p_p + \Delta$. In the Bjorken limit the photon is absorbed by a quark with momentum $k - \frac{\Delta}{2}$ which becomes highly virtual and propagates perturbatively. This photon is radiated by a quark. The process is shown in Fig. 2.5.

We use the Feynman rules to calculate the scattering amplitude. The only part where the processes involving a γ^* , W^\pm or Z^0 differs, is the vertex where these particles couple to the quark. Therefore we specify these vertices here, while we do not give any other Feynman rules explicitly. In the case of a virtual photon the vertex is given by

$$-iee_q\gamma^\mu, \quad (2.40)$$

where e_q is the charge of the particle coupling to the photon, $e_q = \frac{2}{3}(-\frac{1}{3})$ for the u (d) quark.

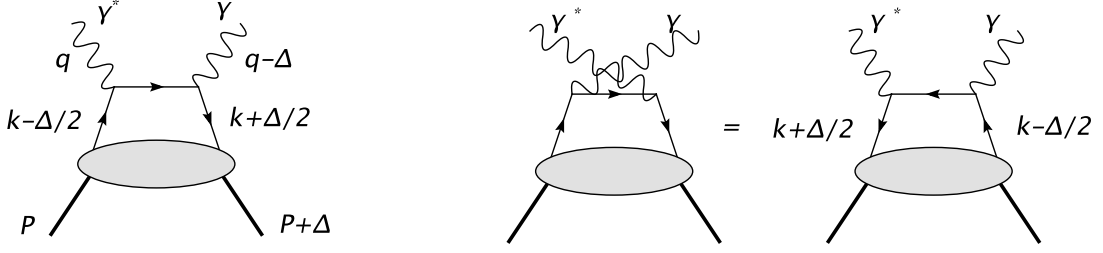


Figure 2.5: QCD graph and crossed graph for deeply virtual Compton scattering displaying the momenta of the active quark.

We can write down the Compton amplitude which has to be connected to the photon lines,

$$T_q^{ba} = -(ee_q)^2 \int \frac{d^4 k}{(2\pi)^4} d^4 z e^{ikz} \left(\gamma^b \frac{i}{\not{k} - \frac{\not{\Delta}}{2} + \not{q} + i\epsilon} \gamma^a + \gamma^b \frac{i}{\not{k} + \frac{\not{\Delta}}{2} - \not{q} + i\epsilon} \gamma^a \right)_{\beta\alpha} \left\langle p_{p'} \left| T \bar{q}_\beta \left(\frac{-z}{2} \right) q_\alpha \left(\frac{z}{2} \right) \right| p_p \right\rangle, \quad (2.41)$$

where T inside the matrix element is the time-ordering operator, which orders subsequent factors right to left consecutively in time. The first term in Eq. 2.41 describes a propagating quark and the second term a propagating antiquark as depicted in Fig. 2.5. The hard scale Q allows the separation of the perturbative part. A proof for the factorization is given in [86, 87, 29].

Let us consider the first term of the Compton amplitude in Eq. 2.41 in some more detail. To proceed further we choose a frame where the colliding proton and photon are collinear and consider a kinematic region where the scattered proton and photon are very close to being collinear. In that case all transverse momenta are of the order of Λ_{QCD} and will be neglected. From

$$Q^2 = -q^2 = -2q^+ q^- + q_T^2 \approx -2q^+ q^- \quad (2.42)$$

we then see that the plus and minus components q^\pm are proportional to Q . All components proportional to Q are considered to be big quantities. Moreover $p_{p'}^+$, $p_{q'}^-$ and k^+ are big, while p_p^- , $p_{p'}^+$, $p_{q'}^+$ and k^- are proportional to Λ_{QCD}^2/Q and will therefore be neglected. We use the Fierz transformation [17] to decompose the term $\bar{q}_\beta q_\alpha$ in the matrix element in Eq. 2.41. Neglecting components of four-vectors which do not produce big scalars in the Bjorken limit and inserting $\int dx \frac{d\lambda}{2\pi} e^{i\lambda(x-k \cdot n_-)} = 1$ gives

$$T_q^{ba} = -(ee_q)^2 \int \frac{d^4 k}{(2\pi)^4} \frac{d\lambda}{2\pi} d^4 z dx e^{ikz} e^{i\lambda(x-k \cdot n_-)} \frac{(n_+)_\mu (k \cdot n_- - \xi) + (n_-)_\mu \frac{Q^2}{4\xi}}{\frac{Q^2}{2\xi}(x-\xi) + i\epsilon} \times \frac{1}{4} \text{Tr}(\gamma^b \gamma^\mu \gamma^a (1 + \gamma_5) \gamma^\nu) \left\langle p_{p'} \left| T \bar{q} \left(\frac{-z}{2} \right) \gamma_\nu q \left(\frac{z}{2} \right) \right| p_p \right\rangle \Big|_{z_\perp = z^+ = 0} + \text{crossed term.} \quad (2.43)$$

Calculating the trace we find

$$\begin{aligned}
T_q^{ba} &= -(ee_q)^2 \int \frac{d^4 k}{(2\pi)^4} \frac{d\lambda}{2\pi} d^4 z dx e^{ikz} e^{i\lambda(x-k \cdot n_-)} \left\langle p_{p'} \left| T \bar{q} \left(\frac{-z}{2} \right) \gamma^+ q \left(\frac{z}{2} \right) \right| p_p \right\rangle \\
&\quad \times \left(2(n_+)_{\beta} (n_-)_{\alpha} \frac{k \cdot n_- - \xi}{\frac{Q^2}{2\xi}(x-\xi) + i\epsilon} - \frac{1}{2} \frac{g_{\perp}^{\mu\nu}}{x-\xi+i\epsilon} + \frac{1}{2} \frac{-i\epsilon_{\perp}^{\mu\nu}}{x-\xi+i\epsilon} \right) \Big|_{z_{\perp}=z^+=0} \\
&\quad + \text{crossed term}, \tag{2.44}
\end{aligned}$$

with

$$g_{\perp}^{ab} = g^{ab} - (n_+)^a (n_-)^b - (n_+)^b (n_-)^a \quad \text{and} \quad \epsilon_{\perp}^{ab} = \epsilon^{ab\mu\nu} - (n_+)^a (n_-)^b - (n_+)^b (n_-)^a. \tag{2.45}$$

The only large component that is left is the plus component in the perturbative part. From $\gamma^{\lambda} \bar{q} \gamma_{\lambda} q$ one gets $\gamma^- \bar{q} \gamma^+ q$, where $\gamma^- = p_{\lambda} \gamma^{\lambda}$, $\gamma^+ = n_{\lambda} \gamma^{\lambda}$. In the soft, non-perturbative part only γ^+ remains. Integrating over k and z leads to the final form

$$\begin{aligned}
T_q^{ba} &= -(ee_q)^2 \int dx \frac{d\lambda}{2\pi} e^{i\lambda x} \left\langle p_{p'} \left| T \bar{q} \left(\frac{-z}{2} \right) \gamma_{\nu} q \left(\frac{z}{2} \right) \right| p_p \right\rangle \\
&\quad \times \left(2(n_+)_{\beta} (n_-)_{\alpha} \frac{k \cdot n_- - \xi}{\frac{Q^2}{2\xi}(x-\xi) + i\epsilon} - \frac{1}{2} \frac{g_{\perp}^{ab}}{x-\xi+i\epsilon} + \frac{1}{2} \frac{-i\epsilon_{\perp}^{ab}}{x-\xi+i\epsilon} \right) \Big|_{z_{\perp}=z^+=0} \\
&\quad + \text{crossed term}. \tag{2.46}
\end{aligned}$$

The crossed term can be calculated in the same way. By adding both terms some contributions vanish and the result of the amplitude is

$$\begin{aligned}
T_q^{ba} &= -(e_q e)^2 \int \frac{d\lambda}{2\pi} dx e^{ix\lambda} \\
&\quad \left\{ \left\langle P \left| \bar{q} \left(\frac{-z}{2} \right) \gamma^+ q \left(\frac{z}{2} \right) \right| P \right\rangle \frac{1}{2} \left(\frac{g_{\perp}^{ba}}{x-\xi+i\epsilon} + \frac{g_{\perp}^{ba}}{x+\xi-i\epsilon} \right) + \right. \\
&\quad \left. \left\langle P \left| \bar{q} \left(\frac{-z}{2} \right) \gamma^+ \gamma_5 q \left(\frac{z}{2} \right) \right| P \right\rangle \frac{1}{2} \left(\frac{i\epsilon_{\perp}^{ba}}{x-\xi+i\epsilon} - \frac{i\epsilon_{\perp}^{ba}}{x+\xi-i\epsilon} \right) \right\}. \tag{2.47}
\end{aligned}$$

In this result for the Compton amplitude we find the four GPDs in

$$\begin{aligned}
\int \frac{d\lambda}{2\pi} \left\langle P \left| \bar{q} \left(\frac{-z}{2} \right) \gamma^+ q \left(\frac{z}{2} \right) \right| P \right\rangle &= H(x, \xi, t) \bar{u}(p_{p'}) \gamma^+ u(p) \\
&\quad + E(x, \xi, t) \bar{u}(p_{p'}) \frac{i\sigma^{+\nu} \Delta_{\nu}}{2m_p} u(p), \tag{2.48}
\end{aligned}$$

$$\begin{aligned}
\int \frac{d\lambda}{2\pi} \left\langle P \left| \bar{q} \left(\frac{-z}{2} \right) \gamma^+ \gamma_5 q \left(\frac{z}{2} \right) \right| P \right\rangle &= H(x, \xi, t) \bar{u}(p_{p'}) \gamma^+ \gamma_5 u(p) \\
&\quad + E(x, \xi, t) \bar{u}(p_{p'}) \frac{i\gamma_5 \Delta^+}{2m_p} u(p). \tag{2.49}
\end{aligned}$$

These results are also given in [32].

2.5.2 Weak current hadronic amplitude in deeply virtual scattering

In this section we derive the amplitude for the W^\pm and Z^0 exchange. These calculations are similar to the DVCS case, therefore we omit details. For the W^\pm we need in addition the vertex of the coupling to a fermion which is given by

$$\frac{-ie}{\sin\theta_w 2\sqrt{2}} \gamma^\alpha (1 - \gamma^5) \quad (2.50)$$

where $\sin\theta_w \approx 0.48$ is the weak mixing angle. We arrive at the Compton amplitude for a W^+ and W^- boson which is depicted in Fig. 2.4 e,f)

$$T_{W^+}^{\mu\nu} = \frac{-e^2 e_q}{\sin\theta_w 2\sqrt{2}} \int \frac{d\lambda}{2\pi} dx e^{ix\lambda} \frac{1}{2} \quad (2.51)$$

$$\left\{ M_{pn} \left(\frac{i\epsilon_\perp^{\mu\nu} - g_\perp^{\mu\nu}}{x - \xi + i\epsilon} - \frac{i\epsilon_\perp^{\mu\nu} + g_\perp^{\mu\nu}}{x + \xi - i\epsilon} \right) + M_{p\gamma^5 n} \left(-\frac{i\epsilon_\perp^{\mu\nu} - g_\perp^{\mu\nu}}{x - \xi + i\epsilon} + \frac{i\epsilon_\perp^{\mu\nu} + g_\perp^{\mu\nu}}{x + \xi - i\epsilon} \right) \right\},$$

$$T_{W^-}^{\mu\nu} = \frac{-e^2 e_q}{\sin\theta_w 2\sqrt{2}} \int \frac{d\lambda}{2\pi} dx e^{ix\lambda} \frac{1}{2} \quad (2.52)$$

$$\left\{ M_{np} \left(\frac{i\epsilon_\perp^{\mu\nu} - g_\perp^{\mu\nu}}{x - \xi + i\epsilon} - \frac{i\epsilon_\perp^{\mu\nu} + g_\perp^{\mu\nu}}{x + \xi - i\epsilon} \right) + M_{n\gamma^5 p} \left(-\frac{i\epsilon_\perp^{\mu\nu} - g_\perp^{\mu\nu}}{x - \xi + i\epsilon} + \frac{i\epsilon_\perp^{\mu\nu} + g_\perp^{\mu\nu}}{x + \xi - i\epsilon} \right) \right\}.$$

where we have introduced the abbreviations

$$M_{pn} = \left\langle p_p \left| \bar{u} \left(\frac{-z}{2} \right) \gamma^+ d \left(\frac{z}{2} \right) \right| p_n \right\rangle, \quad (2.53)$$

$$M_{np} = \left\langle p_n \left| \bar{d} \left(\frac{-z}{2} \right) \gamma^+ u \left(\frac{z}{2} \right) \right| p_p \right\rangle, \quad (2.54)$$

$$M_{p\gamma^5 n} = \left\langle p_p \left| \bar{u} \left(\frac{-z}{2} \right) \gamma^+ \gamma^5 d \left(\frac{z}{2} \right) \right| p_n \right\rangle, \quad (2.55)$$

$$M_{n\gamma^5 p} = \left\langle p_n \left| \bar{d} \left(\frac{-z}{2} \right) \gamma^+ \gamma^5 u \left(\frac{z}{2} \right) \right| p_p \right\rangle. \quad (2.56)$$

Furthermore it is possible to have Z^0 exchange, where we need the vertices for the Z^0 coupling to a quark of charge e_q and isospin I_3 . This is given by

$$\frac{-ie}{\sin\theta_w \cos\theta_w} \left(\frac{1}{2} I_3 \gamma_\mu (1 - \gamma_5) - \sin^2\theta_w e_q \gamma^\mu \right). \quad (2.57)$$

The coupling of the neutral boson to a u quark or to a d quark is different due to the charge and isospin of the quarks. We can thus distinguish the corresponding Compton amplitudes. Relevant graphs are shown in Fig. 2.4 a), b). As an example for Z^0 exchange we show here

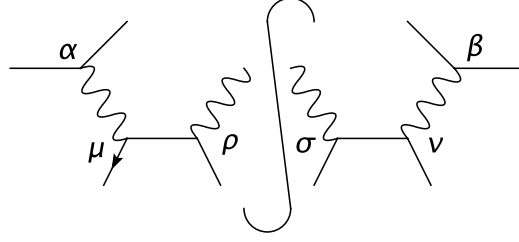


Figure 2.6: This plot shows the relevant indices for the calculation of the squared DVCS amplitude.

the result for scattering off a u quark inside a proton

$$\begin{aligned}
T_{z^0(p,u)}^{\mu\nu} &= \frac{-e^2 e_u}{\sin\theta_w \cos\theta_w} \int \frac{d\lambda}{2\pi} dx e^{ix\lambda} \frac{1}{2} \\
&\left\{ M_{p,u} \left(\frac{1}{4} - \frac{2}{3} \sin^2\theta_w \right) \left(\frac{-g_{\perp}^{\mu\nu}}{x - \xi + i\epsilon} + \frac{-g_{\perp}^{\mu\nu}}{x + \xi - i\epsilon} \right) \right. \\
&\quad \left. + \frac{1}{4} \left(\frac{i\epsilon_{\perp}^{\mu\nu}}{x - \xi + i\epsilon} - \frac{i\epsilon_{\perp}^{\mu\nu}}{x + \xi - i\epsilon} \right) \right) \\
&+ M_{p\gamma^5,u} \left(\left(\frac{1}{4} - \frac{2}{3} \sin^2\theta_w \right) \left(\frac{-i\epsilon_{\perp}^{\mu\nu}}{x - \xi + i\epsilon} + \frac{i\epsilon_{\perp}^{\mu\nu}}{x + \xi - i\epsilon} \right) \right. \\
&\quad \left. + \frac{1}{4} \left(\frac{g_{\perp}^{\mu\nu}}{x - \xi + i\epsilon} + \frac{g_{\perp}^{\mu\nu}}{x + \xi - i\epsilon} \right) \right) \left. \right\} \quad (2.58)
\end{aligned}$$

with the abbreviations

$$M_{i,j} = \left\langle p_i \left| \bar{j} \left(\frac{-z}{2} \right) \gamma^+ j \left(\frac{z}{2} \right) \right| p_i \right\rangle, \quad (2.59)$$

$$M_{i\gamma^5,j} = \left\langle p_i \left| \bar{j} \left(\frac{-z}{2} \right) \gamma^+ \gamma^5 j \left(\frac{z}{2} \right) \right| p_i \right\rangle. \quad (2.60)$$

The index i labels the nucleon and the index j the quark flavor. So for different scattering amplitudes, where the target can be a proton or a neutron and the quark a u quark or a d quark the matrix corresponding elements $M_{i,j}$ and $M_{i\gamma^5,j}$ have to be replaced.

2.5.3 Total scattering amplitude

After having calculated the Compton amplitude we can include the exchanged particle as well as the leptonic part.

The scattering amplitude of the complete process reads

$$\mathcal{M} = \sum_{\lambda'=\pm} L^{\alpha\beta} g_{\alpha}^{\mu} T_{\mu\rho} \epsilon^{*\rho}(\lambda') \epsilon^{\sigma}(\lambda') g_{\beta}^{\nu} T_{\nu\sigma}^*. \quad (2.61)$$

and is illustrated in Fig. 2.6. $L^{\alpha\beta}$ is the leptonic tensor and $T_{\mu\rho}$ the hadronic tensor. The

polarization vectors of the photons are given by

$$\epsilon(+)= -\frac{1}{\sqrt{2}}\begin{pmatrix} 0 \\ 1 \\ i \\ 0 \end{pmatrix}, \quad \epsilon(-)= \frac{1}{\sqrt{2}}\begin{pmatrix} 0 \\ 1 \\ -i \\ 0 \end{pmatrix}, \quad \epsilon(0)= \frac{1}{\sqrt{2}}\begin{pmatrix} 1 \\ 0 \\ 0 \\ 0 \end{pmatrix}. \quad (2.62)$$

When computing unpolarized cross sections involving photons we have

$$-g_{\mu\nu} \approx \sum_{\text{polarizations}} \epsilon_{\mu}^* \epsilon_{\nu} \quad (2.63)$$

by virtue of the Ward identity. With this we arrive at

$$\begin{aligned} \mathcal{M} &= \sum_{\lambda=\pm,0} \sum_{\lambda'=\pm} \sum_{\lambda''=\pm,0} L^{\alpha\beta} \epsilon_{\alpha}^*(\lambda'') \epsilon^{\mu}(\lambda) T_{\mu\rho} \epsilon^{*\rho}(\lambda') \epsilon^{\sigma}(\lambda') \epsilon^{*\nu}(\lambda) \epsilon_{\beta}(\lambda'') T_{\nu\sigma}^* \\ &= \sum_{\lambda=\pm,0} \sum_{\lambda'=\pm} \sum_{\lambda''=\pm,0} L^{\alpha\beta} \epsilon_{\alpha}^*(\lambda'') \epsilon_{\beta}(\lambda'') \epsilon^{\mu}(\lambda) T_{\mu\rho} \epsilon^{*\rho}(\lambda') \epsilon^{*\nu}(\lambda) T_{\nu\sigma}^* \epsilon^{\sigma}(\lambda'). \end{aligned} \quad (2.64)$$

In the Compton amplitudes we have obtained a combination of $g_{\perp}^{\mu\nu}$ and $\epsilon_{\perp}^{\mu\nu}$ terms, see Eqs. 2.47, 2.51, 2.52 and 2.58, which are now combined with the polarization vectors. The quark helicity has to be conserved and since the photon in the final state is real, it has to be transverse. Thus the virtual boson can only have the polarization $\lambda = \pm$. The only non-vanishing contributions to Eq. 2.64 come from $\lambda = \lambda' = \pm$. All terms of mixed helicities disappear which confirms boson helicity conservation. We are now going to investigate the term $\epsilon^{\mu}(\lambda) T_{\mu\mu'} \epsilon^{*\mu'}(\lambda')$ in more detail to see which effect the different polarizations make. $\epsilon^{\mu}(\lambda)$ is the polarization vector of the exchanged particle γ , W^{\pm} or Z^0 and $\epsilon^{*\rho}(\lambda')$ of the outgoing real photon. We introduce the abbreviation α and β for the quark and the antiquark

$$\alpha = x - \xi + i\epsilon, \quad (2.65)$$

$$\beta = x - \xi - i\epsilon. \quad (2.66)$$

In the case of a photon scattering off a u quark inside a proton we get the results

$$\begin{aligned} \epsilon_{\mu}(-) T^{\mu\nu} \epsilon_{\nu}^*(-) &= -(ee_u)^2 \int \frac{d\lambda}{2\pi} dx e^{ix\lambda} \frac{1}{2} \left\{ -M_{pu} \left(\frac{1}{\alpha} + \frac{1}{\beta} \right) \right. \\ &\quad \left. + M_{p\gamma^5 u} \left(\frac{1}{\alpha} - \frac{1}{\beta} \right) \right\}, \end{aligned} \quad (2.67)$$

$$\begin{aligned} \epsilon_{\mu}(+) T^{\mu\nu} \epsilon_{\nu}^*(+) &= -(ee_u)^2 \int \frac{d\lambda}{2\pi} dx e^{ix\lambda} \frac{1}{2} \left\{ -M_{pu} \left(\frac{1}{\alpha} + \frac{1}{\beta} \right) \right. \\ &\quad \left. - M_{p\gamma^5 u} \left(\frac{1}{\alpha} - \frac{1}{\beta} \right) \right\}. \end{aligned} \quad (2.68)$$

Results for a d quark and for a neutron can be obtained by changing M_{ij} and the factor of e_u in front. Due to the factor of e_q in front it makes a difference if the photons scatter of a d or a u quark. It can be seen from Eqs. 2.67 and 2.68 that the propagators of quarks and

antiquarks contribute and thus both of them take part in the scattering process. In a similar way we obtain for the W^+

$$\epsilon_{\mu}(-)T^{\mu\nu}\epsilon_{\nu}^*(-) = \frac{-e_q e^2}{\sin\theta_w 2\sqrt{2}} \int \frac{d\lambda}{2\pi} dx e^{ix\lambda} \left\{ M_{pn} \left(\frac{1}{\alpha} \right) - M_{p\gamma^5 n} \left(\frac{1}{\alpha} \right) \right\}, \quad (2.69)$$

$$\epsilon_{\mu}(+)T^{\mu\nu}\epsilon_{\nu}^*(+) = \frac{-e_q e^2}{\sin\theta_w 2\sqrt{2}} \int \frac{d\lambda}{2\pi} dx e^{ix\lambda} \left\{ M_{pn} \left(\frac{1}{\beta} \right) - M_{p\gamma^5 n} \left(\frac{1}{\beta} \right) \right\}. \quad (2.70)$$

Firstly a right-handed positron decays into a right-handed antineutrino and a right-handed W^+ . This positively charged boson couples via weak interaction to a \bar{u} quark. Secondly a neutrino beam can emit a left-handed W^+ which then couples to a d quark.

For the W^- we have a similar behavior

$$\epsilon_{\mu}(-)T^{\mu\nu}\epsilon_{\nu}^*(-) = \frac{-e_q e^2}{\sin\theta_w 2\sqrt{2}} \int \frac{d\lambda}{2\pi} dx e^{ix\lambda} \left\{ M_{np} \left(\frac{1}{\alpha} \right) - M_{n\gamma^5 p} \left(\frac{1}{\alpha} \right) \right\}, \quad (2.71)$$

$$\epsilon_{\mu}(+)T^{\mu\nu}\epsilon_{\nu}^*(+) = \frac{e^2}{\sin\theta_w 2\sqrt{2}} \int \frac{d\lambda}{2\pi} dx e^{ix\lambda} \left\{ M_{np} \left(\frac{1}{\beta} \right) - M_{n\gamma^5 p} \left(\frac{1}{\beta} \right) \right\}. \quad (2.72)$$

A left-handed W^- can be emitted from a left-handed electron beam and couple to a \bar{u} quark while a right-handed W^- can be emitted from a right-handed antineutrino beam and couple to a d quark. This behavior is confirmed by Eqs. 2.71 and 2.72. Now we show the remaining weakly coupling boson, the Z^0 . Exemplifying the interacting with a u quark within a nucleon i we get

$$\begin{aligned} \epsilon_{\mu}(-)T^{\mu\nu}\epsilon_{\nu}^*(-) &= \frac{-e_q e^2}{\sin\theta_w \cos\theta_w} \int \frac{d\lambda}{2\pi} dx e^{ix\lambda} \frac{1}{2} \left\{ \left(\frac{1}{4} - \frac{2}{3} \sin^2\theta_w \right) \right. \\ &\quad \left\{ M_{iu} \left(\left(\frac{1}{\alpha} + \frac{1}{\beta} \right) + \frac{1}{4} \left(\frac{-1}{\alpha} - \frac{-1}{\beta} \right) \right) \right. \\ &\quad \left. \left. + M_{i\gamma^5 u} \left(\left(\frac{1}{\alpha} - \frac{1}{\beta} \right) + \frac{1}{4} \left(\frac{-1}{\alpha} + \frac{-1}{\beta} \right) \right) \right\} \right\} \end{aligned} \quad (2.73)$$

$$\begin{aligned} \epsilon_{\mu}(+)T^{\mu\nu}\epsilon_{\nu}^*(+) &= \frac{-e_q e^2}{\sin\theta_w \cos\theta_w} \int \frac{d\lambda}{2\pi} dx e^{ix\lambda} \frac{1}{2} \left\{ \left(\frac{1}{4} - \frac{2}{3} \sin^2\theta_w \right) \right. \\ &\quad \left\{ M_{iu} \left(\left(\frac{1}{\alpha} + \frac{1}{\beta} \right) + \frac{1}{4} \left(\frac{1}{\alpha} - \frac{1}{\beta} \right) \right) \right. \\ &\quad \left. \left. + M_{i\gamma^5 u} \left(\left(-\frac{1}{\alpha} + \frac{1}{\beta} \right) - \frac{1}{4} \left(\frac{1}{\alpha} + \frac{1}{\beta} \right) \right) \right\} \right\}. \end{aligned} \quad (2.74)$$

As in the photon case the quarks and the antiquarks are involved in the scattering process. Now we can consider the behavior of the scattering amplitude \mathcal{M} .

Now we insert the just calculated terms $\epsilon_\mu T^{\mu\nu} \epsilon_\nu^*$ into the amplitude. We start with the photon, recalling F^q and \tilde{F}^q from Eqs. 2.1 and 2.2. The amplitude for right- (left-)handed photons is proportional to

$$\mathcal{M} \sim e_q^2 \left(\frac{\pm 1}{\alpha} (\mp F^q + \tilde{F}^q) - \frac{1}{\beta} (F^q \mp \tilde{F}^q) \right), \quad (2.75)$$

the upper (lower) sign belonging right- (left-) handed photons. Because we have a right-handed photon coupling to a quark as well as a left-handed photon coupling to an antiquark this gives access to the difference of F^q and \tilde{F}^q . Accordingly, a left-handed photon coupling to a quark or a right-handed photon coupling to an antiquark gives access to the sum of F^q and \tilde{F}^q . Besides \mathcal{M} is proportional to e_q and we can therefore distinguish between u and d quarks due to their different charges. To separate F^q and \tilde{F}^q for the single flavors one needs combinations of u and d quarks inside the proton and in addition to the proton either combinations of the neutron or one can use the weak current which provides a different combination of u and d quark distributions in F^q and \tilde{F}^q as given in the following. To have the distribution inside the neutron one can for example resort to the deuteron, since the neutron is no stable particle. Here we will stick to weak currents.

One obtains the following proportionalities for the W^+ exchange considering positive polarization

$$\mathcal{M} \sim \frac{e_q}{\alpha} (F^q - \tilde{F}^q) \quad (2.76)$$

and for negative polarization

$$\mathcal{M} \sim \frac{e_q}{\beta} (F^q - \tilde{F}^q). \quad (2.77)$$

Thus the W^+ couples only to left-handed fermions and right-handed antifermions, respectively. In both cases \mathcal{M} is proportional to the difference of F^q and \tilde{F}^q . Thus the W^+ cannot distinguish between the polarization of the final state photon. The difference $F^q - \tilde{F}^q$ for $x > 0$ projects out the left-handed part of the quark distribution while for $x < 0$ the right-handed part is projected out. Depending on the factor e_q we can see whether a u or d quark had coupled to the W^+ boson.

In the case of a right-handed W^- we find

$$\mathcal{M} \sim \frac{e_q}{\beta} (F^q - \tilde{F}^q) \quad (2.78)$$

and for a left-handed

$$\mathcal{M} \sim \frac{e_q}{\alpha} (F^q - \tilde{F}^q). \quad (2.79)$$

Due to charge conservation a right-handed W^- couples to a \bar{d} quark and a left-handed W^- to a u quark.

Furthermore we take into account the Z^0 . A right-handed Z^0 coupling to a u quark leads to

$$\mathcal{M} \sim \frac{1}{\alpha} \left(\frac{1}{2} - \frac{2}{3} \sin^2 \vartheta \right) (F^q - \tilde{F}^q) - \frac{1}{\beta} \frac{2}{3} \sin^2 \vartheta (F^q + \tilde{F}^q), \quad (2.80)$$

and a left-handed Z^0 leads to

$$\mathcal{M} \sim -\frac{1}{\alpha} \frac{2}{3} \sin^2\vartheta (F^q + \tilde{F}^q) + \frac{1}{\beta} \left(\frac{1}{2} - \frac{2}{3} \sin^2\vartheta \right) (F^q - \tilde{F}^q). \quad (2.81)$$

Having a look at a right-handed Z^0 coupling to a d quark shows

$$\mathcal{M} \sim \left(\frac{1}{\alpha} \left(-\frac{1}{2} + \frac{1}{3} \sin^2\vartheta \right) (F^q - \tilde{F}^q) + \frac{1}{\beta} \frac{1}{3} \sin^2\vartheta (F^q + \tilde{F}^q) \right) \quad (2.82)$$

and for negative polarization

$$\mathcal{M} \sim \left(\frac{1}{\alpha} \frac{1}{3} \sin^2\vartheta (F^q + \tilde{F}^q) + \frac{1}{\beta} \left(\frac{1}{2} - \frac{1}{3} \sin^2\vartheta \right) (F^q - \tilde{F}^q) \right). \quad (2.83)$$

Here we have a similar situation as in the photon case. But due to the difference in the coupling to fermions it can be distinguished whether the Z^0 was left- or right-handed and whether it scattered of a u or d quark. From these calculations we see that we either get the difference or the sum of F^q and \tilde{F}^q . These quantities contain the GPDs with different factors in front. We give an overview for the different exchange particles and the corresponding combinations of F^q and \tilde{F}^q for each helicity separately. These contain the GPDs and are therefore of great interest. The results for positive helicity are summarized in Tab. 2.1. Moreover the results for negative helicity are given in Tab. 2.2.

Table 2.1: Matrix elements involving different exchange particles of positive helicity showing the proportionality to the combinations of F^q and \tilde{F}^q which include the GPDs H , \tilde{H} , E and \tilde{E} . The abbreviations α and β for the quark and antiquark are given in Eqs. 2.65 and 2.66.

matrix element	boson	\mathcal{M} proportional to
$\langle P \bar{d}d P\rangle$	γ^*	$-\frac{1}{9} \left(\frac{1}{\alpha} (F^d - \tilde{F}^d) + \frac{1}{\beta} (F^d + \tilde{F}^d) \right)$
$\langle P \bar{u}u P\rangle$	γ^*	$-\frac{4}{9} \left(\frac{1}{\alpha} (F^u - \tilde{F}^u) + \frac{1}{\beta} (F^u + \tilde{F}^u) \right)$
$\langle P \bar{d}d P\rangle$	Z^0	$-\left(\frac{1}{\alpha} \left(-\frac{1}{2} + \frac{1}{3} \sin^2\vartheta \right) (F^d - \tilde{F}^d) + \frac{1}{\beta} \frac{1}{3} \sin^2\vartheta (F^d + \tilde{F}^d) \right)$
$\langle P \bar{u}u P\rangle$	Z^0	$\left(\frac{1}{\alpha} \left(\frac{1}{2} - \frac{2}{3} \sin^2\vartheta \right) (F^u - \tilde{F}^u) - \frac{1}{\beta} \frac{2}{3} \sin^2\vartheta (F^u + \tilde{F}^u) \right)$
$\langle P \bar{u}d N\rangle$	W^+	$\frac{2}{3} \frac{1}{\alpha} (F^u - \tilde{F}^u)$
$\langle N \bar{d}u P\rangle$	W^-	$-\frac{1}{3} \frac{1}{\beta} (F^d - \tilde{F}^d)$

Table 2.2: Matrix elements involving different exchange particles of negative helicity showing the proportionality to the combinations of F^q and \tilde{F}^q which include the GPDs H , \tilde{H} , E and \tilde{E} . The abbreviations α and β for the quark and antiquark are given in Eqs. 2.65 and 2.66.

matrix element	boson	\mathcal{M} proportional to
$\langle P \bar{d}d P\rangle$	γ^*	$-\frac{1}{9}\left(\frac{1}{\alpha}(F^d + \tilde{F}^d) + \frac{1}{\beta}(F^d - \tilde{F}^d)\right)$
$\langle P \bar{u}u P\rangle$	γ^*	$-\frac{4}{9}\left(\frac{1}{\alpha}(F^u + \tilde{F}^u) + \frac{1}{\beta}(F^u - \tilde{F}^u)\right)$
$\langle P \bar{d}d P\rangle$	Z^0	$\left(\frac{1}{\alpha}\frac{1}{3}\sin^2\vartheta(F^d + \tilde{F}^d) - \frac{1}{\beta}\left(-\frac{1}{2} + \frac{1}{3}\sin^2\vartheta\right)(F^d - \tilde{F}^d)\right)$
$\langle P \bar{u}u P\rangle$	Z^0	$\left(-\frac{1}{\alpha}\frac{2}{3}\sin^2\vartheta(F^u + \tilde{F}^u) + \frac{1}{\beta}\left(\frac{1}{2} - \frac{2}{3}\sin^2\vartheta\right)(F^u - \tilde{F}^u)\right)$
$\langle P \bar{u}d N\rangle$	W^+	$\frac{2}{3}\frac{1}{\beta}(F^u - \tilde{F}^u)$
$\langle N \bar{d}u P\rangle$	W^-	$-\frac{1}{3}\frac{1}{\alpha}(F^d - \tilde{F}^d)$

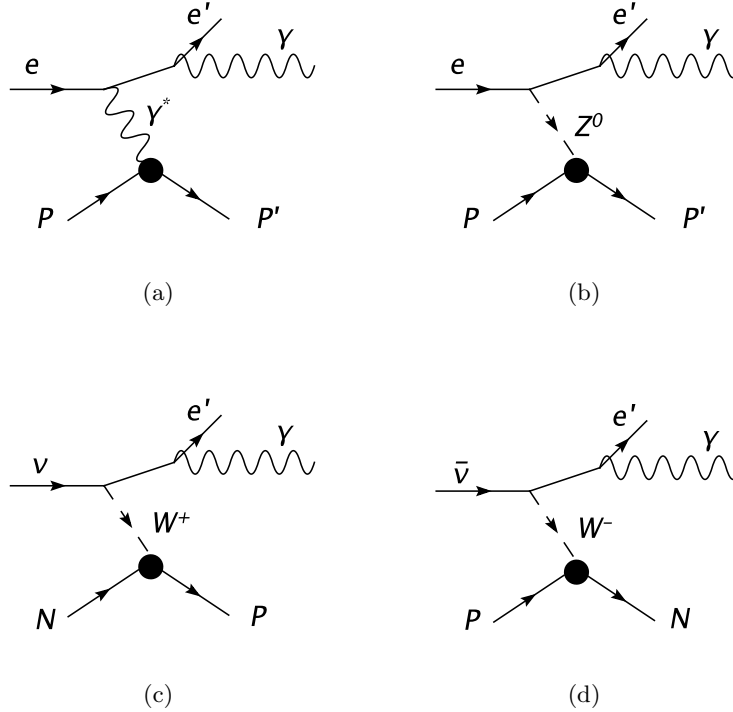


Figure 2.7: Examples for the Bethe-Heitler process for γ , Z^0 , W^+ and W^- exchange.

2.5.4 DVCS and Bethe–Heitler

So far we have considered only Compton scattering. But there is a second process, having the same final state, the Bethe–Heitler (BH) process. In this reaction the electron emits two photons, a real photon and a virtual photon which is absorbed by the proton and changes the momentum of the proton. Examples of the Bethe–Heitler process are depicted in Fig. 2.7, where we have not drawn any crossed graphs. Deeply virtual Compton scattering and the Bethe–Heitler process cannot be distinguished experimentally. To compute the cross section both contributions have to be taken into account. To calculate the Bethe–Heitler amplitude we need the form factors which describe the coupling of the electron to the nucleon given by the blob in Fig. 2.7. The ratio of the Compton to the Bethe–Heitler cross section is approximately given by

$$|\mathcal{M}_{\text{DVCS}}|^2 : |\mathcal{M}_{\text{BH}}|^2 \sim \left(\frac{1}{Q^2} \frac{1}{1-\epsilon} \right) : \left(-\frac{1}{t} \frac{1}{\epsilon} \right), \quad (2.84)$$

where ϵ is defined as

$$\epsilon = \frac{1-y-\delta}{1-y+y^2/2+\delta} \quad \text{with} \quad \delta = \frac{y^2 x_B^2 m_p^2}{Q^2}. \quad (2.85)$$

Their interference term is of the order of their geometric mean. Thus in a kinematic range where $Q^2 \gg t$ the Bethe–Heitler contribution clearly dominates, except for ϵ being close to one, which entails that y is close to zero.

2.5.5 Isospin

Isospin provides a possibility to connect the different matrix elements appearing in the scattering amplitude of DVCS. Measurements from deeply inelastic Compton scattering combined with measurements from weak current between the electron and the proton lead to different combinations of GPDs contained in these matrix elements. Strongly interacting particles form charge multiplets as for example the nucleons (p, n) or the pions (π^+, π^-, π^0). Particles belonging to the same multiplet are observed to have similar properties and behave similar under strong interaction, which indicates the existence of an invariance principle. This isospin invariance is given by a three-dimensional rotation group. One can introduce operators I_{\pm} which can transform a charge state to its adjacent charge state. They fulfill the condition $I_+^\dagger = I_-$. Taking for example the multiplet consisting of a proton and a neutron, where $|p\rangle$ and $|n\rangle$ are the base vectors one finds the following matrix representation for the operators

$$I_+ \Rightarrow \begin{bmatrix} 0 & 1 \\ 0 & 0 \end{bmatrix}, \quad I_- \Rightarrow \begin{bmatrix} 0 & 0 \\ 1 & 0 \end{bmatrix}. \quad (2.86)$$

These operators I_+ and I_- obey the commutation relations

$$[I_3, I_{\pm}] = \pm I_{\pm}, \quad [I_+, I_-] = 2I_3. \quad (2.87)$$

Defining the hermitian operators $I_1 = \frac{1}{2}(I_+ + I_-)$ and $I_2 = \frac{1}{2i}(I_+ - I_-)$ the Lie algebra can be written as

$$[I_i, I_j] = \sum_{k=1}^3 i\epsilon_{ijk} I_k. \quad (2.88)$$

Isospin multiplets correspond to an irreducible representation of this algebra. State vectors of strongly interacting particles can be denoted by $|I, m, \tau\rangle$ where $I(I+1)$ and m are the eigenvalues of I^2 and I_3 . With τ we denote the remaining quantum numbers that are necessary to fully describe the particle [88]. Strongly interacting particles are invariant under operations of the Lie algebra in Eq. 2.88. Isospin symmetry imposes restrictions on the form of the amplitude $\langle f|S|i\rangle$ of the process $a + b \rightarrow c + d$. Neglecting electromagnetic interactions, the initial state is composed of strongly interacting particles belonging to an isospin multiplet (see *e.g.* [88]),

$$\begin{aligned} |i\rangle &= |I_a, m_a, \tau_a\rangle \otimes |I_b, m_b, \tau_b\rangle \\ &= \sum_I \langle I_a I_b m_a m_b | I m \rangle |I, m, \tau\rangle \end{aligned} \quad (2.89)$$

with $I = m_a + m_b, m_a + m_b - 1, \dots, |m_a - m_b|$ and $m = m_a + m_b = m_c + m_d$. The coefficients in the last line of Eq. 2.89 are the Clebsch-Gordon coefficients. In analogy this can be done for the final state and we find that

$$\begin{aligned} \langle f|S|i\rangle &= \sum_I \langle I_c m_c, I_d m_d | S_{\tau\tau'} | I_a m_a, I_b m_b \rangle \\ &= \sum_I \langle m_c m_d | I m \rangle \langle m_a m_b | I m \rangle S_{\tau\tau'}(I). \end{aligned} \quad (2.90)$$

For the nucleons and quarks the isospin doublets are

$$\begin{pmatrix} p \\ n \end{pmatrix}, \quad \begin{pmatrix} u \\ d \end{pmatrix}. \quad (2.91)$$

The antiparticle states are coupled by Clebsch-Gordon coefficients. This means, that not the multiplets which arise after charge conjugation are transformed, but those particles that transform under isospin as the corresponding particles. Therefore we have a minus sign in the upper part of these doublets:

$$\begin{pmatrix} -\bar{n} \\ \bar{p} \end{pmatrix}, \quad \begin{pmatrix} -\bar{d} \\ \bar{u} \end{pmatrix}. \quad (2.92)$$

Each nucleon has isospin $I = \frac{1}{2}$ with $I_3 = \frac{1}{2}$ for the proton and $I_3 = -\frac{1}{2}$ for the neutron.

Quarks can be coupled by using Clebsch-Gordon coefficients in the same way as the nucleons are coupled. The calculation of the matrix elements leads to the following relations:

$$\begin{aligned} {}_{\tau'} \langle \bar{p} | \bar{u} u | p \rangle_{\tau} &= \sum_I \left\langle -\frac{1}{2} \frac{1}{2} \middle| 10 \right\rangle \left\langle -\frac{1}{2} \frac{1}{2} \middle| 10 \right\rangle S_{\tau\tau'}(I) \\ &= \frac{1}{2} S_{\tau\tau'}(0) + \frac{1}{2} S_{\tau\tau'}(1), \end{aligned} \quad (2.93)$$

$$\begin{aligned} {}_{\tau'} \langle \bar{p} | \bar{d} d | p \rangle_{\tau} &= - \sum_I \left\langle \frac{1}{2} - \frac{1}{2} \middle| 10 \right\rangle \left\langle -\frac{1}{2} \frac{1}{2} \middle| 10 \right\rangle S_{\tau\tau'}(I) \\ &= \frac{1}{2} S_{\tau\tau'}(0) - \frac{1}{2} S_{\tau\tau'}(1), \end{aligned} \quad (2.94)$$

$${}_{\tau'} \langle \bar{p} | \bar{u} d | n \rangle_{\tau} = S_{\tau\tau'}(1), \quad (2.95)$$

$${}_{\tau'} \langle \bar{n} | \bar{d} u | p \rangle_{\tau} = S_{\tau\tau'}(1), \quad (2.96)$$

where $S_{\tau\tau'}$ is now a function depending only on the isospin. Altogether one obtains the following relations for quarks in the nucleons

$$\langle p|\bar{u}u|p\rangle = \langle n|\bar{d}d|n\rangle = \frac{1}{2}S_{\tau\tau'}(0) + \frac{1}{2}S_{\tau\tau'}(1), \quad (2.97)$$

$$\langle p|\bar{d}d|p\rangle = \langle n|\bar{u}u|n\rangle = \frac{1}{2}S_{\tau\tau'}(0) - \frac{1}{2}S_{\tau\tau'}(1), \quad (2.98)$$

$$\langle p|\bar{u}d|n\rangle = \langle n|\bar{d}u|p\rangle = S_{\tau\tau'}(1). \quad (2.99)$$

This shows that the matrix elements are given as functions of two isospins only. Now it is obvious that $\langle p|\bar{u}u + \bar{d}d|p\rangle = S_{\tau\tau'}(0)$. By including $[I_+, I_-]$ we obtain

$${}_{\tau'}\langle I=1, I_3=0|I=1, I_3=0\rangle_{\tau} = {}_{\tau'}\langle I=1, I_3=1|I=1, I_3=1\rangle_{\tau}, \quad (2.100)$$

thus the matrix elements are independent of I_3 .

Here we see that isospin relates matrix elements including protons, neutrons and the transition from proton to neutron and from a neutron to a proton. Thus one can determine the transition matrix element from the knowledge of the proton and neutron matrix elements.

Chapter 3

Scattering off a virtual pion

Pions are the lightest existing hadrons. According to the standard model they are composed of quarks (u and d) and antiquarks (\bar{u} and \bar{d}). The spins of the two quarks are aligned in such a way, that the resulting spin of the pion is zero. Moreover, pions are pseudoscalars under parity transformation. Altogether there are three pions, π^0 , π^+ and π^- forming an isospin triplet with $I = 1$. Pions were theoretically predicted by Yukawa as the carrier of the strong nuclear force. The first pions were found in 1947 by Powell and Lattes [7]. Due to the spinless nature of the pion, it is much simpler than the spin- $\frac{1}{2}$ nucleons. A generalized parton distribution for the pion is needed to describe exclusive processes involving a pion. Many models have been proposed so far for the pion GPDs [89, 90, 91, 92]. Experiments can provide a pion beam, but there is a lack of pions as a target. However, the investigation of a process like $ep \rightarrow e'n\pi^+\gamma$ in the regime where the transition between the proton and the neutron occurs via a single pion emission enables such studies. The final state pion is a π^+ , but we omit the $+$ for simplicity in the following. Indeed, this reaction contains the DVCS process $e\pi \rightarrow e'\pi'\gamma$. The proton emits a pion and the electron scatters off that pion. Although the emitted pion is virtual, we can take it as a pion source and keep the virtuality small, allowing for an on-shell treatment. To calculate this process we divide it into two modules: a proton emitting a pion and transforming into a neutron and a photon scattering off a pion. They are connected by the pion propagator. Due to the analogy with DVCS, discussed in Sec. 2.5.1, we call this process pion DVCS. The separation of the hadronic part and the scattering off a virtual pion is depicted in Fig. 3.1.

The structure of this chapter is as follows: we introduce the kinematics of the full process $ep \rightarrow e'n\pi\gamma$. In addition to that we introduce the kinematics of the pion-photon center-of-mass frame. Thereafter we give the most important ingredients of the cross section $ep \rightarrow e'n\pi\gamma$, which are the phase space and the scattering amplitude. Since we decompose the process in modules we need the scattering amplitude of $e\pi \rightarrow e'\pi'\gamma$ which we give in the $e\pi$ center-of-mass frame. To finally compute the total cross section we need a model for the pion GPD on which we focus in Sec. 3.6. In the end we calculate the total cross section of this reaction and we include in our calculation kinematical constraints arising due to the design of the HERMES detector at DESY and the CLAS detector at JLab to predict measurable cross sections.

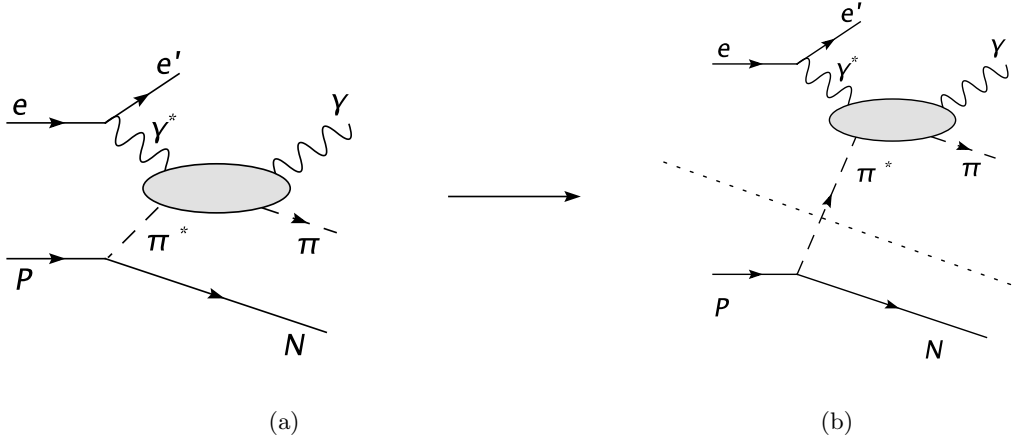


Figure 3.1: For the calculation we separate the $ep \rightarrow e' \pi \gamma n$ process into a hadronic part and deeply virtual Compton scattering off a pion which are connected by a propagating pion.

3.1 The $ep \rightarrow e' \pi \gamma n$ process

In this section we consider the process $ep \rightarrow e' \pi \gamma n$ depicted in Fig. 3.2 and 3.3, where the initial electron emits a virtual photon and the initial proton emits a virtual pion. These virtual particles then scatter and we find a real photon, a real pion, the scattered electron and a neutron in the final state. All variables belonging to a special particle are labeled by an index that represents the particle, as p_e , and $p_{e'}$ for the electron and the scattered electron, respectively.

The aim is to compute the total cross section for the process $ep \rightarrow e' \pi \gamma n$. Depending on the size of the cross section it might be possible to compare it to experimental data. The general formula for the differential cross section is given by

$$d\sigma|_{ep \rightarrow e' \pi \gamma n} = \frac{1}{F_{ep}} |\mathcal{T}_{ep}(p_e p_p \rightarrow \{p_f\})|^2 d\Phi_4 \quad (3.1)$$

where F_{ep} is the flux factor, Φ_4 the phase space of the four particle final state and \mathcal{T}_{ep} the scattering amplitude of the process. In this chapter we derive these single components of the cross section in detail and compute the total cross section as well as beam charge and beam polarization asymmetries.

3.1.1 Electron-proton center-of-mass frame

The experiment takes place in the laboratory frame of the proton. This frame is connected via a z -boost with the electron-proton center-of-mass frame. In this ep frame we have the proton and the electron colliding head-on and moving along the z -axis, the electron going in positive direction. The final-state electron and the neutron are moving along arbitrary directions given by their azimuthal and polar angles, $\psi_{e'}$, ψ_n , $\vartheta_{e'}$ and ϑ_n . We define the

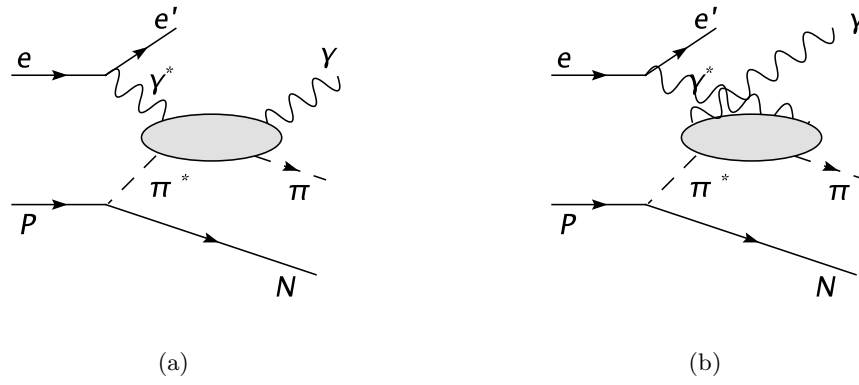


Figure 3.2: Deeply virtual Compton scattering off a virtual pion emitted from a proton and b) its crossed graph.

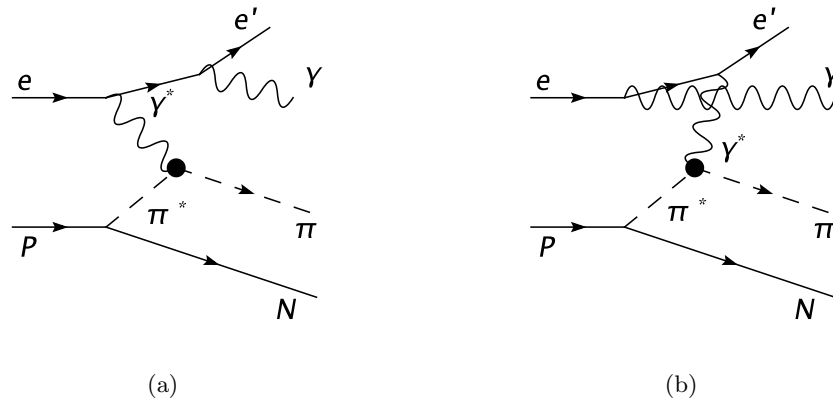


Figure 3.3: a) The Bethe–Heitler process of $ep \rightarrow e\pi\gamma n$ and b) the crossed graph.

particle four-momenta in the following way

$$p_e = (E_e, 0, 0, |\vec{p}_e|), \quad (3.2)$$

$$p_{e'} = (E_{e'}, |\vec{p}_{e'}| \sin\vartheta_{e'} \cos\psi_{e'}, |\vec{p}_{e'}| \sin\vartheta_{e'} \sin\psi_{e'}, |\vec{p}_{e'}| \cos\vartheta_{e'}), \quad (3.3)$$

$$p_q = p_e - p_{e'}, \quad (3.4)$$

$$p_p = (E_p, 0, 0, -|\vec{p}_p|), \quad (3.5)$$

$$p_n = (E_n, |\vec{p}_n| \sin\vartheta_n \cos\psi_n, |\vec{p}_n| \sin\vartheta_n \sin\psi_n, -|\vec{p}_n| \cos\vartheta_n), \quad (3.6)$$

$$p_\pi = p_p - p_n. \quad (3.7)$$

First of all we want to express a differential cross section in terms of eight invariant variables. Therefore all energies, momenta and angles have to be given in those variables. DVCS off a proton has five invariant variables, which are x_B , Q^2 , t , ψ_n and ψ_e . In the reaction considered here, we have in addition a pion in the final state, which leads to three additional invariants. One is chosen to be x_π , giving approximately the ratio of the pion and the proton energy, then we define t_π being the difference between the initial- and final-state pion and $\phi_\pi^{\pi\gamma}$ which is the angle between the electron and the hadron plane. The angle $\phi_\pi^{\pi\gamma}$ is also the scattering angle of the pion in the centre-of-mass frame of the photon and the pion. Altogether we have

$$-Q^2 = (p_e - p_{e'})^2, \quad (3.8)$$

$$x_B = \frac{Q^2}{2p_p \cdot p_q}, \quad (3.9)$$

$$t = (p_p - p_n)^2, \quad (3.10)$$

$$x_\pi = \frac{p_\pi \cdot p_e}{p_p \cdot p_e}, \quad (3.11)$$

$$t_\pi = (p_\pi - p_{\pi'})^2, \quad (3.12)$$

$$\psi_n, \quad \psi_e, \quad \phi_\pi^{\pi\gamma} \quad (3.13)$$

describing the process. We denote the initial, virtual pion by p_π and the final-state pion by $p_{\pi'}$. In addition we introduce the Mandelstam variable s

$$s = \frac{Q^2}{x_B y} + m_p^2, \quad (3.14)$$

which is the center-of-mass energy of the electron-proton collision. For the HERMES experiment with an electron beam energy of 22.75 GeV, s amounts to 51.81 GeV², while for the 12 GeV upgrade at JLab¹ s will be 22.5 GeV². To compute the energies, momenta and angles of the participating particles, and to connect the different kinematical frames in the following, we need some frame-independent Lorentz-invariant scalar products, $p_i \cdot p_j$, in terms of the

¹For CLAS the beam energy will only be 11 GeV

invariants:

$$\begin{aligned}
 p_p \cdot p_q &= \frac{Q^2}{2x_B}, & p_n \cdot p_p &= \frac{1}{2}(m_p^2 + m_n^2 - t), \\
 p_e \cdot p_{e'} &= \frac{1}{2}Q^2, & p_n \cdot p_e &= \frac{1}{2} \frac{Q^2}{x_B y} (1 - x_\pi), \\
 p_e \cdot p_p &= \frac{1}{2} \frac{Q^2}{x_B y}, & p_\pi \cdot p_e &= \frac{1}{2} \frac{Q^2}{x_B y} x_\pi.
 \end{aligned} \tag{3.15}$$

Now we can focus on the energies and momenta of the first particles. For the colliding electron and proton we find

$$E_e = \frac{s - m_p^2}{2\sqrt{s}}, \quad |\vec{p}_e| = \frac{s - m_p^2}{2\sqrt{s}}, \tag{3.16}$$

$$E_p = \frac{s + m_p^2}{2\sqrt{s}}, \quad |\vec{p}_p| = \frac{s - m_p^2}{2\sqrt{s}}, \tag{3.17}$$

for the final-state electron the results are

$$E_{e'} = \frac{s - m_p^2 + Q^2(1 - \frac{1}{x})}{2\sqrt{s}} = |\vec{p}_{e'}|, \tag{3.18}$$

$$\cos\vartheta_{e'} = \frac{1 - y - xy - \frac{2m_p^2 x^2 y^2}{Q^2}}{1 - y + x}, \tag{3.19}$$

and moreover the neutron components are given by

$$E_n = \frac{(s - m_p^2)(1 - x_\pi) + m_p^2 + m_n^2 - t}{2\sqrt{s}}, \tag{3.20}$$

$$|\vec{p}_n| = \sqrt{\frac{1}{4s}((s - m_p^2)(1 - x_\pi) + m_p^2 + m_n^2 - t)^2 - m_n^2}, \tag{3.21}$$

$$\cos\vartheta_n = \frac{(s + m_p^2)(1 - x_\pi) - m_p^2 - m_n^2 + t}{\sqrt{((s - m_p^2)(1 - x_\pi) + m_p^2 + m_n^2 - t)^2 - 4sm_n^2}}, \tag{3.22}$$

with $m_n = 938.6$ MeV. Still missing are the final pion and photon which cannot be calculated straightforward at this point, but will be determined later in this work. It is very important, especially for experimentalists, to know where to expect the particles inside the detector. With help of the just derived quantities we are able to compute further scalar products which

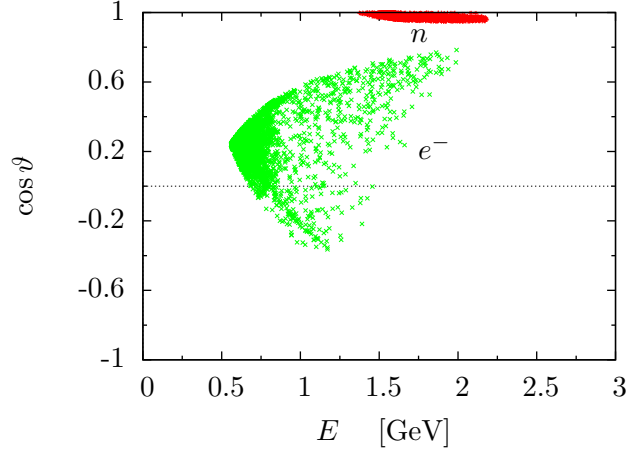


Figure 3.4: Electron (green) and neutron (red) distribution of their energy to the cosine of their scattering angle in the electron proton center-of-mass frame.

will be of great interest in forthcoming calculations,

$$\begin{aligned}
 p_{e'} \cdot p_n &= E_{e'} E_n - |\vec{p}_{e'}| |\vec{p}_n| \left(\cos(\psi_e - \psi_n) \sqrt{1 - \cos^2 \vartheta_e} \sqrt{1 - \cos^2 \vartheta_n} - \cos \vartheta_e \cos \vartheta_n \right) \\
 &\approx \frac{1}{2} \frac{Q^2}{xy} (1 - x_\pi)(1 - y) + \mathcal{O}(m_p^2), \tag{3.23}
 \end{aligned}$$

$$\begin{aligned}
 p_\pi \cdot p_{e'} &= \frac{1}{2} \frac{Q^2}{xy} (1 - y) - p_{e'} \cdot p_n \\
 &\approx \frac{1}{2} \frac{Q^2}{xy} x_\pi (1 - y) + \mathcal{O}(m_p^2), \tag{3.24}
 \end{aligned}$$

$$\begin{aligned}
 p_\pi \cdot p_q &= \frac{1}{2} \frac{Q^2}{xy} (y + x_\pi - 1) + p_{e'} \cdot p_n \\
 &\approx \frac{Q^2 x_\pi}{2x_B} + \mathcal{O}(m_p^2). \tag{3.25}
 \end{aligned}$$

For simplicity we approximated the scalar products in the limit of $Q^2 \gg m^2, t$. If we take a closer look at the scattering angles of Eqs. 3.19 and 3.22 we see that the neutron is moving very close to the z -axis

$$\cos \vartheta_n^R \rightarrow 1 \tag{3.26}$$

while the electron has not such a preferred scattering region. In Fig. 3.4 we have plotted the cosine of the polar angle versus the energy for the scattered electron and neutron. This shows where these particles are expected to be. The points are produced with a numerical program we use for the calculation of the total cross section. Thus also this plot shows, that the neutron in the final state tends to have only a very small scattering angle while the electron is spread over a broad range.

Regarding the scattered neutron there are two boundary conditions on t coming from the minimum and maximum scattering angle $\cos \vartheta_n = \pm 1$ corresponding to forward and backward

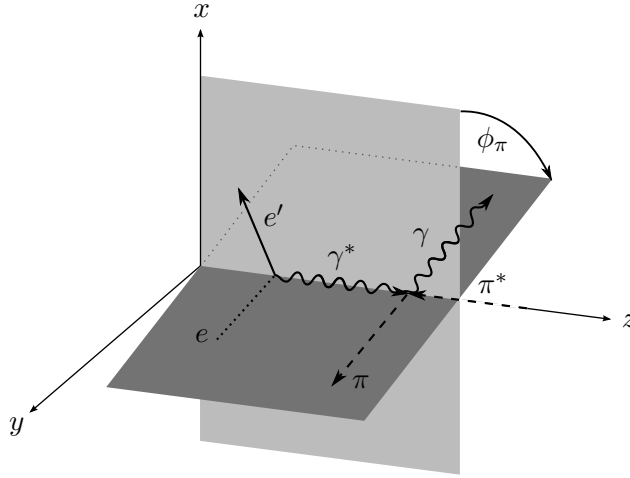


Figure 3.5: Pion-photon scattering in the pion-photon center-of-mass frame.

scattering. In the process considered here we get for both conditions the same restriction on t given by

$$t_0 = -\frac{x_\pi(m_p^2(1+x_\pi) - m_n^2)}{1-x_\pi}. \quad (3.27)$$

This is the minimum of t , it is the smallest value of $|t|$. Its value $|t|$ has to be bigger than zero, because the final-state photon is real and therefore we need at least some momentum transfer to produce this photon.

3.1.2 Kinematics for the $\pi \gamma \rightarrow \pi' \gamma'$ subprocess

In a next step we focus on the subprocess $\pi \gamma \rightarrow \pi' \gamma'$ and it is convenient to work in the center-of-mass frame of the pion and the photon. The axes are chosen in such a way that the initial γ and π are moving along the z -axis. The photon is moving along the positive z -direction and the electron plane identifies with the x - z plane as shown in Fig. 3.5.

We further define the center-of-mass energy of the process

$$\begin{aligned} s_\pi &= (p_q + p_\pi)^2 \\ &\approx \frac{Q^2}{x_B}(x_\pi - x_B) + \mathcal{O}(m^2). \end{aligned} \quad (3.28)$$

The approximated form of s_π shows that we need to fulfill the condition

$$x_\pi > x_B \quad (3.29)$$

to remain in the kinematically allowed region, where $s_\pi > 0$.

In the pion-photon frame we label all quantities by the superscript $\pi\gamma$. The four-momenta of the initial pion and photon are defined as

$$p_\pi^{\pi\gamma} = -|\vec{p}_\pi|^{\pi\gamma} \vec{e}_z, \quad (3.30)$$

$$p_q^{\pi\gamma} = |\vec{p}_q|^{\pi\gamma} \vec{e}_z, \quad (3.31)$$

while the electrons are defined to be in the x - z plane

$$p_{e'}^{\pi\gamma} = \begin{pmatrix} E_{e'}^{\pi\gamma} \\ |\vec{p}_{e'}|^{\pi\gamma} \sin\vartheta_{e'}^{\pi\gamma} \\ 0 \\ |\vec{p}_{e'}|^{\pi\gamma} \cos\vartheta_{e'}^{\pi\gamma} \end{pmatrix}, \quad (3.32)$$

$$p_e^{\pi\gamma} = \begin{pmatrix} E_e^{\pi\gamma} \\ |\vec{p}_e|^{\pi\gamma} \sin\vartheta_e^{\pi\gamma} \\ 0 \\ |\vec{p}_e|^{\pi\gamma} \cos\vartheta_e^{\pi\gamma} \end{pmatrix}. \quad (3.33)$$

Finally we have the scattered pion with the coordinates

$$p_{\pi'}^{\pi\gamma} = \begin{pmatrix} E_{\pi'}^{\pi\gamma} \\ -|\vec{p}_{\pi'}|^{\pi\gamma} \sin\vartheta_{\pi'}^{\pi\gamma} \cos\phi_{\pi}^{\pi\gamma} \\ -|\vec{p}_{\pi'}|^{\pi\gamma} \sin\vartheta_{\pi'}^{\pi\gamma} \sin\phi_{\pi}^{\pi\gamma} \\ |\vec{p}_{\pi'}|^{\pi\gamma} \cos\vartheta_{\pi'}^{\pi\gamma} \end{pmatrix}. \quad (3.34)$$

The angle $\phi_{\pi}^{\pi\gamma}$ is the scattering angle of the final photon, measured from the positive x -axis, as shown in Fig. 3.5. The angle of the scattered pion is $\phi_{\pi}^{\pi\gamma} + \pi$. The energies and momenta expressed through the invariants for the initial pion and photon are

$$|\vec{p}_{\pi}|^{\pi\gamma} = \sqrt{\left(\frac{s_{\pi} + t + Q^2}{2\sqrt{s_{\pi}}}\right)^2 - t}, \quad E_{\pi}^{\pi\gamma} = \frac{s_{\pi} + t + Q^2}{2\sqrt{s_{\pi}}}, \quad (3.35)$$

$$|\vec{p}_q|^{\pi\gamma} = \sqrt{\left(\frac{s_{\pi} - t - Q^2}{2\sqrt{s_{\pi}}}\right)^2 + Q^2}, \quad E_{\gamma}^{\pi\gamma} = \frac{s_{\pi} - t - Q^2}{2\sqrt{s_{\pi}}}, \quad (3.36)$$

and for the final-state pion and photon

$$|\vec{p}_{\pi'}|^{\pi\gamma} = \frac{s_{\pi} - m_{\pi}^2}{2\sqrt{s_{\pi}}}, \quad E_{\pi'}^{\pi\gamma} = \frac{s_{\pi} + m_{\pi}^2}{2\sqrt{s_{\pi}}}, \quad (3.37)$$

$$|\vec{p}_{q'}|^{\pi\gamma} = \frac{s_{\pi} - m_{\pi}^2}{2\sqrt{s_{\pi}}}, \quad E_{\gamma'}^{\pi\gamma} = \frac{s_{\pi} - m_{\pi}^2}{2\sqrt{s_{\pi}}}. \quad (3.38)$$

The scattering angle of the final pion is given by

$$\cos\vartheta_{\pi'}^{\pi\gamma} = \frac{t_{\pi} - t - m_{\pi}^2 + 2E_{\pi}^{\pi\gamma}E_{\pi'}^{\pi\gamma}}{-2|\vec{p}_{\pi}|^{\pi\gamma}|\vec{p}_{\pi'}|^{\pi\gamma}}. \quad (3.39)$$

Since the pion and the photon are scattered back-to-back it is sufficient to have $\cos\vartheta_{\pi'}^{\pi\gamma}$ for both particles.

Let us consider the final pion in more detail. For our process we require t_{π} to be small. In this kinematics the value of $\cos\vartheta_{\pi'}^{\pi\gamma}$ is very small because we take into account only large

values of $Q^2 \gg |t_\pi|$. We call this process forward DVCS. But one can also think of the process in a range, where t_π is large. In that case we further on introduce the Mandelstam variable

$$u_\pi = -Q^2 + t + m_\pi^2 - s_\pi - t_\pi \quad (3.40)$$

and keep u_π small. Then we see that $\cos\vartheta_{\pi'}^{\pi\gamma} \rightarrow 1$ becomes large. This shows that the two kinematical regimes can be distinguished very well and we don't run into danger to mix up different kinematics. The latter case is called backward DVCS. We will come to this distinction again in Sec. 3.3.2.

So far we do not know the energies and momenta of the initial and final electron in the pion-photon centre-of-mass frame. Starting from the scalar products $p_e p_\pi$, $p_e p_q$, $p_{e'} p_\pi$ and $p_{e'} p_q$ of Eq. 3.13 one obtains the energy and the angle of the initial- and final-state electrons

$$E_e^{\pi\gamma} = \frac{(p_e \cdot p_q)|\vec{p}_\pi|^{\pi\gamma} + (p_e \cdot p_\pi)|\vec{p}_q|^{\pi\gamma}}{E_q^{\pi\gamma}|\vec{p}_\pi|^{\pi\gamma} + E_\pi^{\pi\gamma}|\vec{p}_q|^{\pi\gamma}}, \quad (3.41)$$

$$\cos\vartheta_e^{\pi\gamma} = \frac{(p_e \cdot p_q)E_\pi^{\pi\gamma} - (p_e \cdot p_\pi)E_q^{\pi\gamma}}{(p_e \cdot p_q)|\vec{p}_\pi|^{\pi\gamma} + (p_e \cdot p_\pi)|\vec{p}_q|^{\pi\gamma}}, \quad (3.42)$$

$$E_{e'}^{\pi\gamma} = \frac{(p_{e'} \cdot p_q)|\vec{p}_\pi|^{\pi\gamma} + (p_{e'} \cdot p_\pi)|\vec{p}_q|^{\pi\gamma}}{E_q^{\pi\gamma}|\vec{p}_\pi|^{\pi\gamma} + E_\pi^{\pi\gamma}|\vec{p}_q|^{\pi\gamma}}, \quad (3.43)$$

$$\cos\vartheta_{e'}^{\pi\gamma} = \frac{(p_{e'} \cdot p_q)E_\pi^{\pi\gamma} - (p_{e'} \cdot p_\pi)E_q^{\pi\gamma}}{(p_{e'} \cdot p_q)|\vec{p}_\pi|^{\pi\gamma} + (p_{e'} \cdot p_\pi)|\vec{p}_q|^{\pi\gamma}}. \quad (3.44)$$

The energies and momenta of the electrons can be treated as equal because their mass is negligible. The angle $\sin\vartheta_{e'}$ is always positive due to the definition of the spherical coordinates, where $\vartheta \in [0.. \pi]$. The explicit calculations of the energies and the momenta of the electrons lead to complex results. Therefore we present a diagram, see Fig. 3.6 a), where the energy is plotted versus the momentum for both of the electrons, showing their different kinematic distribution. The points are obtained from the numerical program calculating the cross section. Each point is a kinematical possible point in the allowed integration region.

Finally we can compute the proton components in the $\pi\gamma$ -frame, using $p_p p_\pi$, $p_p p_q$ and $p_p p_e$ leading to

$$E_p^{\pi\gamma} = \frac{Q^2 + (m_p^2 - m_n^2 + t)x_B}{2x_B s_\pi}, \quad (3.45)$$

$$\cos\vartheta_p^{\pi\gamma} = \frac{-Q^4 + (s_\pi - t)(m_p^2 - m_n^2 + t)x_B - Q^2(s_\pi + t + m_p^2 x_B - m_n^2 x_B + t x_B)}{\sqrt{Q^4 + (s_\pi - t)^2 + 2Q^2(s_\pi + t)}\sqrt{Q^4 + 2Q^2(m_p^2 - m_n^2 + t)x_B + w_2}}, \quad (3.46)$$

including the lower order term $w_2 = (m_p^4 + (m_n^2 - t)^2 - 2m_p^2(m_n^2 + 2s_\pi - t))x_B^2$. As for the electrons we plot the proton energy and momentum shown in Fig. 3.6 b). This shows that the angle of the proton tends to be relatively close to 180°.

3.2 Four particle phase space integral

One main component of the cross section in Eq. 3.1 is the phase space. After introducing the kinematical frame and the kinematics of the pion-photon subframe we can now compute the

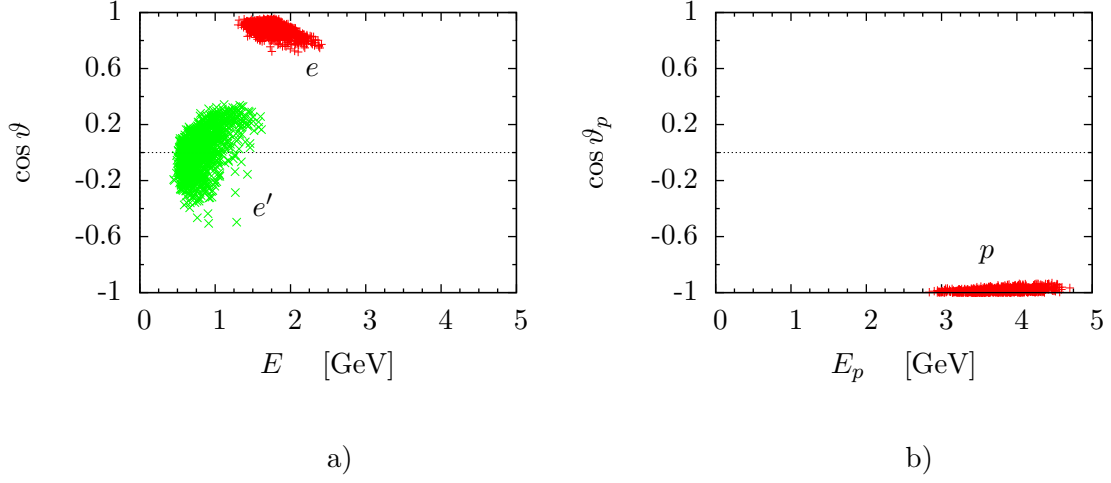


Figure 3.6: a) Distribution of the initial (red) and final (green) electrons in the pion-photon centre-of-mass frame and b) the proton distribution in the pion-photon center-of-mass frame.

required phase space, which is generally defined as

$$\int d\Phi_n = \left(\prod_{f=1}^n \int \frac{d^3 p_f}{(2\pi)^3} \frac{1}{2E_f} \right) (2\pi)^4 \delta^{(4)} \left(p_e + p_p - \sum_{f=1}^n p_f \right), \quad (3.47)$$

where p_f are the momenta of the final-state particles. This contains the integration over the momenta of the n final-state particles having the momenta p_f . The four-dimensional δ -function conserves energy and momentum. $d\Phi_n$ is Lorentz-invariant so that the phase space integral can be computed in any frame of reference.

In particular, the four-particle phase space element of the reaction $e p \rightarrow e' \pi \gamma n$ has the form

$$\int d\Phi_4 = \int \frac{d^3 p_{\pi'} d^3 q_{q'} d^3 p_n d^3 p_{e'}}{(2\pi)^{12}} \frac{(2\pi)^4}{8E_n E_{e'} E_{\pi'} E_{q'}} \delta^{(4)}(p_e + p_p - p_{e'} - p_{\pi'} - p_{q'} - p_n). \quad (3.48)$$

This contains the two-particle phase space of the final pion and photon

$$\int d\Phi_2 = \int \frac{d^3 p_{\pi'} d^3 q_{q'}}{(2\pi)^6} \frac{(2\pi)^4}{4E_{\pi'} E_{q'}} \delta^{(4)}(p_{\pi'} + p_{q'} - p_{\pi} - p_q). \quad (3.49)$$

The two-particle phase space can be calculated in the center-of-mass frame of the pion-photon subsystem, where $\vec{p}_{\pi}^{\pi\gamma} + \vec{p}_{\gamma}^{\pi\gamma} = 0$ and $E_{\pi}^{\pi\gamma} + E_{\gamma}^{\pi\gamma} = \sqrt{s_{\pi\gamma}} = E_{\text{cm}}^{\pi\gamma}$. Inserting this into Eq. 3.49 leads to

$$\begin{aligned} \int d\Phi_2 &= \frac{1}{(2\pi)^2} \int \frac{d^3 p_{\pi'}^{\pi\gamma} d^3 p_{q'}^{\pi\gamma}}{2E_{\pi'}^{\pi\gamma} 2E_{q'}^{\pi\gamma}} \delta^{(4)}(p_q^{\pi\gamma} + p_{\pi}^{\pi\gamma} - p_{q'}^{\pi\gamma} - p_{\pi'}^{\pi\gamma}) \\ &= \frac{1}{16\pi^2} \int \frac{(p_q^{\pi\gamma})^2 dp_q^{\pi\gamma} d\Omega^{\pi\gamma}}{E_q^{\pi\gamma} E_{\pi}^{\pi\gamma}} \delta(E_{\text{cm}}^{\pi\gamma} - E_q^{\pi\gamma} - E_{\pi}^{\pi\gamma}). \end{aligned} \quad (3.50)$$

Integrating over the final δ -function gives

$$\begin{aligned}
\int d\Phi_2 &= \frac{1}{16\pi^2} \int \frac{(\vec{p}_q^{\pi\gamma})^2 d\Omega}{E_q^{\pi\gamma} E_\pi^{\pi\gamma}} \frac{E_q^{\pi\gamma} E_\pi^{\pi\gamma}}{\vec{p}_q^{\pi\gamma} (E_q^{\pi\gamma} + E_\pi^{\pi\gamma})} \\
&= \frac{1}{16\pi^2} \int \frac{|\vec{p}_q^{\pi\gamma}|}{E_q^{\pi\gamma} + E_\pi^{\pi\gamma}} d\cos\vartheta_{\pi'}^{\pi\gamma} d\phi_\pi^{\pi\gamma} \\
&= \frac{1}{16\pi^2} \int \frac{s_\pi - m_\pi^2}{2s_\pi} d\cos\vartheta_{\pi'}^{\pi\gamma} d\phi_\pi^{\pi\gamma}.
\end{aligned} \tag{3.51}$$

Since $\cos\vartheta_{\pi'}^{\pi\gamma}$ is not one of the invariant variables we chose, we substitute it by t_π via

$$\frac{dt_\pi}{d\cos\vartheta_{\pi'}^{\pi\gamma}} = \frac{(s_\pi - m_\pi^2) \sqrt{(s_\pi + t + Q^2)^2 - 4s_\pi t}}{2s_\pi}. \tag{3.52}$$

Including this substitution, the final form of the two-particle phase space reads

$$\int d\Phi_2 = \frac{1}{16\pi^2} \int \frac{1}{\sqrt{(s_\pi + t + Q^2)^2 - 4s_\pi t}} dt_\pi d\phi_\pi. \tag{3.53}$$

To determine $d\Phi_4$ we moreover need the integrations over the final electron and neutron momenta

$$\int \frac{d^3 p_{e'}}{(2\pi)^3 2E_{e'}} \quad \text{and} \quad \int \frac{d^3 p_n}{(2\pi)^3 2E_n}. \tag{3.54}$$

These Lorentz-invariant three-momentum integrals should also be expressed in terms of the invariants, which we use for the final integration to calculate the total cross section. Therefore a variable transformation is made

$$\begin{aligned}
\frac{d^3 p_{e'}}{2E_{e'}} &= \frac{1}{2E_{e'}} (E_{e'})^2 dE' d\cos\vartheta_e d\psi_e \\
&= \frac{1}{2E_{e'}} (E_{e'})^2 dQ^2 dx d\psi_e y (m_p^2 - s) |J_1|^{-1},
\end{aligned} \tag{3.55}$$

$$\begin{aligned}
\frac{d^3 p_n}{2E_n} &= \frac{1}{2E_n} (\vec{p}_n)^2 dE_n d\cos\vartheta_n d\psi_n \\
&= \frac{(\vec{p}_n)^2}{2E_n} |J_2|^{-1} dt dx_\pi d\psi_n.
\end{aligned} \tag{3.56}$$

For the Jacobians J_1 and J_2 we need

$$\begin{aligned}
-Q^2 &= (p_e - p_{e'})^2 \\
&= -2E_e E_{e'} + 2|\vec{p}_e||\vec{p}_{e'}| \cos\vartheta_{e'}
\end{aligned} \tag{3.57}$$

and furthermore an expression for W^2

$$\begin{aligned}
W^2 &= (p_p + p_q)^2 \\
&= m_p^2 - 2E_e E_{e'} + 2|\vec{p}_e||\vec{p}_{e'}| \cos\vartheta_{e'} + (s - m_p^2) - 2E_p E_{e'} + 2|\vec{p}_p||\vec{p}_{e'}| \cos\vartheta_{e'}
\end{aligned} \tag{3.58}$$

to substitute $\cos \vartheta_{e'}$ and $E_{e'}$ by Q^2 and W^2 . We neglect the electron mass and obtain the differentials

$$\frac{dQ^2}{dE_{e'}} = 2E_e(1 - \cos \vartheta_{e'}), \quad \frac{dQ^2}{d \cos \vartheta_{e'}} = -2E_e E_{e'}, \quad (3.59)$$

$$\frac{dW}{dE_{e'}} = \cos \vartheta_{e'} \left(2E_e + 2\sqrt{E_p^2 - m_p^2} \right) - 2\sqrt{s}, \quad \frac{dW}{d \cos \vartheta_{e'}} = 2E_{e'} \left(E_e + \sqrt{E_p^2 - m_p^2} \right), \quad (3.60)$$

which yield the Jacobians

$$J_1 = 4E_e E_{e'} \left(\sqrt{E_p^2 - m_p^2} - E_p \right), \quad (3.61)$$

$$J_2 = \frac{2}{E_p} \sqrt{(E_p^2 - m_p^2)(E_n^2 - m_n^2)}. \quad (3.62)$$

We can easily change from W^2 to x_B via

$$dW^2 = -\frac{Q^2}{x_B^2} dx_B \quad (3.63)$$

This leads to the Lorentz-invariants we use in our calculation

$$\begin{aligned} \frac{d^3 p_{e'}}{2E_{e'}} &= \frac{1}{4} \frac{y}{x_B} dQ^2 dx_B d\psi_{e'} \\ &= \frac{1}{4} dQ^2 dy d\psi_{e'} \end{aligned} \quad (3.64)$$

$$\frac{d^3 p_n}{2E_n} = \sqrt{\frac{E_n^2 - m_n^2}{E_p^2 - m_p^2}} \frac{E_p}{4E_n} dt dx_\pi d\psi_n. \quad (3.65)$$

In the limit of masses and t going to zero we have $d^3 p_n / (2E_n) \rightarrow 1/4$, which corresponds to the results for the (massless) electron. Gathering the results we can now compute the phase space for a two, three and four-particle final-states,

$$\int d\Phi_2(\pi\gamma \rightarrow \pi'\gamma') = \frac{1}{16\pi^2} \int \frac{1}{\sqrt{(s_\pi + t + Q^2)^2 - 4s_\pi t}} dt_\pi d\phi_\pi, \quad (3.66)$$

$$\begin{aligned} \int d\Phi_3(e\pi \rightarrow e'\pi'\gamma) &= \int \phi_2 \frac{d^3 p_{e'}}{2E_{e'}(2\pi)^3} \\ &= \int \frac{1}{16(2\pi)^5} \frac{1}{\sqrt{(s_\pi + t + Q^2)^2 - 4s_\pi t}} dt_\pi d\phi_\pi dQ^2 dy d\psi_e, \end{aligned} \quad (3.67)$$

$$\begin{aligned} \int d\Phi_4(ep \rightarrow e'n\pi\gamma) &= \int \phi_3 \frac{d^3 p_n}{(2\pi)^3 2E_n} \\ &= \int \phi_3 \sqrt{\frac{E_n^2 - m_n^2}{E_p^2 - m_p^2}} \frac{E_p}{4E_n} \frac{1}{(2\pi)^3} dx_\pi dt d\psi_n. \end{aligned} \quad (3.68)$$

We can express Φ_4 also in terms of invariants, but this expression is omitted here, since it is a lengthy expression leading to no further information.

An additional term appearing in the differential cross section is the flux factor which is defined by

$$\begin{aligned} F_{ep}(s, m_p^2) &= 4\sqrt{(p_e \cdot p_p)^2 - m_e^2 m_p^2} \\ &= 2(s - m_p^2), \end{aligned} \quad (3.69)$$

where we again neglected the electron mass.

3.3 The $e\pi \rightarrow e'\pi'\gamma$ subprocess

3.3.1 Kinematics for the electron-pion subprocess

When we deal with the process $e\pi \rightarrow e'\pi'\gamma$ we shall work in the center-of-mass frame of the electron and the virtual pion. This process is analogue to DVCS off a proton $ep \rightarrow e'p\gamma$ and can be treated in the same way. To deal with the electron-pion scattering process it is convenient to introduce variables corresponding to the scattering off a proton target, these are

$$x_B^\pi = \frac{Q^2}{2p_\pi \cdot p_q}, \quad (3.70)$$

$$t_\pi = (p_{\pi'} - p_\pi)^2, \quad (3.71)$$

$$\begin{aligned} \xi_\pi &= \frac{p_\pi^+ - p_{\pi'}^+}{p_\pi^+ + p_{\pi'}^+} \\ &\approx \frac{x_B^\pi}{2 - x_B^\pi}. \end{aligned} \quad (3.72)$$

Similar to t we have t_π which is the momentum transfer between the pions. Analogue to x_B and ξ in the proton case, x_B^π is the fraction of the longitudinal momentum of the quark in the pion and ξ_π the longitudinal momentum transfer between the initial and final state pion. We can expand x_B^π by neglecting masses and momentum transfer. This leads to

$$x_B^\pi = \frac{x_B}{x_\pi} + \mathcal{O}\left(\frac{m^2}{Q^2}\right). \quad (3.73)$$

Moreover we introduce further variables which are relevant for the calculations

$$\begin{aligned} s_{e\pi} &= (p_e + p_\pi)^2 \\ &\approx s \cdot x_\pi, \end{aligned} \quad (3.74)$$

$$\begin{aligned} y_\pi &= \frac{p_q \cdot p_\pi}{p_e \cdot p_\pi} \\ &\approx y. \end{aligned} \quad (3.75)$$

The variable x_π introduced in Eq. 3.13 can be approximated by

$$\begin{aligned} x_\pi &= \frac{p_e \cdot p_\pi}{p_e \cdot p_p} \\ &= 1 - \frac{p_e \cdot p_n}{p_e \cdot p_p} \\ &\approx \frac{E_\pi}{E_p}, \end{aligned} \quad (3.76)$$

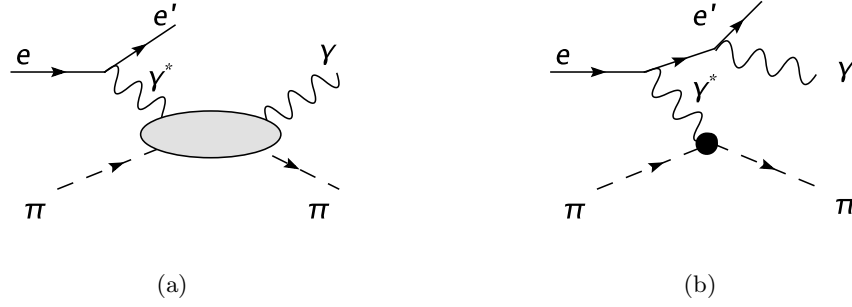


Figure 3.7: a) Deeply virtual Compton scattering off a virtual pion and b) the corresponding Bethe–Heitler process

this confirms the statement we made in the introduction, that x_π gives the ratio of the pion and proton energy. The last formula is valid in any frame where the proton is moving fast.

In the calculation of the cross section, we further use ϵ_π , the ratio of the longitudinal and transverse polarization of the virtual photon,

$$\epsilon_\pi = \frac{1 - y_\pi}{1 - y_\pi + y_\pi^2/2}. \quad (3.77)$$

Having these variables we can also define the flux factor for the electron-pion scattering process

$$\begin{aligned} F_{e\pi} &= 4\sqrt{(p_e \cdot p_\pi)^2} \\ &= 2(s_{e\pi} - m_\pi^2) \\ &= 2x_\pi(s - m_p^2) + \mathcal{O}(m^2). \end{aligned} \quad (3.78)$$

3.3.2 Squared amplitude of $e\pi \rightarrow e'\pi'\gamma$

Since we have two processes, DVCS and Bethe–Heitler, both contributing to the cross section, they will interfere at amplitude level. The complete amplitude reads

$$|\mathcal{T}_{e\pi}|^2 = |\mathcal{T}_{\text{DVCS}}|^2 + |\mathcal{T}_{\text{BH}}|^2 + \mathcal{T}_{\text{INT}}. \quad (3.79)$$

For the calculation of the scattering amplitude we treat the virtual pion as an on-shell pion. One way to determine the amplitude for virtual scattering off the pion is to derive it from proton DVCS. Doing that, form factors and GPDs of the proton have to be replaced by those of the pion. We are now going to deduce the amplitude from the well-known proton amplitude. It is worth presenting also the proton amplitude, since we will use this in calculations in Chapter 4. This leads to the same results as calculating the process from scratch as done by Belitsky *et al.*[93]. We compare our results to those of Belitsky *et al.* and see that they coincide, except in the overall sign in the Bethe–Heitler amplitude squared. But since the amplitude has to be positive, we stick to our result.

It is common to parameterize the scattering amplitudes $\mathcal{T}_{\text{DVCS}}$, \mathcal{T}_{BH} and \mathcal{T}_{INT} in terms of helicity amplitudes $M_{\lambda'\mu',\lambda\mu}$, where $\lambda(\lambda')$ is the proton helicity and $\mu(\mu')$ the photon helicity.

All in all there are 24 amplitudes which reduce to twelve by applying parity invariance:

$$M_{\lambda'+,\lambda+} \quad \text{leading order in } \frac{1}{Q} \text{ and } \alpha_s, \quad (3.80)$$

$$M_{\lambda'+,\lambda 0} \quad \frac{1}{Q} \text{ suppressed}, \quad (3.81)$$

$$M_{\lambda'+,\lambda-} \quad \text{suppressed by either } \alpha_s \text{ or } \frac{1}{Q^2}. \quad (3.82)$$

The four leading order amplitudes in $1/Q$ can be expressed via the GPDs H , \tilde{H} , E and \tilde{E} .

As we can read from the definition of the pion GPD in Eq. 2.7 there is only one GPD parameterizing the vector matrix element, while the axial vector case does not exist for a pion. Due to the fact that the pion is a spin-zero particle there appear no spinors and comparing the pion GPD and the nucleon GPDs we can make the replacement

$$\bar{u}(p')H^q(x, \xi, t)\gamma^+u(p) + \bar{u}(p')E^q(x, \xi, t)\frac{i\sigma^{+\nu}\Delta_\nu}{2m}u(p) \rightarrow H_\pi^q, \quad (3.83)$$

$$\tilde{F}^q \rightarrow 0. \quad (3.84)$$

The number of GPDs is obtained by counting helicity amplitudes under the constraints due to spatial parity only. For spin-zero targets there is only

$$\langle p_2 | \mathcal{O}(-z^-, z^-) | p_1 \rangle = p^+ \int_{-1}^1 dx e^{-ixp^+z^-} H^q(x, \eta, t). \quad (3.85)$$

Since the pion is a spin-zero particle it cannot flip helicity and therefore there is no replacement for the GPD E^q of the proton. Thus it follows that

$$H_p^q \rightarrow H_\pi^q, \quad (3.86)$$

$$E_p^q \rightarrow 0. \quad (3.87)$$

3.3.2.1 DVCS amplitude

Now we would like to consider the proton DVCS amplitude in some detail. The amplitude for such a process can be written as a convolution of a perturbatively calculable contribution describing the hard scattering the and non-perturbative part containing GPDs, as mentioned in Sec. 1.1.3.1. We consider the kinematical region where the momentum transfer between the initial- and final-state proton is small compared to Q^2 . The final result for the proton DVCS amplitude for helicity conserving, transverse photons is given by

$$\sum'_{\text{spins}} |\mathcal{T}_{\text{DVCS}}|^2 = \frac{1}{Q^2} \frac{2}{1-\epsilon} \sum_{\lambda, \lambda'} \frac{1}{2} |M_{\lambda'+,\lambda+}|^2 \quad (3.88)$$

with λ, λ' being the proton helicities [79]. \sum'_{spins} denotes the sum over the final-state proton and photon spins and the average over the initial proton. The prefactor $2/(Q^2(1-\epsilon))$ is related to the transversely polarized photons. The squared amplitude contains the nucleon GPDs which are themselves contained in the Compton form factors \mathcal{H} , $\tilde{\mathcal{H}}$, \mathcal{E} and $\tilde{\mathcal{E}}$

$$\begin{aligned} \sum_{\lambda, \lambda'} \frac{1}{2} |M_{\lambda'+,\lambda+}|^2 &= (1-\xi^2)(|\mathcal{H}|^2 + |\tilde{\mathcal{H}}|^2) - \left(\xi^2 + \frac{t}{4m^2}\right)|\mathcal{E}|^2 - \xi^2 \frac{t}{4m^2} |\tilde{\mathcal{E}}|^2 \\ &\quad - 2\xi^2 \text{Re}(\mathcal{H}^*\mathcal{E} + \tilde{\mathcal{H}}^*\tilde{\mathcal{E}}). \end{aligned} \quad (3.89)$$

The Compton form factors are defined as

$$\mathcal{F}(\rho, \xi, t) = \sum_q e_q^2 \int_{-1}^1 dx F^q(x, \xi, t) \left(\frac{1}{\rho - x - i\epsilon} - \frac{1}{\rho + x - i\epsilon} \right) + \mathcal{O}(\alpha_s), \quad (3.90)$$

$$\tilde{\mathcal{F}}(\rho, \xi, t) = \sum_q e_q^2 \int_{-1}^1 dx \tilde{F}^q(x, \xi, t) \left(\frac{1}{\rho - x - i\epsilon} + \frac{1}{\rho + x - i\epsilon} \right) + \mathcal{O}(\alpha_s). \quad (3.91)$$

According to the definitions in [94, 95] the Compton form factors \mathcal{H} and \mathcal{E} are obtained by replacing F^q in Eq. 3.90 with H^q and E^q and analogue for $\tilde{\mathcal{H}}$ and $\tilde{\mathcal{E}}$ by replacing \tilde{F}^q in Eq. 3.91 with \tilde{H}^q and \tilde{E}^q .

The structure for the amplitude changes when we replace the proton with the pion. In the proton case the helicity amplitude contains all four Compton form factors while for the pion we have only \mathcal{H}_π . The factor $(1 - \xi^2)$ in front of \mathcal{H}^2 appears due to the spinors which are not present for pions anymore, so the cross section has to be divided by $(1 - \xi^2)$. The final form for the pion is

$$\sum'_{\text{spins}} |\mathcal{T}_{\text{DVCS}}|^2 = \frac{1}{Q^2} \frac{2}{1 - \epsilon_\pi} |\mathcal{H}_\pi^q(x, \xi_\pi, t_\pi)|^2, \quad (3.92)$$

where \mathcal{H}_π is the Compton form factor for the pion. In Sec. 3.6.1 in Fig. 3.10 we show the real and imaginary part of the x -integrated pion Compton form factor for four different models and for three different values of $\xi_\pi = 0.2, 0.3, 0.4$. These models will be explained in Sec. 3.9.1 and 3.9.2. Those plots show the the model dependence of the expected t_π behavior for fixed values of ξ_π integrated over x .

3.3.2.2 Backward scattering and transition distribution amplitudes

Extensions of these studies in the backward regime — where t_π is large — involving a transition from a photon to a meson [96] or from a baryon to a meson or a photon [97] were recently proposed. In our case we need a transition from a pion to a photon which is depicted in Fig. 3.8 b). In the latter regime, the nonperturbative objects playing the role of the GPDs are named Transition Distribution Amplitudes (TDAs). First phenomenological studies can be found in [98, 99]. In the backward region u_π has to be small. Compared to the kinematical regime of DVCS discussed above, the role of t_π and u_π changes. In the backward regime the Bethe–Heitler process is expected to be suppressed.

We show here the definition of the TDA for the transition $\gamma \rightarrow \pi^-$ as given in [100]

$$\begin{aligned} \frac{dz^-}{2\pi} e^{ixP^+z^-} \left\langle \pi^-(p_{\pi^-}) \left| \bar{d} \left(-\frac{z}{2} \right) \left[-\frac{z}{2}; \frac{z}{2} \right] \gamma^\mu u \left(\frac{z}{2} \right) \right| \gamma(p_\gamma, \varepsilon) \right\rangle \Big|_{z^+ = z_T = 0} \\ = \frac{1}{P^+} \frac{ie}{f_\pi} e^{\mu\varepsilon P \Delta_\perp} V^{\pi^-}(x, \xi, t), \end{aligned} \quad (3.93)$$

$$\begin{aligned} \frac{dz^-}{2\pi} e^{ixP^+z^-} \left\langle \pi^-(p_{\pi^-}) \left| \bar{d} \left(-\frac{z}{2} \right) \left[-\frac{z}{2}; \frac{z}{2} \right] \gamma^\mu \gamma^5 u \left(\frac{z}{2} \right) \right| \gamma(p_\gamma, \varepsilon) \right\rangle \Big|_{z^+ = z_T = 0} \\ = \frac{1}{P^+} \frac{e}{f_\pi} (\varepsilon \cdot \Delta) P^\mu A^{\pi^-}(x, \xi, t), \end{aligned} \quad (3.94)$$

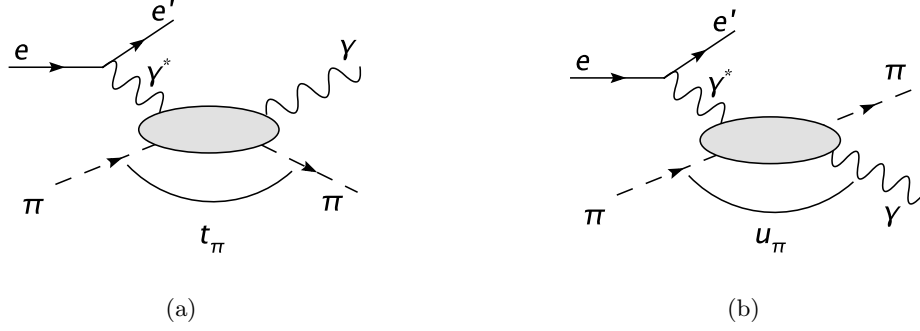


Figure 3.8: a) Deeply virtual Compton scattering off a virtual pion parametrized by GPDs in the kinematical regime of small t_π . b) The kinematical regime of small u_π which corresponds to backward scattering, parametrized by TDAs.

$$\begin{aligned} \frac{dz^-}{2\pi} e^{ixP^+z^-} \left\langle \pi^-(p_{\pi^-}) \left| \bar{d} \left(-\frac{z}{2} \right) \left[-\frac{z}{2}; \frac{z}{2} \right] \sigma_{\mu\nu} u \left(\frac{z}{2} \right) \right| \gamma(p_\gamma, \varepsilon) \right\rangle \Big|_{z^+=z_T=0} \\ = \frac{e}{P^+} \epsilon^{\mu\varepsilon P\Delta_\perp} P_\sigma \left[\varepsilon_\rho T_1^{\pi^-}(x, \xi, t) - \frac{1}{f_\pi} (\varepsilon \cdot \Delta) \Delta_{\perp\rho} T_2^{\pi^-}(x, \xi, t) \right], \end{aligned} \quad (3.95)$$

where $P = (p_{\pi^-} + p_\gamma)/2$ and $\Delta = p_{\pi^-} - p_\gamma$. V^{π^-} is the vector and A^{π^-} the axial vector TDA, and $T_{1,2}^{\pi^-}$ are the chiral-odd tensorial TDAs. Due to the photon polarization ε there are four TDAs in the leading twist decomposition. TDAs can be related to vector and axial vector form factors and can be modeled by double distributions. For further details see [101]. In Sec. 3.8 we will show some plots depicting the two different regimes of forward and backward Compton scattering.

3.3.2.3 Bethe–Heitler amplitude

In addition to DVCS we have to consider the Bethe–Heitler amplitude. The form factors for the nucleon are defined in the following way

$$\langle p_{p'} | j_{em}^\mu | p_p \rangle = \bar{u}(p_{p'}) \left(F_1 \gamma^\mu + F_2 \frac{\sigma^{\mu\nu} \Delta_\nu}{2m_p} \right) u(p_p). \quad (3.96)$$

The amplitude of the Bethe–Heitler process has the form

$$\sum'_{\text{spins}} |\mathcal{T}_{\text{BH}}|^2 = -\frac{4}{t\epsilon P} \left[\frac{1-\xi^2}{\xi} \frac{t-t_0}{t} \left(F_1^2(t) - \frac{t}{4m_p^2} F_2^2(t) \right) + 2(F_1(t) + F_2(t))^2 + \mathcal{O}\left(\frac{1}{Q}\right) \right]. \quad (3.97)$$

Since form factors are measured experimentally very well, the Bethe–Heitler process can be treated accurately in a numerical analysis [102, 103]. For $y \rightarrow 1$ the BH contribution could blow up since the factor $1/\epsilon$, containing y , goes to zero in that limit. However at HERMES and CLAS y is restricted to $y < 0.85$. We have included the factor $P = 1 + (\cos \phi) \mathcal{O}(1/Q)$, which is the ratio of exact and approximated lepton propagators. The lepton virtualities are independent of ϕ_π to leading order in $1/Q$. But experimentally this ϕ_π dependence cannot

be neglected, therefore we keep the term P . For our numerical calculations we use for P :

$$P = \frac{(A_s - B \cos \phi_\pi)(A_u - B \cos \phi_\pi)}{A_s A_u}, \quad (3.98)$$

with

$$A_s = \frac{Q^2(1 - y_\pi)t_\pi}{y_\pi}, \quad (3.99)$$

$$A_u = \frac{Q^2(1 - y_\pi) - t_\pi}{y_\pi}, \quad (3.100)$$

$$B = \frac{2Q^2}{y_\pi} \sqrt{1 - y_\pi - \frac{1}{4}y_\pi^2 \gamma_\pi^2} \sqrt{(1 - x_B^\pi)(t_{\pi,0} - t_\pi)}, \quad (3.101)$$

$$\gamma_\pi = \frac{2x_B^\pi m_p}{Q}, \quad (3.102)$$

up to relative corrections of order $x_B^\pi t/Q^2$ or $x_B^\pi t_\pi/Q^2$. For more details on P see [79]. An exact expressions for the amplitude is given in [95].

In the pion case one has as a first parametrisation, with $\Delta_\pi^\mu = (p_{\pi'} - p_\pi)^\mu$ and $P_\pi^\mu = \frac{1}{2}(p_\pi + p_{\pi'})^\mu$

$$\langle p_{\pi'} | j_{em}^\mu | p_\pi \rangle = a_1 \Delta_\pi^\mu + a_2 P_\pi^\mu. \quad (3.103)$$

Applying time-reversal invariance one obtains

$$\langle p_{\pi'} | j_{em}^\mu | p_\pi \rangle = -a_1 \Delta_\pi^\mu + a_2 P_\pi^\mu. \quad (3.104)$$

Parity does not lead to a change. But because both relations have to be valid (before and after time invariance) a_1 has to vanish. This leads to the final form of the pion form factor

$$\langle p_{\pi'} | j_{em}^\mu | p_\pi \rangle = (p_{\pi'} + p_\pi)^\mu F_\pi(Q^2). \quad (3.105)$$

For the pion we obtain an expression analogous to the proton for the Bethe–Heitler amplitude

$$\sum'_{\text{spins}} |\mathcal{T}_{\text{BH}}|^2 = -\frac{4(1 - \xi_\pi^2)(t_\pi - t_{\pi 0})}{t_\pi^2 \epsilon_\pi \xi_\pi^2 P} F_\pi^2 + \mathcal{O}\left(\frac{1}{Q}\right). \quad (3.106)$$

3.3.2.4 Interference term

The interference term appearing in the squared amplitude is given by

$$\mathcal{T}_{\text{INT}} = \mathcal{T}_{\text{BH}}^* \mathcal{T}_{\text{DVCS}} + \mathcal{T}_{\text{DVCS}}^* \mathcal{T}_{\text{BH}}. \quad (3.107)$$

Considering only virtual and real photons with the same helicity the result of the cross section for proton scattering is

$$\begin{aligned} \sum'_{\text{spins}} \mathcal{T}_{\text{INT}} &= e_l \frac{8\sqrt{2}m}{tQ\xi P} \cos \phi_\pi \frac{1}{\sqrt{\epsilon(1-\epsilon)}} \text{Re} \hat{M}_{++} \\ &\quad + e_l \frac{8\sqrt{2}m}{tQ\xi P} P_l \sin \phi_\pi \sqrt{\frac{1+\epsilon}{\epsilon}} \text{Im} \hat{M}_{++}. \end{aligned} \quad (3.108)$$

This term includes e_l which is the lepton beam charge and P_l the lepton beam polarization. For our calculation we are going to take into account only electrons (no positrons) and have therefore $e_l = -1$. \hat{M}_{++} is known [104] and has the form

$$\hat{M}_{++} = \sqrt{1 - \xi^2} \frac{\sqrt{(t_0 - t)}}{2m} \left(F_1(t) \mathcal{H} + \xi (F_1(t) + F_2(t)) \tilde{\mathcal{H}} - \frac{t}{4m^2} F_2(t) \mathcal{E} \right) \quad (3.109)$$

including GPDs as well as form factors. The amplitude reduces in the pion case to

$$\begin{aligned} \sum'_{\text{spins}} |\mathcal{T}_{\text{INT}}| &= e_l \frac{4\sqrt{2}}{t_\pi Q \xi_\pi P} \left(\cos\phi_\pi \frac{1}{\sqrt{\epsilon_\pi(1 - \epsilon_\pi)}} \sqrt{(1 - \xi_\pi^2)(t_{\pi 0} - t_\pi)} F_\pi(t_\pi) \text{Re}(\mathcal{H}_\pi) \right. \\ &\quad \left. + P_l \sin\phi_\pi \sqrt{\frac{1 + \epsilon_\pi}{\epsilon_\pi}} \sqrt{(1 - \xi_\pi^2)(t_{\pi 0} - t_\pi)} F_\pi(t_\pi) \text{Im}(\mathcal{H}_\pi) \right). \end{aligned} \quad (3.110)$$

This interference term consists in leading order in Q of two terms which we refer to as

$$\sum'_{\text{spins}} |\mathcal{T}_{\text{BCA}}| = e_l \frac{4\sqrt{2}}{t_\pi Q \xi_\pi} \cos\phi_\pi \frac{1}{\sqrt{\epsilon_\pi(1 - \epsilon_\pi)}} \sqrt{(1 - \xi_\pi^2)(t_{\pi 0} - t_\pi)} F_\pi(t_\pi) \text{Re}(\mathcal{H}_\pi), \quad (3.111)$$

$$\sum'_{\text{spins}} |\mathcal{T}_{\text{BPA}}| = e_l \frac{4\sqrt{2}}{t_\pi Q \xi_\pi} P_l \sin\phi_\pi \sqrt{\frac{1 + \epsilon_\pi}{\epsilon_\pi}} \sqrt{(1 - \xi_\pi^2)(t_{\pi 0} - t_\pi)} F_\pi(t_\pi) \text{Im}(\mathcal{H}_\pi), \quad (3.112)$$

where \mathcal{T}_{BCA} is proportional to the beam charge asymmetry and \mathcal{T}_{BPA} to the beam polarization asymmetry. Because it is much simpler to measure asymmetries compared to cross sections we will focus our attention on these asymmetries in Sec. 3.7

3.4 Hadronic part of $e p \rightarrow e' \pi \gamma n$

We separate the process into different parts as depicted in Fig. 3.1. In addition to the $e\pi$ amplitude we furthermore need the hadronic part (lower part in the figure). Hence we will now take into account the transition between the proton and the neutron by the emission of a pion. This hadronic part is calculated by the sum over the proton spin

$$\begin{aligned} \sum'_{\text{spins}} |\bar{u}(p_{p'}) \gamma_5 u(p_p)|^2 &= \sum'_{\text{spins}} (\bar{u}(p_{p'}) \gamma_5 u(p_p)) (\bar{u}(p_{p'}) \gamma_5 u(p_p))^* \\ &= -\frac{1}{2} \text{Tr}((\not{p}_{p'} + m_p) \gamma_5 (\not{p}_p + m_p) \gamma_5) \\ &= -\frac{1}{2} (4m_p^2 - 4p_p \cdot p_{p'}) \\ &= -t. \end{aligned} \quad (3.113)$$

The vertex of the pion-nucleon-nucleon coupling is described by the dimensionless coupling $g_{\pi NN} = 14.7$ which is given by the Goldberger Treiman relation.

Eventually the hadronic part and the scattering off the pion are connected by the propagating pion. Therefore we have to implement the pion propagator

$$\frac{1}{m_\pi^2 - t} \quad (3.114)$$

into the cross section.

3.5 Differential cross section for the process $ep \rightarrow e' \pi \gamma n$

In the last sections we have derived all components which are necessary to compute the cross section. Analytically we can express the eight-fold differential cross section

$$\frac{d\sigma(ep \rightarrow e\pi\gamma n)}{dQ^2 dy dx_\pi dt_\pi dt d\phi_\pi d\psi_{e'} d\psi_n} = \Phi_4 F_{ep} \sum_{\text{spins}} |\mathcal{T}_{e\pi}|^2 \frac{-t}{(m_\pi^2 - t)^2} g_{\pi NN}^2 \left(\frac{\Lambda^2 - m_\pi^2}{\Lambda^2 - t} \right)^2. \quad (3.115)$$

\sum_{spins} sums over the final-state electron and photon polarization. Furthermore we have averaged over the proton polarization and summed over the neutron polarization and kept the lepton polarization fixed. We have included a phenomenological factor $(\Lambda^2 - m_\pi^2)/(\Lambda^2 - t)$ that cuts the $1/(m_\pi^2 - t)$ behavior of the pure pole term for large $-t$. As a cut-off mass we take a value of $\Lambda = 0.8 \text{ GeV}$ as suggested in [105]. With the flux factor of Eq. 3.69, the phase space from Eq. 3.68 and the amplitudes for DVCS, BH and the interference term (Eqs. 3.92, 3.106 and 3.110) we can completely determine this differential cross section,

$$\begin{aligned} \frac{d\sigma(ep \rightarrow e\pi\gamma n)}{dQ^2 dy dx_\pi dt_\pi dt d\phi_\pi d\psi_{e'} d\psi_n} &= \left(\frac{1}{4} + a_1 \right) \frac{x_\pi}{(2\pi)^3} \frac{d\sigma(e\pi \rightarrow e\pi'\gamma)}{dQ^2 dy_\pi dt_\pi d\phi_\pi \psi_e} \frac{-t}{(m_\pi^2 - t)^2} \\ &\times g_{\pi NN}^2 \left(\frac{\Lambda^2 - m_\pi^2}{\Lambda^2 - t} \right)^2, \end{aligned} \quad (3.116)$$

where we have used the abbreviation $a_1 = (x_B(-m_n^2 + m_p^2(1 - x_\pi)^2)y)/(2Q^2(1 - x_\pi))$. It can be seen in the last equation that the differential cross section for the four-particle final state contains the differential cross section of the scattering process $e\pi \rightarrow e\pi'\gamma$, which is given by

$$\frac{d\sigma(e\pi \rightarrow e\pi'\gamma)}{dQ^2 dy_\pi dt_\pi d\phi_\pi d\psi_{e'}} = F_3 \Phi_3 \sum_{\text{spins}} |\mathcal{T}_{e\pi}|^2. \quad (3.117)$$

Finally we know the differential cross section for $ep \rightarrow e' \pi \gamma n$. To obtain the total cross section, we numerically integrate over the eight invariant variables. This is done using the Vegas routine. Therefore we need to insert a model for the pion GPD to perform the integration and in addition we need to determine the integration limits and have to take into account experimental constraints on the kinematics and the dimensions of the detector.

3.6 Models for the pion GPD

Let us now focus on the required pion GPD. We use for our calculation of the cross section a model for the pion GPD, where we have a factorized t_π -dependence,

$$H_\pi^q(x, \xi_\pi, t_\pi) = H_\pi^q(x, \xi_\pi) F(t_\pi). \quad (3.118)$$

This is a simple approach but adequate for our purpose, because the pion GPD is still unknown. On the level of the cross section the pion GPD is contained in the Compton form factor, which is generally defined in Eq. 3.90, and reads for the pion

$$\mathcal{H}_\pi(x, \xi_\pi, t_\pi) = \sum_q e_q^2 \int_{-1}^1 dx H_\pi^q(x, \xi_\pi) F(t_\pi) \left(\frac{1}{\xi_\pi - x - i\epsilon} - \frac{1}{\xi_\pi + x - i\epsilon} \right) + \mathcal{O}(\alpha_s). \quad (3.119)$$

For the t_π -independent function in Eq. 3.119 we use the double distribution ansatz shown in Sec. 2.4 which contains the pionic parton distributions. We neglect any evolution effects since we stay in a narrow range of Q^2 . We can rewrite the Compton form factor in terms of the integrals given in [106],

$$I^q(\xi_\pi) = \int_{-1}^1 dx H^q(x, \xi_\pi) \frac{1}{\xi_\pi - x - i\epsilon}, \quad (3.120)$$

$$I^{\bar{q}}(\xi_\pi) = \int_{-1}^1 dx H^{\bar{q}}(x, \xi_\pi) \frac{1}{\xi_\pi - x - i\epsilon} = [I^q(-\xi_\pi)]^*, \quad (3.121)$$

here we use the definitions $H^{\bar{q}}(x, \xi_\pi) = -H^q(-x, \xi_\pi)$ and $\tilde{H}^{\bar{q}}(x, \xi_\pi) = \tilde{H}^q(-x, \xi_\pi)$. We obtain

$$\mathcal{H}_\pi = F_\pi(t) \left(\frac{4}{9} \int_{-1}^1 dx (I^u + I^{\bar{u}}) + \frac{1}{9} \int_{-1}^1 dx (I^d + I^{\bar{d}}) \right). \quad (3.122)$$

These integrals can be divided into an imaginary and a real part

$$\text{Im} I^q(\xi_\pi) = \int_0^{\frac{2\xi_\pi}{1+\xi_\pi}} dx I(x, \xi_\pi) q(x), \quad (3.123)$$

$$\text{Im} I^{\bar{q}}(\xi_\pi) = \int_0^{\frac{2\xi_\pi}{1+\xi_\pi}} dx I(x, \xi_\pi) \bar{q}(x), \quad (3.124)$$

$$\text{Re} I^q(\xi_\pi) = \int_0^1 dx (R(x, \xi_\pi) q(x) + R(x, -\xi_\pi) \bar{q}(x)), \quad (3.125)$$

where $q(x)$ and $\bar{q}(x)$ are the quark distribution functions and the functions $I(x, \xi_\pi)$ and $R(x, \xi_\pi)$ are given by

$$R(x, \xi_\pi, b=1) = \frac{3}{4\xi_\pi^3(1-x)^3} \left(2\xi_\pi(1-x)(x-\xi_\pi) + x(1-\xi_\pi) \left[x(1+x) - 2\xi_\pi \right] \log \frac{|x(1+x) - 2\xi_\pi|}{x(1-\xi_\pi)} \right), \quad (3.126)$$

$$R(x, \xi_\pi, b=2) = \frac{5}{16\xi_\pi^5(1-x)^5} \left(2\xi_\pi(1-x)(x-\xi_\pi) [3(x-\xi_\pi^2 - 5\xi_\pi^2(1-x)^2)] + 3x^2(1-\xi_\pi)^2 \left[x(1+x) - 2\xi_\pi \right]^2 \log \frac{|x(1+x) - 2\xi_\pi|}{x(1-\xi_\pi)} \right), \quad (3.127)$$

$$I(x, \xi_\pi) = \frac{\pi\Gamma(2b+2)}{2^{2b+1}\Gamma^2(b+1)} \frac{(1-\xi_\pi)^b}{\xi_\pi^{2b+1}} \frac{1}{(1-x)^{2b+1}} \left(\frac{2\xi_\pi}{1+\xi_\pi} - x \right)^b x^b. \quad (3.128)$$

The function $R(x, \xi_\pi)$ is continuous in the full integration interval and has finite limits at $x=0$ and $x=1$. $I(x, \xi_\pi)$ vanishes at the endpoints of the integration region ensuring convergence. It is a better ansatz to take $b=2$, because the $b=1$ strongly depends on the PDF for $x \rightarrow 0$, which is unknown. Now we want to determine the imaginary and real part of the Compton form factor of Eq. 3.122. For the positive charged pion, consisting of a u and a \bar{d} quark, the valence and sea distributions v^π and \bar{q}^π are given by

$$v^\pi = u_v^\pi + \bar{d}_v^\pi = 2(u^\pi - \bar{u}^\pi), \quad (3.129)$$

$$\bar{q}^\pi = \bar{u}^\pi = d^\pi. \quad (3.130)$$

Inserting these distributions into Eq. 3.122 we get the imaginary part

$$\begin{aligned}\text{Im}\mathcal{H}_\pi(x, \xi_\pi, t_\pi) &= F_\pi(t_\pi) \int_{-1}^1 dx I(x, \xi_\pi) \left(\frac{4}{9}(u^\pi + \bar{u}^\pi) + \frac{1}{9}(d^\pi + \bar{d}^\pi) \right) \\ &= F_\pi(t_\pi) \int_{-1}^1 dx I(x, \xi_\pi) \left(\frac{5}{9} \left(\frac{1}{2}v^\pi + 2\bar{q}^\pi \right) \right)\end{aligned}\quad (3.131)$$

and for the real part

$$\text{Re}\mathcal{H}_\pi(x, \xi_\pi, t_\pi) = \int_{-1}^1 dx \left(R(x, \xi_\pi) \left(\frac{4}{9}u^\pi + \frac{1}{9}d^\pi \right) + R(x, -\xi_\pi) \left(\frac{4}{9}\bar{u}^\pi + \frac{1}{9}\bar{d}^\pi \right) \right) \quad (3.132)$$

of the Compton form factor. Now we have to include the pion quark distribution functions into the Compton form factor. The valence density of the pion is experimentally well measured in Drell-Yan dilepton production, whereas the sea-quark density is unconstrained so far.

3.6.1 Pion PDFs

First we consider a parametrization given by Glück, Reya and Schienbein (GRS) [107]. Neglecting the strange quark content in the low resolution scale $\mu_{\text{LO}}^2 = 0.26 \text{ GeV}^2$ the constituent quark independent relation given in [107] by GRS is

$$\frac{v^\pi(n, \mu^2)}{v^p(n, \mu^2)} = \frac{\bar{q}^\pi(n, \mu^2)}{\bar{q}^p(n, \mu^2)} = \frac{g^\pi(n, \mu^2)}{g^p(n, \mu^2)}, \quad (3.133)$$

where v , \bar{q} and g are the parton contents of the proton and pion with $v^p = u_v^p + d_v^p$, $\bar{q}^p = (\bar{u}^p + \bar{d}^p)/2$ for the proton and $v^\pi = u_v^{\pi^+} + d_v^{\pi^+}$, $\bar{q}^\pi = (\bar{u}^{\pi^+} + \bar{d}^{\pi^+})/2$ and $d_v^{\pi^+} = \bar{u}_v^{\pi^+}$ for the positive charged pion. Besides Glück, Reya and Schienbein have taken the Mellin n -moments

$$v(n, Q^2) \equiv \int_0^1 x^{n-1} v(x, Q^2) dx, \quad (3.134)$$

and similarly for \bar{q} and g . The better v^π is measured, the better the sea density for the pion can be estimated. With the definition of s

$$s \equiv \ln \left[\frac{\ln[Q^2/(0.204\text{GeV})^2]}{\ln[\mu_{\text{LO}}^2/(0.204\text{GeV})^2]} \right], \quad (3.135)$$

the parametrization of the valence distribution in the kinematical range of $0.5 \text{ GeV}^2 \leq Q^2 \leq 10^5 \text{ GeV}^2$ and $10^{-5} \leq x < 1$ is given by

$$xv^\pi(x, \mu^2) = N x^a (1 + A\sqrt{x} + Bx)(1-x)^D. \quad (3.136)$$

and the light sea-quark distribution is parametrized as

$$\begin{aligned}x\bar{q}^\pi(x, \mu^2) &= \left[x^a (A + B\sqrt{x} + Cx) \left(\ln \frac{1}{x} \right)^b \right. \\ &\quad \left. + s^\alpha \exp \left(-E + \sqrt{E' s^\beta \ln \frac{1}{x}} \right) \right] (1-x)^D\end{aligned}\quad (3.137)$$

The parameters are given in the Appendix C, Eqs. C.1 and C.2. We choose an input scale of $Q = 2 \text{ GeV}$. Any next-to-leading order corrections are neglected in this work. To avoid the simple t_π -factorized ansatz one can think of a model with a t_π -dependent GPD. To do that we use a t_π -dependent pionic parton distribution function. The pionic parton distributions including a t_π -dependence are parametrized as

$$v^\pi(x, t_\pi) = v^\pi(x) e^{t_\pi f(|x|)}, \quad (3.138)$$

$$\bar{q}^\pi(x, t_\pi) = \bar{q}^\pi(x) e^{t_\pi f(|x|)}. \quad (3.139)$$

For an optimal description of small, intermediate and large x the function $f(x)$ is parametrized as

$$f(x) = \alpha'(1-x)^3 \log \frac{1}{x} + B(1-x)^3 + Ax(1-x)^2, \quad (3.140)$$

with $\alpha' = 0.9 \text{ GeV}^{-2}$. For the pionic parton distribution of GRS the parameters are $A = 2.19 \text{ GeV}^{-2}$, $B = -0.38 \text{ GeV}^{-2}$. For further detail see [104]. Another parametrization we include is the Sutton, Martin, Roberts, and Stirling [108] parametrization. They give different parametrization for various choices of the sea-quark distribution, where we choose a sea-quark distribution of 15%. The parton distribution functions at $Q^2 = Q_0^2 = 4 \text{ GeV}^2$ are

$$v_\pi = A_v x^{(\alpha-1)} (1-x)^\beta, \quad (3.141)$$

$$\bar{q}^\pi = x(u + \bar{d} + \bar{s}) = A_s (1-x)^{\eta_s}, \quad (3.142)$$

assuming that $u = \bar{d} = \bar{s}$. Appropriate parameters are $\alpha = 0.64$, $\beta = 1.08$, $A_s = 0.9$ and $\eta_s = 5$. We can add a t_π -dependence in the same way as for GRS, where the parameters for the function $f^q(x)$ are $A = 1.35 \text{ GeV}^{-2}$ and $B = 0.58 \text{ GeV}^{-2}$. In Fig. 3.9 we show v_π and \bar{q}^π for the two models of Glück, Reya and Schienbein and of Sutton, Martin, Roberts and Stirling to show the differences between them.

In Fig. 3.10 we show the real and imaginary parts of the Compton form factor for different models. This shows, that the real part of the Compton form factor is sensitive to the different models for small ξ_π .

3.6.2 Pion form factor

To determine the pion Compton form factor including the pionic parton distribution without a t_π -dependence we furthermore need the pion form factor F_π , containing the t_π -dependence. For very low values of Q^2 up to $Q^2 = 0.28 \text{ GeV}^2$ it is experimentally measured by scattering high energy pions off atomic electrons [109]. Going to higher Q^2 one can study the reaction $ep \rightarrow e'\pi^+n$. This process can be treated as quasi elastic scattering of the electron off a virtual pion from the proton. The longitudinal cross section is proportional to the pion form factor in the t -pole approximation, [109]. Up to $Q^2 = 1.6 \text{ GeV}^2$ the data follow a monopole form. Lattice data [110, 111, 112] are in good consistency with the data and show that a monopole ansatz describes the pion form factor very well, also for higher values of Q^2 . It is seen that

$$F_\pi(t_\pi) = \frac{1}{\left(1 - \frac{t_\pi}{m_{\text{mono}}^2}\right)} \quad (3.143)$$

gives a very good description of the data for $m_{\text{mono}} = 0.727(16) \text{ GeV}$ [110].

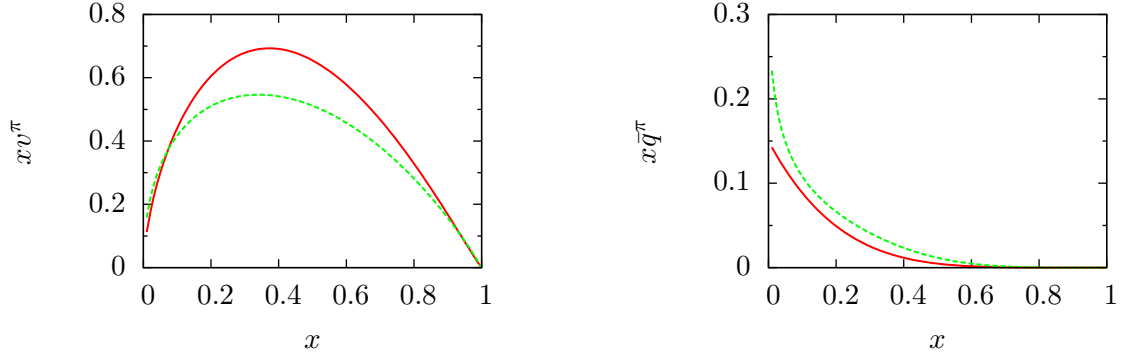


Figure 3.9: Pion PDFs at $Q^2 = 4 \text{ GeV}^2$ on the left for the valence distribution and on the right for the sea-quark distribution by Glück, Reya and Schienbein (green, dashed line) and by Sutton, Martin, Roberts and Stirling (red, solid line).

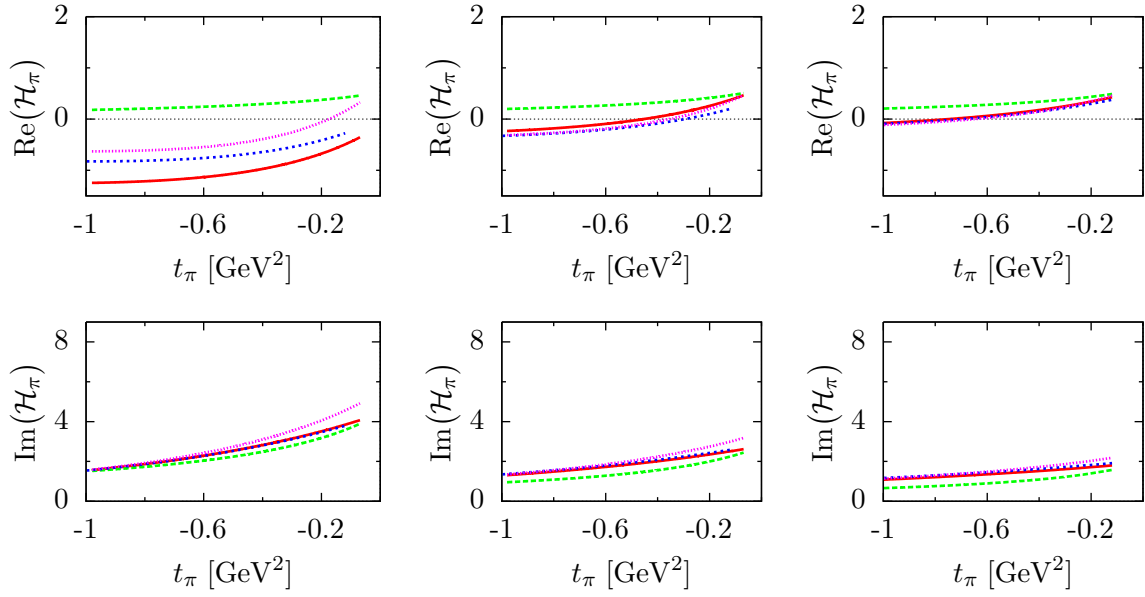


Figure 3.10: The upper three figures show the real parts of the Compton form factor integrated over x for $\xi_\pi = 0.2, 0.3$ and 0.4 from left to right and the lower three figures show the corresponding imaginary parts. The red (solid) line refers to the t_π -dependent Glück, Reya and Schienbein parametrization for the pion PDF, the green (dashed) line to the t_π -independent Glück, Reya and Schienbein parametrization for the pion PDF, the blue (dotted) line refers to the t_π -dependent parametrization by Sutton, Martin, Roberts and Stirling for the pion PDF and the pink (small dotted) line to the t_π -dependent Glück, Reya and Schienbein parametrization for the pion PDF, where the parameter b is set to 1. In all previous cases b was equal to 2.

3.7 Experimental extraction

In order to be able to measure the cross section several aspects have to be fulfilled. The luminosity has to be sufficient and the acceptance and efficiency of the detector have to be good enough. If the Compton amplitude of $ep \rightarrow e' \pi \gamma n$ can be experimentally extracted, we can compare our results to the data. The Compton amplitude is sensitive to the theoretically implemented model of the pion GPD. By inserting different models we can thus test their reliability.

The experiments measure the DVCS contribution through the interference with the Bethe–Heitler process. As we have seen in Eq. 2.84 the Bethe–Heitler contribution dominates in the kinematics we consider.

One possibility to eliminate the Bethe–Heitler contribution is to take the difference of the cross section for opposite beam charge or polarization. Hence we are left with a combination of the Compton amplitude and the interference. A clean separation can for example be achieved in experiments using electron and positron beams, because DVCS is linear in e_l and BH quartic, the interference term is projected out in the cross section differences and vanishes in their sum.

The beam polarization asymmetry can be measured using a longitudinally (L) polarized lepton beam and an unpolarized (U) target and is defined as

$$A_{LU}(\phi) = \frac{d\sigma(\vec{e}, \phi) - d\sigma(\overleftarrow{e}, \phi)}{d\sigma(\vec{e}, \phi) + d\sigma(\overleftarrow{e}, \phi)}, \quad (3.144)$$

where the arrows indicate positive (\rightarrow) and negative (\leftarrow) beam helicity.

When the time intervals between the flipping of the beam spin is short enough, efficiency and acceptance effects, which are not correlated to the beam spin, cancel out. This is valid for asymmetries, but not for absolute cross sections. Therefore measuring asymmetries is less susceptible to systematic effects than measurements of cross sections.

For proton DVCS this asymmetry is well known. It has a $\sin \phi$ modulation and is proportional to the imaginary part of the Compton form factor \mathcal{H} in $ep \rightarrow e' \gamma p$ and given by

$$A_{LU}(\phi) \sim F_1 \text{Im} \mathcal{H} \sin \phi. \quad (3.145)$$

In the process $ep \rightarrow e' \pi \gamma n$ we have the analog asymmetry

$$A_{LU}(\phi_\pi) \sim F_\pi \text{Im} \mathcal{H}_\pi \sin \phi_\pi. \quad (3.146)$$

Experimental measurements of the beam polarization asymmetry associated with DVCS are given in [113, 114] and are depicted in Fig. 3.11.

The beam charge asymmetry is defined as [104]

$$A_C(\phi) = \frac{d\sigma(e^+, \phi) - d\sigma(e^-, \phi)}{d\sigma(e^+, \phi) + d\sigma(e^-, \phi)}. \quad (3.147)$$

It is approximately given by a $\cos \phi$ dependence. Also this asymmetry is well known for proton DVCS. It is proportional to the real part of the Compton form factor \mathcal{H} in $ep \rightarrow e' \gamma p$ and given by

$$A_C(\phi) \sim F_1 \text{Re} \mathcal{H} \cos \phi, \quad (3.148)$$

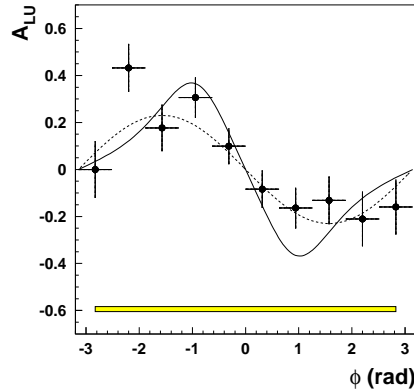


Figure 3.11: Figure taken from HERMES [113] showing the beam spin asymmetry A_{LU} for hard electroproduction of photons as a function of the azimuthal angle ϕ . The data correspond to the missing mass region between -1.5 and $+1.7$ GeV. The dashed curve represents a $\sin \phi$ dependence with an amplitude of 0.23, while the solid curve represents the result of a model calculation taken from [115]. The horizontal error bars represent the bin width, and the error band below represents the systematic uncertainty.

for $ep \rightarrow e' \pi \gamma n$ we have the analogous asymmetry

$$A_C(\phi_\pi) \sim F_\pi \operatorname{Re} \mathcal{H}_\pi \cos \phi_\pi. \quad (3.149)$$

Experimental results for the beam charge asymmetry of $ep \rightarrow e' \gamma p$ are given in [76] and shown in Fig. 3.12.

We consider in the following calculations of weighted cross sections which are defined as

$$A_{\text{BCA}}^{\cos \phi_\pi} = \int d\phi_\pi 2 \cos \phi_\pi \frac{d\sigma_{\text{BCA}}}{d\phi_\pi}, \quad (3.150)$$

$$A_{\text{BPA}}^{\sin \phi_\pi} = \int d\phi_\pi 2 \sin \phi_\pi \frac{d\sigma_{\text{BPA}}}{d\phi_\pi}. \quad (3.151)$$

This weighted beam charge (BCA) and beam polarization (BPA) cross sections will be computed for the HERMES and CLAS experiments and their results will be presented in Sec. 3.9.1 and 3.9.2.

3.8 Theoretical and kinematical cuts for HERMES and CLAS

Now we consider the kinematics for HERMES at DESY and CLAS at JLab. A maximum value of Q^2 is experimentally given by

$$Q_{\text{max, HERMES}}^2 = 4 \text{ GeV}^2 \quad Q_{\text{max, JLab}}^2 = 8 \text{ GeV}^2 \quad (3.152)$$

while we chose a minimum value of

$$Q_{\text{min}}^2 = 2 \text{ GeV}^2 \quad (3.153)$$

to justify factorization as well as the approximations done in the calculation of the cross section.

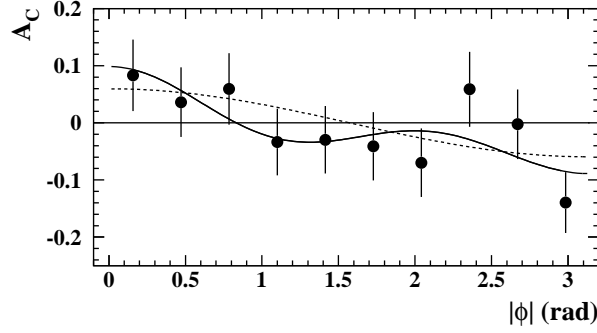


Figure 3.12: Figure taken from HERMES [76] showing the beam charge asymmetry A_C for the hard electroproduction of photons off protons as a function of the azimuthal angle ϕ , for the exclusive sample before background correction. Statistical uncertainties are shown. The dashed line shows the pure $\cos \phi$ dependence.

To stay in a physical regime values for t are constrained such that $|\cos \vartheta_n| \leq 1$ and this leads to a minimum value t_0 as given in Eq. 3.27. Furthermore we impose a maximum value for $|t|$ for two reasons, first to maximize the probability that the proton emits a pion and not a heavier particle as for example the ρ meson and secondly to keep the virtuality of the pion small to ensure the assumption to take the pion as on-shell for the calculation of the scattering amplitude. The cross section is dominated by small values of $|t|$, therefore only a small fraction of it is lost when imposing a constraint on t .

The boundary values for t_π ($t_{\pi,0}$ and $t_{\pi,1}$) follow from $\cos \vartheta_{\pi'}^{\pi\gamma} = \pm 1$. In the case of DVCS we constrain to small t_π while we require large values for the TDA case. The boundary conditions are given by

$$\begin{aligned}
 t_{\pi,0} &= \frac{1}{2s_\pi} \left[-Q^2(s_\pi + m_\pi^2) + (s_\pi - m_\pi^2) \right. \\
 &\quad \left. \left(t - s_\pi + \sqrt{Q^4 + (s_\pi - t)^2 + 2Q(s_\pi + t)} \right) \right] \\
 &\approx \frac{x_B(t(x_B - x_\pi) + m_\pi^2 x_\pi)}{(x_B - x_\pi)x_\pi}, \tag{3.154}
 \end{aligned}$$

$$\begin{aligned}
 t_{\pi,1} &= \frac{1}{2s_\pi} \left[-Q^2(s_\pi + m_\pi^2) + (m_\pi^2 - s_\pi) \right. \\
 &\quad \left. \left(s_\pi - t + \sqrt{Q^4 + (s_\pi - t)^2 + 2Q(s_\pi + t)} \right) \right] \\
 &\approx -\frac{Q^2 x_\pi}{x_B} \tag{3.155}
 \end{aligned}$$

in their exact form and in the Bjorken limit. But for DVCS we impose an upper cut on $|t_\pi|$. As we will see in Chapter 4 constraining t is very important since off-shell effects become more important for larger values of $|t|$.

Another integration variable is y , which is less than 0.85 in both kinematics. In the considered Bjorken limit we find that $y \simeq y_\pi$, thus we do not reach the critical point $\epsilon_\pi \rightarrow 0$ in the Bethe-Heitler term. For both experiments we constrain

$$y_{\min} = 0.15, \tag{3.156}$$

$$y_{\max} = 0.85. \tag{3.157}$$

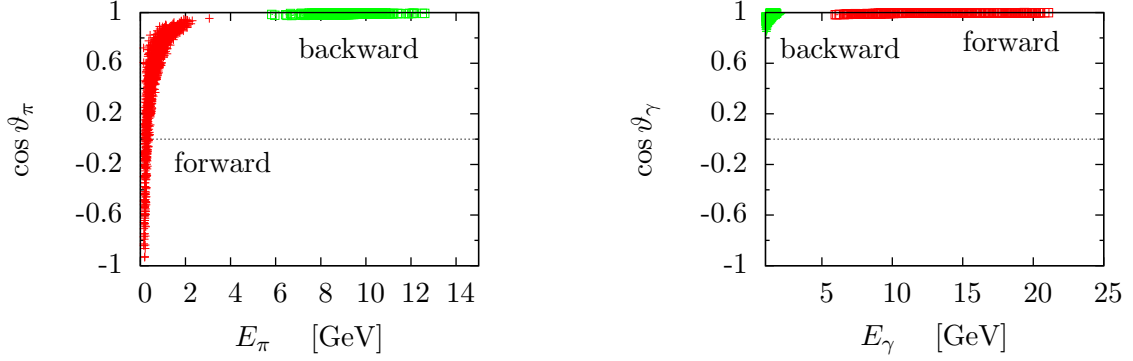


Figure 3.13: Distribution of the energy versus the cosine of the scattering angle for the pion (left) and the photon (right) in the proton rest frame. The distributions are shown for forward (red) and backward (green) scattering.

Apart from that x_B is constrained by the experiment as well and the allowed region is

$$0.01 < x_B < 0.5 \quad \text{HERMES}, \quad (3.158)$$

$$0.1 < x_B < 0.6 \quad \text{CLAS}. \quad (3.159)$$

We want to avoid final-state interactions, like further pion exchange, between the neutron and the pion, and resonances. Therefore we require minimum momenta for the pion and the neutron so that they do not have enough time close to each other to interact at all. This is satisfied when we take a minimum value of W^2 which is bigger than just the mass of the final state particles,

$$W^2 = (p_q + p_p)^2 > \alpha (\sqrt{s_\pi} + m_n)^2, \quad (3.160)$$

where α is chosen to be $\alpha = 1.1$. We take a value bigger than 1 to impose some momentum to the particles. In the HERMES experiment a lower limit is imposed

$$W^2 > 10 \text{ GeV}^2. \quad (3.161)$$

The variable x_π has to be bigger than x_B . Due to kinematical and experimental constraints on y and t , x_π is never reaching 1, thus we do not have to set an upper limit.

In order to get a sufficient detectability, the final-state pion and photon should be fast enough. We require at least

$$s_\pi > 4 \text{ GeV}^2. \quad (3.162)$$

To get an idea where to find the scattered pion and photon in the lab frame we plot $\cos \vartheta$ versus the corresponding energy for the pion and the photon. These points are created numerically and represent the possible kinematical values. Fig. 3.13 a) shows $\cos \vartheta_\pi$ versus the energy of the pion E_π in the proton rest frame. The '+' represent the scattering in a kinematic regime, where $t_\pi < -0.5 \text{ GeV}^2$ and the squares in the regime where we have $u_\pi < -0.5 \text{ GeV}^2$. Here one can see very well that we have two distinct regions for forward and backward scattering which can be distinguished experimentally. In forward scattering

the pions have small energies of up to 2 GeV but a wide scattering angles, while they have a large energy and very small polar angles for backward scattering. The same is shown in Fig. 3.13 b) for the photon. Here it is the other way round, in the forward scattering regime, the photon has a high energy and a small deflection angle and in the backward regime it has small energies up to 2 GeV and a broader scattering range. In both cases the two particles differ considerably from each other. Due to their explicit distinction in momentum and energy they can be distinguished in the detector.

For the two different experiments there are certain constraints on the threshold energy and the scattering angles.

For HERMES these are

$$E_\gamma > 0.8 \text{ GeV}, \quad (3.163)$$

$$E_\pi > 1.0 \text{ GeV}. \quad (3.164)$$

Constraints on the scattering angle in the HERMES detector are

$$2.3^\circ < \vartheta_\pi < 11.5^\circ \quad (3.165)$$

and from the additional recoil detector, which is of particular interest for our scattering process,

$$40^\circ < \vartheta_\pi < 140^\circ. \quad (3.166)$$

For CLAS 12 the minimum energies are

$$E_\gamma > 0.08 \text{ GeV}, \quad (3.167)$$

$$E_\pi > 0.2 \text{ GeV} \quad (3.168)$$

and constraints on the scattering angles are

$$5^\circ < \vartheta_\pi < 135^\circ, \quad (3.169)$$

$$2^\circ < \vartheta_\gamma < 40^\circ. \quad (3.170)$$

Furthermore CLAS has a better angular acceptance since it is a 4π detector while Hermes is composed of two parallel layers in front of the target.

3.8.1 Pion and photon in the proton laboratory frame

To confirm the distributions of the pion and photon angles just discussed we make a Taylor expansion of the energies and cosines of the particles in the proton rest frame. We expand m_p^2 , m_n^2 , m_π^2 , $t \rightarrow 0$. Further on we take the limit $t_\pi \rightarrow 0$ for forward and $u_\pi \rightarrow 0$ for backward scattering.

Treating first forward scattering gives for the pion

$$E_\pi^R \approx \frac{1}{2m_p x_\pi^2} \left[(m_\pi^2 - t_\pi)x_\pi + 2 \sin \phi_\pi \sqrt{(t - t_0)(1 - x_\pi)(x_\pi - x_B)x_\pi(t_\pi - t_{\pi 0})} + t((2 - x_\pi x_B - (1 - x_\pi)x_\pi)) \right] + \mathcal{O}\left(\frac{m^2}{Q}\right), \quad (3.171)$$

$$\cos \vartheta_\pi^R \approx 1 - \frac{x_\pi(1 - x_B^\pi)m_p}{E_\pi^R} + \mathcal{O}\left(\frac{m}{Q}\right). \quad (3.172)$$

Here we have a pion with a small to medium energy and a scattering angle showing no strong tendency. For the photon we get

$$E_\gamma^R \approx \frac{Q^2}{2m_p x_B} + \mathcal{O}(m), \quad (3.173)$$

$$\cos \vartheta_\gamma^R \approx 1 - \frac{2(1-y)m_p^2 x_B^2}{Q^2} + \mathcal{O}\left(\frac{m^4}{Q^4}\right). \quad (3.174)$$

This shows that the photon has a huge energy and a very small scattering angle.

By interchanging pion and photon we find in the backward regime for the pion energy and its polar angle

$$E_\pi^R \approx \frac{Q^2}{2m_p x_B} + \mathcal{O}(m), \quad (3.175)$$

$$\cos \vartheta_\pi^R \approx 1 - \frac{2m_p^2 x_B^2 (1-y)}{Q^2} + \mathcal{O}\left(\frac{m^2}{Q^2}\right). \quad (3.176)$$

As we can read from Eqs. 3.175 and 3.176, this leads to high energy pions moving in the forward direction.

For the photon we find

$$E_\gamma^R \approx \frac{\sin \phi_\pi \sqrt{(t-t_0)(1-x_\pi)(x_\pi-x_B)(-u_\pi x_\pi)}}{m_p x_\pi^2} + \mathcal{O}\left(\frac{m^2}{Q}\right). \quad (3.177)$$

$$\cos \vartheta_\gamma^R \approx 1 - \frac{2m_p^2 x_\pi (x_\pi - x_B)}{|u_\pi|} + \mathcal{O}\left(\frac{m^2}{Q^2}\right). \quad (3.178)$$

In contrast to the pion the photon is left with a quite small energy and is scattered broadly. These approximations are in good agreement with Fig. 3.13.

3.9 Results for the cross section and measurable asymmetries

3.9.1 Results for HERMES

In this section we give the expected cross section for the HERMES experiment at DESY. Experimentally the precision of measurements depends on the understanding of the systematics of the detector and its statistical accuracy. The latter is determined by the available beam current, the target density and the total measurement period weighted with a factor composed of beam and target polarization and the ratio of polarized and unpolarized nucleons.

We compute the cross sections and asymmetries for different constraints and make use of a numerical integration. The obtained values have thus an error due to the numerical uncertainty. This error is of the order of 1–2% and is not given explicitly below.

First of all we give the numerical result for deeply virtual scattering off a proton on the one hand and a pion on the other hand. Without imposing any cuts, and taking $2 \text{ GeV}^2 < Q^2 < 4 \text{ GeV}^2$ and $t > -0.5$ the results for the Bethe–Heitler processes are

$Q^2 > 2 \text{ GeV}^2$	proton	pion	(T.3.1)
BH	116 pb	132 pb	

This shows that the cross section for the pion is slightly bigger than the corresponding cross section for the proton, which is due to the behavior of the form factors.

Now we do the numerical computations for the process $ep \rightarrow e' \pi \gamma n$ starting from the eight-fold differential cross section of Eq. 3.116, performing the integration over the three polar angles ϕ_π , ψ_n and ψ_e , over the momentum transfers t and t_π and further on over Q^2 , y and x_π . The integration limits have already been discussed in Sec. 3.8. We use for the calculation two different models for the pion PDF. For the first model, J_1 , we take the pionic parton distribution from Eqs. 3.136 and 3.137 [107] and include the form factor for a t_π -dependence. We set the profile parameter $b = 2$. For the second model, J_2 , we add a t_π -dependence as shown in Eqs. 3.138 and 3.139 to the parton distribution and hence do not need the form factor to obtain a t_π -dependent GPD. Here again we take $b = 2$.

The contributions to the cross section, DVCS, BH and the two interference terms BCA and BPA as well as the corresponding event rates for the HERMES experiment for a minimum value Q^2 of 2 GeV^2 are

	Model J_1	#/year	Model J_2	#/year
DVCS	126 fb	1190	130 fb	1229
BH	3207 fb	30306	3207 fb	30306
BCA	-46 fb	435	-205 fb	1938
BPA	0	0	0	0

(T.3.2)

Since BPA is proportional to $\sin \phi_\pi$ the ϕ_π integration leads to zero. This term does thus not contribute to the total cross section. The value for the Bethe–Heitler cross section does not depend on the parametrization of the PDFs and is thus independent of the model. Due to the small luminosity of $L = 3 \cdot 10^{32} (\text{cm}^2\text{s})^{-1}$ [?] at HERMES the event rate per year is small.

To have realistic results we have to add constraints relevant for the HERMES detector. First of all the particles must have a minimum energy as given in Sec. 3.8. As it is shown in Fig. 3.13 a huge fraction of the pions have an energy below the threshold of 1.0 GeV and we are left with the reduced cross sections

	Model J_1	#/year	Model J_2	#/year
DVCS	30 fb	284	32 fb	302
BH	778 fb	7352	778 fb	7352
BCA	-20 fb	189	-98 fb	926

(T.3.3)

Secondly the detector is limited in size and by taking into account only those reactions, where the final-state pion and photon reach the detector (including the recoil detector) we obtain

	Model J_1	#/year	Model J_2	#/year
DVCS	5.1 fb	48	3.8 fb	36
BH	118 fb	1115	118 fb	1115
BCA	-0.2 fb	2	-2.1 fb	198

(T.3.4)

DVCS and Bethe–Heitler cross sections can in principle be measured, but since experimentalists have a much better access to the weighted beam charge and beam polarization asymmetries of Eqs. 3.150 and 3.151, we perform these weighted integrations and get the following results for the two models

	Model J_1	#/year	Model J_2	#/year
$A_{BCA}^{\cos \phi}$	-46 fb	434	-22 fb	207
$A_{BPA}^{\sin \phi}$	-15 fb	141	-25 fb	236

(T.3.5)

This shows that we can expect approximately 1200 events per year for the cross section and only up to 400 events for the weighted asymmetries. The measurement of cross sections at HERMES is affected by uncertainties related to acceptance effects. These uncertainties cancel to a large extent in the measurement of asymmetries. Thus, any comparison should be done at the level of asymmetries. However, since the event rate per year is small, it will be impossible to reach the statistical accuracy required for the measurement of these asymmetries.

3.9.2 Results for JLab

Another possible experiment, where the process $ep \rightarrow e' \pi \gamma n$ can be measured, is the CLAS experiment at JLab after the 12 GeV upgrade. The beam energy will be only 11 GeV for CLAS. Therefore the resulting center-of-mass energy is less than half of the center-of-mass energy available at HERMES. But in contrast to HERMES the detector covers a 4π range. Even more important, the luminosity at JLab is much higher, namely $L = 10^{35}(\text{cm}^2/\text{s})^{-1}$ [?]. In the calculation for JLab we use four different models. Two of them have already been introduced in the last chapter but are recalled here for sake of completeness:

- Model J_1 : It contains the pionic distribution functions from Glück, Reya and Schienbein [107]. The profile parameter b is set to $b = 2$. Furthermore we added a t_π -dependence (Eqs. 3.138 and 3.139) to the pionic distribution function.
- Model J_2 : It contains the pionic distribution functions from GRS [107] and b is set to $b = 2$, but no further t_π -dependence is added to the pionic parton distribution. Instead of that the t_π -dependence is provided by multiplying with the form factor as shown in Eq. 3.118.
- Model J_3 : It contains the pionic distribution functions from GRS [107] but b is set to $b = 1$. A t_π -dependence is added to the pionic distributions.
- Model J_4 : This model contains the pionic distribution functions from Martin, Sutton, Roberts and Stirling [108] and b is set to $b = 2$. A t_π -dependence is added to the pionic distributions.

Compared to the first model we always change one part, either the t_π -dependence or b or the parametrization of the pionic parton distributions. Hence it is easier to see the single

effects. Since we do not take final-state interactions into account, we take a minimum value for s_π of 4 GeV^2 and start with $2 \text{ GeV}^2 < Q^2 < 8 \text{ GeV}^2$. We immediately implement all constraints on energies and angles required by the detector and obtain

	Model J_1	#/year	Model J_2	#/year
DVCS	6.9 fb	23310	5.8 fb	23259
BH	175.3 fb	552195	175.3 fb	552195
BCA	-8.7 fb	27405	-8.6 fb	27090

(T.3.6)

	Model J_3	#/year	Model J_4	#/year
DVCS	8.5 fb	26775	5.1 fb	16065
BH	175.3 fb	552195	175.3 fb	552195
BCA	-10.0 fb	31500	-17.8 fb	56070

(T.3.7)

In the case of JLab kinematics there are more than half a million events per year for the $ep \rightarrow e\pi\gamma n$ process. Hence we can constrain Q^2 further and start at $Q^2 = 2.5 \text{ GeV}^2$. This is desirable because theoretically we need high Q^2 to justify factorization and to make approximations valid in the Bjorken limit. This leads to

	Model J_1	#/year	Model J_2	#/year
DVCS	2.2 fb	6930	2.4 fb	7276
BH	60.2 fb	183948	60.2 fb	183948
BCA	-1.9 fb	5985	-2.2 fb	6952

(T.3.8)

	Model J_3	#/year	Model J_4	#/year
DVCS	2.7 fb	8505	1.7 fb	5355
BH	60.2 fb	183948	60.2 fb	183948
BCA	-2.4 fb	7560	-0.5 fb	1575

(T.3.9)

Due to the high luminosity we are still left with more than 180000 events per year. Aside from Q^2 we increase the minimum value for $s_\pi > 5 \text{ GeV}^2$ to ensure that we do not take final state interactions into account and get

	Model J_1	#/year	Model J_2	#/year
DVCS	0.5 fb	1874	0.5 fb	1874
BH	21.1 fb	66498	21.1 fb	66498
BCA	-0.8 fb	2520	-0.4 fb	1264

(T.3.10)

	Model J_3	#/year	Model J_4	#/year
DVCS	0.7 fb	2205	0.4 fb	1890
BH	21.1 fb	66498	21.1 fb	66498
BCA	-0.8 fb	2520	-1.7 fb	2839

(T.3.11)

By cutting $Q^2 > 2.5 \text{ GeV}^2$ and $s_\pi > 5 \text{ GeV}^2$ we are still left with about 70000 events per year. These are enough events to analyze data, once they will be available.

In a next step we consider the resulting weighted cross sections as in the HERMES case. We give the values for the weighted cross sections of Eqs. 3.150 and 3.151 and the percentage of this cross sections compared to the Bethe–Heitler cross section. The DVCS and BCA contributions are much smaller than the Bethe–Heitler part and they furthermore partly cancel other. Thus the total cross section is approximately equal to the Bethe–Heitler cross section.

For the first model the weighted cross sections are

	Model J_1	%
$A_{\text{BCA}}^{\cos \phi}$	-15 fb	8
$A_{\text{BPA}}^{\sin \phi}$	-67 fb	48

(T.3.12)

The weighted cross sections for the polarization is much bigger than the beam charge asymmetry, but both of them are reasonably large. A_{BPA} is close to 50% of the Bethe–Heitler term and is large enough that it could be measured.

In the following we would like to compare the different models. First we will skip the t_π -dependence (model J_2) which gives

	Model J_2	%
$A_{\text{BCA}}^{\cos \phi}$	-11 fb	6
$A_{\text{BPA}}^{\sin \phi}$	-56 fb	32

(T.3.13)

Here we see that the weighted cross sections for the beam polarization is clearly smaller than for the model J_1 . The third model leads to

	Model J_3	%
$A_{\text{BCA}}^{\cos \phi}$	-17 fb	10
$A_{\text{BPA}}^{\sin \phi}$	-71 fb	41

(T.3.14)

Here the percentage of $A_{\text{BPA}}^{\sin \phi}$ is bigger than for the first two models. Finally by changing the pionic parton distributions we get

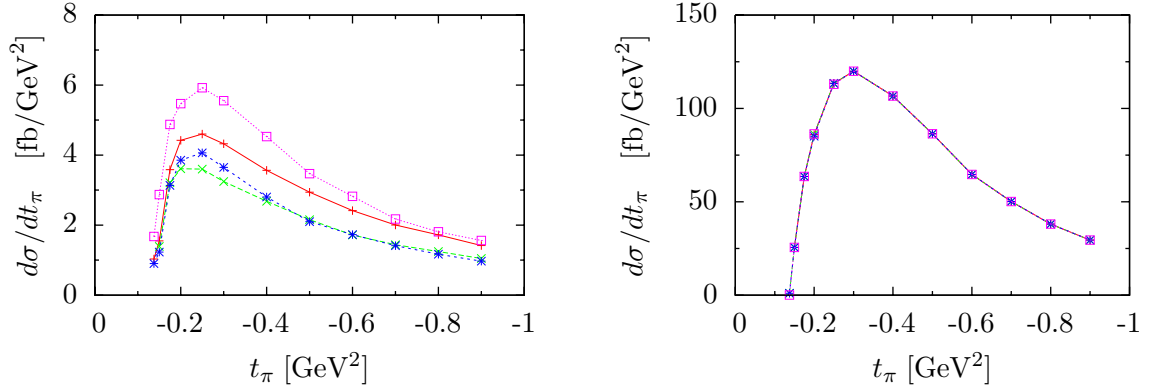


Figure 3.14: The left figure shows the differential cross section in t_π for deeply virtual Compton scattering and the right figure for the corresponding Bethe–Heitler process. The red (solid and pluses) line refers to the model J_1 , the green (dashed and crosses) line to model J_2 , the pink (small dotted and squares) line to model J_3 and the blue (dotted and stars) line to model J_4 .

	Model J_4	%
$A_{\text{BCA}}^{\cos \phi}$	-31 fb	17
$A_{\text{BPA}}^{\sin \phi}$	-53 fb	30

(T.3.15)

This comparison shows that we get significantly different numbers for the considered models. Comparing these results to experimental data will show which model gives the best description of the data. As before we can now further constrain the value of Q^2 . We set Q_{min}^2 to 2.5 GeV^2 and show the results for the weighted cross sections and the percentage of the corresponding Bethe–Heitler term for all four models

	Model J_1	%	Model J_2	%	Model J_3	%	Model J_4	%
$A_{\text{BCA}}^{\cos \phi}$	-3.4 fb	6	-4 fb	7	-4 fb	7	-8.3 fb	10
$A_{\text{BPA}}^{\sin \phi}$	-21 fb	35	-21 fb	35	-26 fb	43	-38 fb	35

(T.3.16)

For 30% of the Bethe–Heitler term, there are 57000 events per year. Since this number is high enough we proceed by taking the condition $s_\pi > 5 \text{ GeV}^2$ and obtain

	Model J_1	%	Model J_2	%	Model J_3	%	Model J_4	%
$A_{\text{BCA}}^{\cos \phi}$	-1.3 fb	6	-1.4 fb	7	-1.5 fb	7	-2.6 fb	12
$A_{\text{BPA}}^{\sin \phi}$	-6.2 fb	30	-5.8 fb	28	-7.3 fb	35	-6.1 fb	29

(T.3.17)

If we take the first model J_1 the weighted cross sections $A_{\text{BPA}}^{\sin \phi}$ is 30% of the Bethe–Heitler cross section which means that there are about 23000 events per year.

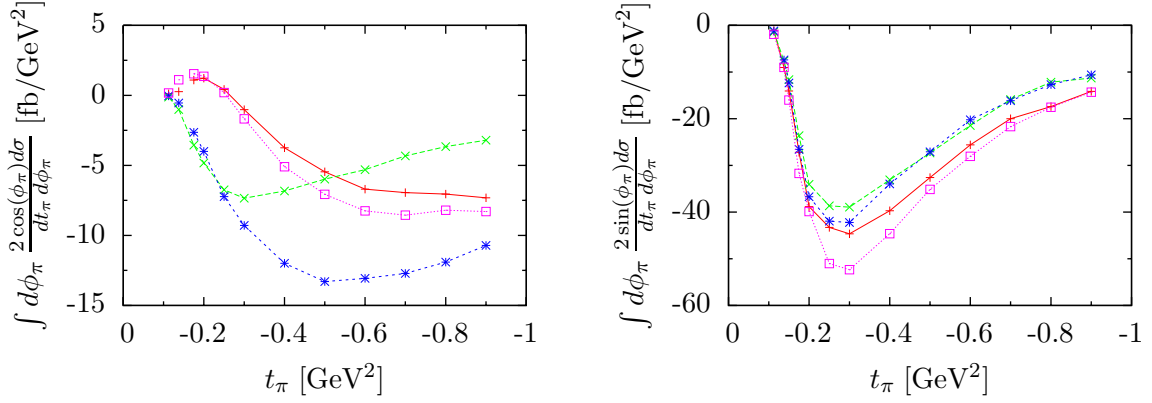


Figure 3.15: The two plots show the differential cross sections in t_π for the weighted interference terms, on the left side $A_{\text{BCA}}^{\sin \phi_\pi}$ and on the right side $A_{\text{BPA}}^{\cos \phi_\pi}$. Labeling as in Fig. 3.14.

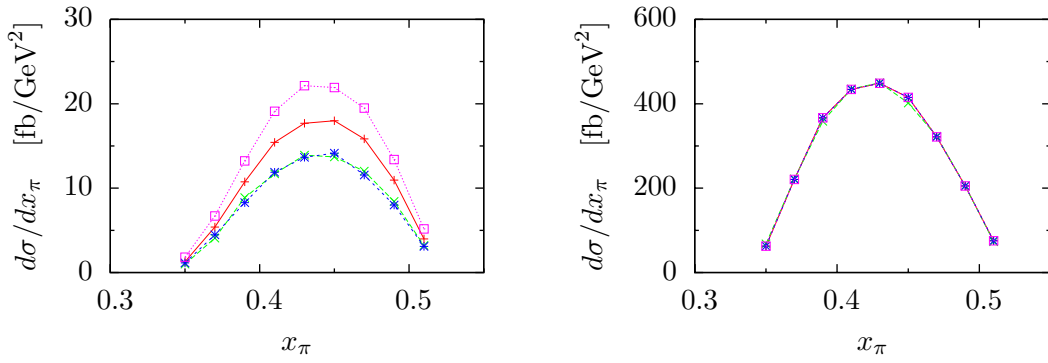


Figure 3.16: The left figure shows the differential cross section in x_π for deeply virtual Compton scattering and the right figure for the corresponding Bethe–Heitler process. Labeling as in Fig. 3.14.

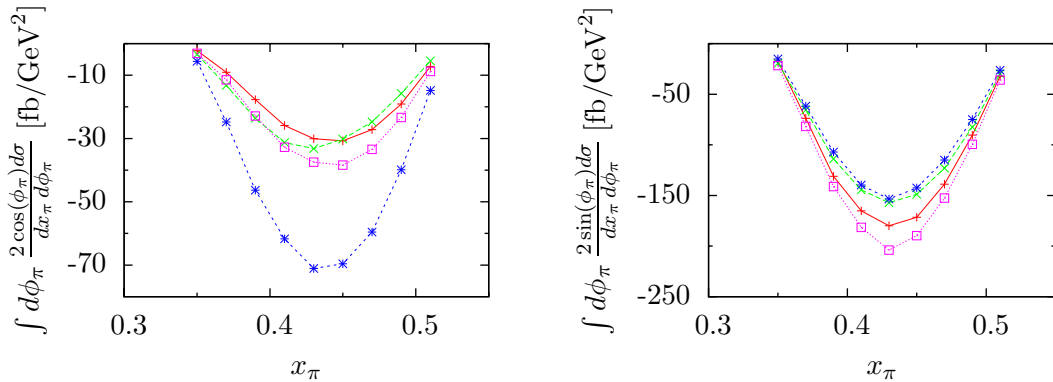


Figure 3.17: The two plots show the differential cross sections for x_π for the weighted interference terms, on the left side $A_{\text{BCA}}^{\sin \phi_\pi}$ and on the right side $A_{\text{BPA}}^{\cos \phi_\pi}$. Labeling as in Fig. 3.14.

Fig. 3.14 shows the t_π -dependence of the DVCS and Bethe–Heitler cross sections including all cuts for JLab kinematics and $Q^2 > 2.5 \text{ GeV}^2$, $s_\pi > 4 \text{ GeV}^2$ and $t_\pi > -0.9 \text{ GeV}^2$. The decrease for small $|t_\pi|$ in the differential DVCS cross section is due to the applied cuts. The plots show very well the expected decrease of the differential cross section for decreasing t_π .

To see what we expect from the experiment we show in Figs. 3.15 and 3.17 the weighted differential asymmetries for t_π and x_π for the different models. These asymmetries show very clearly the differences of the models, especially for the beam charge asymmetry. Furthermore these plots show that the beam polarization asymmetry is bigger than the beam charge asymmetry, which is in consistency with experimental results of electroproduction of photons off protons. Unfortunately there is no positron beam at JLab, therefore it is not possible to measure a beam charge asymmetry there. Nevertheless, results for the beam polarization asymmetry are theoretically very interesting and hence presented here.

The behavior for x_π is shown in Fig. 3.16. Here we see that x_π contributes to the differential cross section roughly below 0.5. To see where this maximum originates from we recall that we have an upper limit on t . This implies a maximum value for x_π

$$x_\pi < x_{\pi,\max} = \frac{1}{2} \left[\sqrt{\left(\frac{|t|_{\max}}{m_p^2}\right)^2 + 4\frac{|t|_{\max}}{m_p^2}} - \frac{|t|_{\max}}{m_p^2} \right] \approx 0.5. \quad (3.179)$$

A further constraint is that we impose lower cuts on s_π and Q^2 . From this we obtain in the Bjorken limit the approximated expression

$$x_\pi y \approx \frac{s_\pi + Q^2}{s}, \quad (3.180)$$

which implies a lower limit on x_π

$$x_{\pi,\min} \approx \frac{s_{\pi,\min} + Q_{\min}^2}{y_{\max} s} \approx 0.35. \quad (3.181)$$

This lower limit is not reached in the differential cross section. But having these two limits on x_π we understand, that the range of x_π is constrained.

Since the event rate at JLab is high we can now reduce the maximum value of $|t|$ further. This is important to ensure that we take into account only the one-pion exchange. Taking the Bethe–Heitler process as an example we show the changes of the cross section for different upper limits on $|t|$

	$t > -0.5 \text{ GeV}^2$	$t > -0.3 \text{ GeV}^2$	$t > -0.2 \text{ GeV}^2$
$Q^2 : 2 \dots 8 \text{ GeV}^2$	175 fb	56 fb	6.8 fb
$Q^2 : 2.5 \dots 8 \text{ GeV}^2$	65 fb	5.8 fb	0 fb

(T.3.18)

A cross section of 5 fb still corresponds to approximately 15000 events per year. Thus reducing $|t|_{\max}$ is an option that can be taken into account. But of course it is desirable to gain

more events per year. Therefore we consider y_{\max} once more. In the formula for the energy of the scattered electron in the proton rest frame

$$E_{e'} = E_e(1 - y) \quad (3.182)$$

y governs the energy of the scattered electron. If we take $y_{\max} = 0.95$ while the beam energy is 11 GeV we are left with $E_{e'} = 550$ MeV. Assuming that this energy is high enough to detect the electron we could rise the event rate by increasing y_{\max} . For the dominating Bethe–Heitler cross section and the measurable beam polarization asymmetry the results are for $t > -0.3 \text{ GeV}^2$ and $2 \text{ GeV}^2 < Q^2 < 8 \text{ GeV}^2$

y_{\max}	0.95	0.9	0.85
BH	369 fb	144 fb	59 fb
$A_{\text{BPA}}^{\sin \phi}$	-10.7 fb	-6.1 fb	-3.6 fb

(T.3.19)

and for $t > -0.3 \text{ GeV}^2$ and $2.5 \text{ GeV}^2 < Q^2 < 8 \text{ GeV}^2$

y_{\max}	0.95	0.9	0.85
BH	117 fb	32 fb	5 fb
$A_{\text{BPA}}^{\sin \phi}$	-2.1 fb	-0.9 fb	0 fb

(T.3.20)

Here we have to make a compromise of what we would like to impose theoretically and what can be performed experimentally. In any case we can gain a sufficient event rate.

The computed values for the cross sections and asymmetries can be compared to the experiment after the upgrade at JLab will be made and data are analyzed. In addition to the models presented here it is possible to implement further available models. Experiments will then show which one fits best.

In addition we show in Fig. 3.18 and 3.19 the differential cross sections and asymmetries in t . These plots include all cuts explained in Sec. 4.7 and $s_\pi > 4 \text{ GeV}^2$, $2.5 \text{ GeV}^2 < Q^2 < 8 \text{ GeV}^2$ and $t_\pi > -0.9 \text{ GeV}^2$. The left side of Fig. 3.18 shows the differential cross section for DVCS and the right side for Bethe–Heitler. In both cases we see the decrease for decreasing t . Further more these plots show very clearly that there is no contribution for $t > -0.2 \text{ GeV}^2$. This is in agreement with the results of T.3.18 where we get no cross section for $t > -0.2 \text{ GeV}^2$. In Fig. 3.19 the weighted asymmetries show very clear the differences of the implemented models.

The results manifest that we get a sufficient event rate for CLAS. Thus the process $ep \rightarrow e\pi\gamma n$ offers a possibility to investigate the pion GPD H_π . Besides we implemented different models which can be distinguished in the weighted asymmetries very well. The CLAS experiment can provide important measurements in the future to determine H_π and reveal the inner structure of the pion.

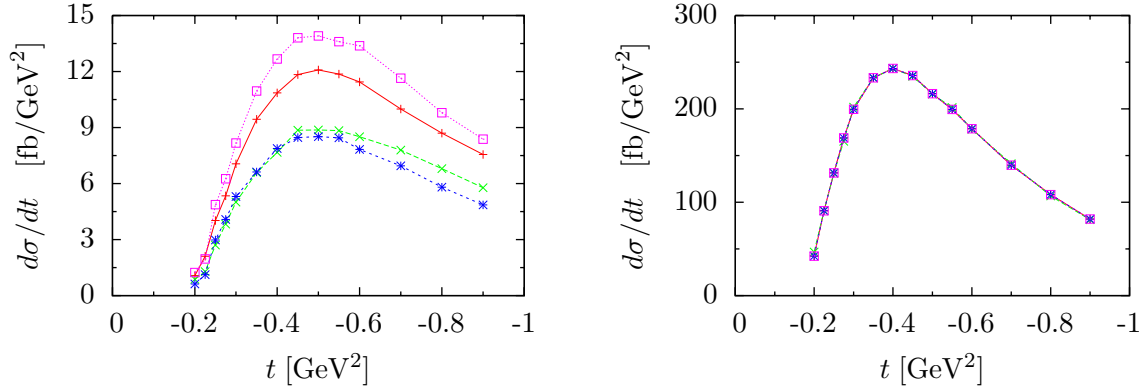


Figure 3.18: The left figure shows the differential cross section of $ep \rightarrow e'\pi\gamma n$ in t for deeply virtual Compton scattering and the right figure for the corresponding Bethe-Heitler process. Labeling as in Fig.3.14.

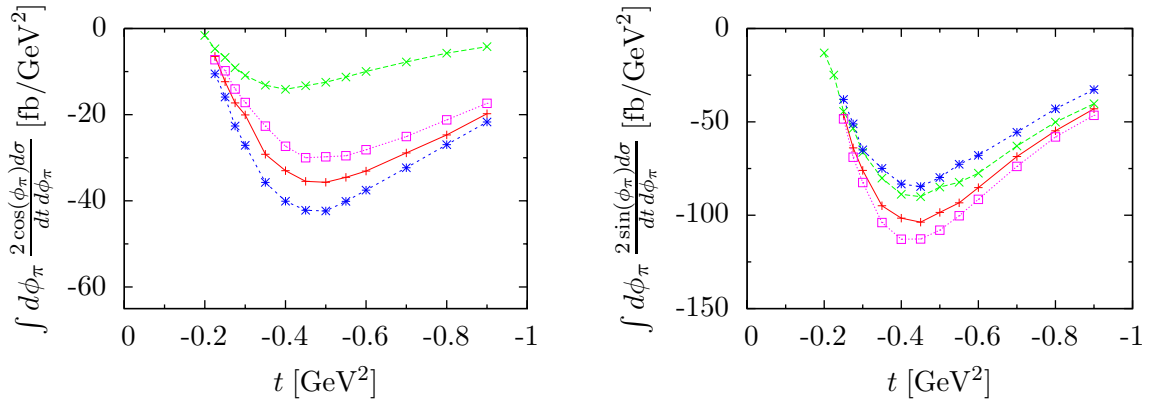


Figure 3.19: The two plots show the differential cross sections in t for the weighted interference terms, on the left side $A_{BCA}^{\sin \phi_\pi}$ and on the right side $A_{BPA}^{\cos \phi_\pi}$. Labeling as in Fig. 3.14.

Chapter 4

Electron deuteron scattering

Before considering any scattering processes involving the deuteron we will give a brief summary how the deuteron, the nucleus of the deuterium, was discovered.

In order to remove the discrepancy between different mass measurements of hydrogen Birge and Menzel [116] proposed in 1931 the existence of an isotope, the deuterium. This hypothesis was experimentally confirmed some months later [117]. The deuteron has been of great interest since then. It is the only stable two-nucleon bound state and therefore very interesting for nuclear theory. Already in 1933 deuterons were used as accelerated projectiles [118, 119] and the first photodisintegrations $\gamma d \rightarrow pn$ were measured in 1934 [3]. At that time it was thought that the nucleus was composed of protons and electrons, the only known charged particles. This idea was supported by the observation that nuclei emit electrons through β -decay. Furthermore the electrons were meant to cancel some of the positive charge of the proton. Even after the discovery of the neutron [3], shortly after the discovery of the deuteron, this problem was not settled, since the first assumption of the neutron was that it is composed of an electron and a proton. Only after accepting the Fermi theory of the β -decay [120, 121] the electron-proton model of the neutron began to abandon.

In this chapter we will first briefly discuss basic properties of the deuteron and introduce its GPDs and the wave function to finally compute the total cross section of the process $ed \rightarrow e'p\gamma n$.

4.1 Basic properties of the deuteron

The deuteron is a very weakly bound particle. It does not have excited states, since these states are not bound anymore. Its binding energy can be obtained by measuring the γ -rays coming from radiative np capture with thermal nucleons [122]. It is precisely measured in different ways which are in very good agreement and it is found to be

$$E_{\text{bin}} = 2.22463(4) \text{ MeV}. \quad (4.1)$$

Besides the deuteron mass is measured very precisely

$$m_d = 1.87614(19) \text{ GeV}. \quad (4.2)$$

Combining the binding energy and the mass of the deuteron leads to a precise determination of the neutron mass via [123]

$$m_n = m_d - m_p + E_{\text{bin.}} \quad (4.3)$$

$$= 939.56536(8) \text{ GeV} \quad (4.4)$$

From electron scattering experiments the charge radius of the deuteron is known to be about 2.1 fm [122].

The total angular momentum of the deuteron J is composed of the nucleon spins and their orbital angular momentum L

$$\vec{J} = \vec{s}_p + \vec{s}_n + \vec{L}. \quad (4.5)$$

Using photometry Murphy and Johnston [124] determined the molecular spectrum of deuterium and concluded that the spin of the deuteron is $J = 1$, which is in agreement with the further experimental measurements. Since the nucleon spins can either add up to 0 or 1 the orbital angular momentum can take not only $L = 0$. There are four ways to obtain a total angular momentum of one:

- \vec{s}_p and \vec{s}_n parallel with $L = 0$,
- \vec{s}_p and \vec{s}_n antiparallel with $L = 1$,
- \vec{s}_p and \vec{s}_n parallel with $L = 1$,
- \vec{s}_p and \vec{s}_n parallel with $L = 2$.

But since the parity of the deuteron is even, the $L = 1$ state is excluded, because parity associated with orbital motion is $(-1)^L$. Hence we are left with the s -wave ($L = 0$) and the d -wave ($L = 2$) having parallel spin.

Furthermore the deuteron has isospin $I = 0$. In conclusion it is a spin triplet and an isospin singlet.

4.1.1 Magnetic moment of the deuteron

One important property of the deuteron is its magnetic dipole moment. First measurements were already made in 1934 by Rabi [125]. Considering only the $L = 0$ part would lead to a magnetic moment just equal to the sum of the magnetic moments of the nucleons

$$\mu_d = \mu_p + \mu_n = 0.879804 \mu_N, \quad (4.6)$$

where μ_N is the nuclear magneton. In contrast to that, the observed value is $0.8574376(4) \mu_N$ which is a slight deviation from the measured value. This discrepancy can be ascribed to the small admixture of the d state ($l = 2$) in the deuteron wave function

$$\psi_d = a_s \psi(L = 0) + a_d \psi(L = 2). \quad (4.7)$$

Therefrom the magnetic moment follows to be

$$\mu_d = a_s^2 \mu(L = 0) + a_d^2 \mu(L = 2), \quad (4.8)$$

where $\mu(L = 0)$ is given in Eq. 4.6. Comparing this result to the measured value a good consistency is obtained from $a_s^2 = 0.96$ and $a_d^2 = 0.04$.

4.1.2 Electric quadrupole moment of the deuteron

A further significant feature is the electric quadrupole moment Q_d of the deuteron, which neither the proton nor the neutron possesses and hence must come from the $L = 2$ contribution. This quadrupole moment was discovered in 1939 [126] and has the consequence that the nuclear force cannot be central but has to be more complex.

The proton-neutron interaction depends on the orientation of their spins to each other as well as their spin orientation with respect to the line passing through the two nucleons. This explains the quadrupole moment and indicates that the proton distribution in the deuteron ground state is extended in the direction of the total spin of the system. The quadrupole moment is given by

$$Q_d = \frac{1}{20} \int_0^\infty dr r^2 w(r) \left(\sqrt{8} u(r) - w(r) \right). \quad (4.9)$$

Calculations of the quadrupole moment need relativistic potentials and lead to an admixture of the d -wave of a few percent, which is consistent with the value deduced from the magnetic dipole. Although there is a good agreement for the admixture of the d -wave for μ_d and Q_d the percentage of the admixture for the magnetic moment is quite uncertain. The nucleons in the deuteron are neither free nor strongly bound, other effects like spin-orbit interactions, relativistic effects and meson exchanges can as well have an effect on μ_d , but may also cancel each other. Scattering experiments verify a d -wave admixture in the range of 4%. For further details see [127].

4.2 Deuteron in exclusive processes

In the scattering process where an electron scatters off the deuteron, the deuteron can either serve as a source of weakly bound protons and neutrons or it acts as a single particle. In the latter case the deuteron stays intact after the scattering. This occurs in a non negligible fraction of events and is studied *e.g.* in [128, 129, 130] but will not be further considered in this thesis. We investigate the incoherent case where the deuteron breaks up.

A simple approach to model deuteron scattering is that the interaction takes place with one quark of one of the nucleons while the other nucleon is just a spectator. This is known as impulse approximation and depicted in Fig. 4.2. Possible kinematical scattering regions are shown in Fig. 4.1. In our work we use the impulse approximation and retain only lowest Fock-space states in the deuteron wave function. Then the deuteron light-cone wave function can be linked to the non-relativistic deuteron wave function, which we are going to use in the numerical calculations.

To describe scattering processes involving the deuteron we introduce relevant kinematical variables, the GPDs and the form factors of the deuteron.

4.2.1 Kinematics

In the following we present the required deuteron variables, which will be labeled with a subscript d to distinguish from proton variables used before,

$$P_d = \frac{1}{2} (p_d + p_{d'}), \quad \Delta_d = p_d - p_{d'}, \quad \xi_d = -\frac{\Delta_d \cdot n_-}{P_d \cdot n_-}, \quad t_d = \Delta_d^2. \quad (4.10)$$

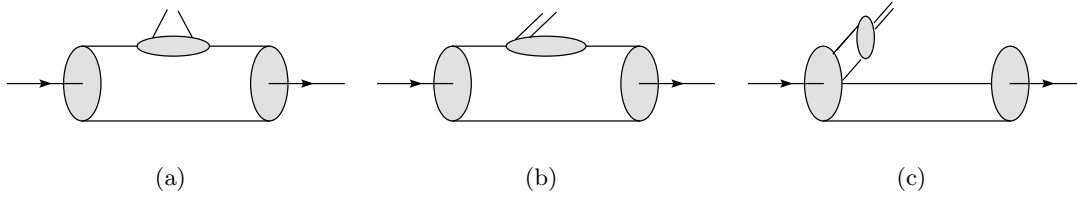


Figure 4.1: Kinematical regions for scattering off a deuteron, a) shows the emission and reabsorption of a quark, b) the scattering off a quark-antiquark pair and c) off a nucleon-antinucleon pair which is highly suppressed due to the high invariant mass of the nucleon pair.

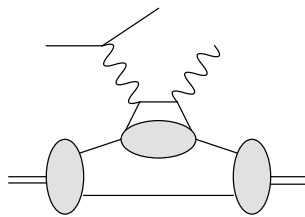


Figure 4.2: Impulse approximation for electron-deuteron scattering

Furthermore the deuteron has the polarization vectors $\varepsilon_d(p_d, \lambda_d)$ and $\varepsilon_{d'}(p_{d'}, \lambda_{d'})$ with the polarization $\lambda_d, \lambda_{d'}$ of the initial- and final-state deuteron, respectively. These vectors fulfill the conditions

$$\varepsilon_d \cdot p_d = \varepsilon_{d'} \cdot p_{d'} = 0. \quad (4.11)$$

Positivity of $\Delta_{d,\perp}^2$ implies a minimal momentum transfer $t_{d,0}$ for fixed ξ_d

$$t_{d,0} = -\frac{4\xi_d^2 m_d^2}{1 - \xi_d^2} \quad (4.12)$$

while for a given t_d there is an upper boundary for ξ_d

$$\xi_d^2 \leq \frac{-t_d}{4m_d^2 - t_d}. \quad (4.13)$$

In addition we label the momentum transfer t between the initial and final active nucleon from Eq. 1.34 with t_p to emphasize that it belongs to the nucleon.

4.2.2 Deuteron GPDs

Theoretical arguments for applying factorization theorems for the nucleon target are also valid in the deuteron case and hence a formalism for deuteron GPDs can be developed [131]. The deuteron is the simplest and therefore best known nucleus, after the proton, and is thus an optimal starting point to investigate hard exclusive scattering off nuclei [132, 133, 134]. Scattering experiments involving the deuteron are *e.g.* made at HERMES (DESY) and CLAS (JLab) and data are published in [135, 136].

The GPDs for the deuteron are nonperturbative matrix elements of quark-antiquark operators on the light-cone. These matrix elements determine the DVCS amplitude on a spin-one

target. Their general decomposition given in [130] can be written in terms of nine GPDs H_i and \tilde{H}_i ,

$$\begin{aligned} V_{\lambda_d, \lambda_{d'}} &= \int \frac{d\kappa}{2\pi} e^{ix\kappa 2P_d \cdot n_-} \langle p_{d'}, \lambda_{d'} | \bar{\psi}_d(-\kappa \cdot n_-) \not{n} \psi_d(\kappa \cdot n_-) | p_d, \lambda_d \rangle \\ &= \sum_{i=1}^5 \varepsilon_{d'}^{*\beta} V_{\beta, \alpha}^{(i)} \varepsilon_d^\alpha H_i(x, \xi_d, t_d), \end{aligned} \quad (4.14)$$

$$\begin{aligned} A_{\lambda_d, \lambda_{d'}} &= \int \frac{d\kappa}{2\pi} e^{ix\kappa 2P_d \cdot n_-} \langle p_{d'}, \lambda_{d'} | \bar{\psi}_d(-\kappa \cdot n_-) \not{n} \gamma^5 \psi_d(\kappa \cdot n_-) | p_d, \lambda_d \rangle \\ &= \sum_{i=1}^5 \varepsilon_{d'}^{*\beta} A_{\beta, \alpha}^{(i)} \varepsilon_d^\alpha \tilde{H}_i(x, \xi_d, t_d), \end{aligned} \quad (4.15)$$

where $|p_d, \lambda_d\rangle$ represents the deuteron state of momentum p_d and polarization λ_d .

The tensors $V^{(i)}$ and $A^{(i)}$ depend on p_d , $p_{d'}$ and n_- . Applying parity invariance it turns out that $V_{\beta, \alpha}^{(i)}$ are linear combinations of five tensor structures while $A_{\beta, \alpha}^{(i)}$ are linear combinations of seven tensors but only four of them are independent [128, 129, 130].

In a symbolic way the matrix elements of Eqs. 4.15 and 4.14 can be expressed as a convolution of the deuteron wave function ψ_d and the corresponding nucleon GPDs

$$V_{\lambda_d, \lambda_{d'}}(x, \xi_d, t_d) \sim \psi_{d'}^*(\alpha', \vec{k}'_\perp, \lambda'_1, \lambda'_2) \otimes H, E(x, \xi, t) \otimes \psi_d(\alpha', \vec{k}_\perp, \lambda_1, \lambda_2), \quad (4.16)$$

$$A_{\lambda_d, \lambda_{d'}}(x, \xi_d, t_d) \sim \psi_{d'}^*(\alpha', \vec{k}'_\perp, \lambda_1, \lambda'_2) \otimes \tilde{H}, \tilde{E}(x, \xi, t) \otimes \psi_d(\alpha', \vec{k}_\perp, \lambda_1, \lambda_2), \quad (4.17)$$

where $\alpha = p_2^+ / p_d^+$ is the plus-momentum carried by the initial active nucleon, labeled with the index 2, and k_\perp is its transverse momentum in a frame where the total transverse momentum of the deuteron vanishes.

4.2.3 Deuteron form factors

The vector and axial currents for the spin-one deuteron are parametrized by the elastic form factors G_i , \tilde{G}_i [137].

$$\begin{aligned} \langle p_{d'} | \bar{\psi}(0) \gamma^\mu \psi(0) | p_d \rangle &= -G_1(t_d) \varepsilon_{d'}^* \varepsilon_d P_d^\mu + G_2(t_d) [\varepsilon_d^\mu (\varepsilon_{d'} \cdot P_d) \\ &\quad + \varepsilon_{d'}^{*\mu} (\varepsilon_d \cdot P_d)] - G_3(t_d) (\varepsilon_d \cdot P_d) (\varepsilon_{d'}^* \cdot P_d) \frac{P_d^\mu}{2m_d^2} \end{aligned} \quad (4.18)$$

$$\begin{aligned} \langle p_{d'} | \bar{\psi}(0) \gamma^\mu \gamma^5 \psi(0) | p_d \rangle &= -i\tilde{G}_1(t_d) \varepsilon_{\alpha\beta\gamma}^\mu \varepsilon_{d'}^{*\alpha} \varepsilon_d^\beta P_d^\gamma \\ &\quad + i\tilde{G}_2(t_d) \varepsilon_{\alpha\beta\gamma}^\mu \Delta_d^\alpha P_d^\beta \frac{\varepsilon_d^\gamma (\varepsilon_{d'}^* \cdot P_d) + \varepsilon_{d'}^{*\gamma} (\varepsilon_d \cdot P_d)}{m_d^2} \end{aligned} \quad (4.19)$$

These form factors are given by the first x -moments of the deuteron GPDs as in to the nucleon case

$$\int_{-1}^1 dx H_i(x, \xi_d, t_d) = G_i(t_d), \quad i = 1, 2, 3, \quad (4.20)$$

$$\int_{-1}^1 dx \tilde{H}_i(x, \xi_d, t_d) = \tilde{G}_i(t_d), \quad i = 1, 2, \quad (4.21)$$

$$\int_{-1}^1 dx H_4(x, \xi_d, t_d) = 0, \quad i = 4, 5, \quad (4.22)$$

$$\int_{-1}^1 dx \tilde{H}_3(x, \xi_d, t_d) = 0, \quad i = 3, 4. \quad (4.23)$$

In the case of H_4, H_5, \tilde{H}_3 and \tilde{H}_4 the first moments do not correspond to form factors of the local vector and axial vector currents and thus they vanish. The form factors are related to the charge monopole G_C , the magnetic dipole G_M and the charge quadrupole G_Q moments:

$$G_1(t_d) = G_C(t_d) - \frac{2}{3}\eta G_Q(t_d), \quad (4.24)$$

$$G_2(t_d) = G_M(t_d), \quad (4.25)$$

$$(1 + \eta)G_3(t_d) = G_M(t_d) - G_C(t_d) + (1 + \frac{2}{3}\eta)G_Q(t_d), \quad (4.26)$$

with $\eta = \frac{Q^2}{4m_d^2}$ which are normalized as

$$G_C(0) = 1, \quad (4.27)$$

$$G_Q(0) = m_d^2 Q_d, \quad (4.28)$$

$$G_M(0) = \frac{m_d}{m_p} \mu_d. \quad (4.29)$$

Experimental values are $G_M(0) = 1.714$ and $G_Q(0) = 25.38$ [138].

4.2.4 Helicity amplitudes

In the region $\xi_d < x < 1$ the GPDs can be represented in terms of scattering amplitudes of a quark in a deuteron [139]

$$\mathcal{A}_{\lambda_{d'} \pm, \lambda_d \pm} = \frac{1}{2}(V_{\lambda_d, \lambda_{d'}} + A_{\lambda_d, \lambda_{d'}}) \quad (4.30)$$

with the condition

$$\mathcal{A}_{-\lambda_{d'} - \mu, -\lambda_d - \mu} = (-1)^{\lambda_{d'} - \lambda_d} \mathcal{A}_{\lambda_{d'} \mu, \lambda_d \mu}. \quad (4.31)$$

From parity invariance it follows that there are nine independent quark helicity amplitudes. Since

$$\mathcal{A}_{0-, 0-} = (-1)^{0-0} \mathcal{A}_{0+, 0+}, \quad (4.32)$$

there are only four quark helicity dependent distributions \tilde{H}_i but five quark helicity independent distributions H_i and the number of the amplitudes is reduced by one. Time invariance does not reduce the number any further and leads to the condition

$$\mathcal{A}(x, \xi_d, t_d)_{\lambda_{d'} \mu, \lambda_d \mu} = (-1)^{\lambda_{d'} - \lambda_d} \mathcal{A}(x, -\xi_d, t_d)_{\lambda_{d'} \mu, \lambda_d \mu}. \quad (4.33)$$

H_2, H_4 and \tilde{H}_4 appear only in longitudinal deuteron polarization. Moreover, there are the gluon distributions in the deuteron as presented in [131]

$$4 \frac{(n_-)_\alpha \cdot (n_-)_\beta}{P \cdot n_-} \int \frac{d\kappa}{2\pi} e^{ix\kappa 2P_d \cdot n_-} \langle p_{d'}, \lambda_{d'} | F^{\alpha\mu}(-\kappa n_-) F_\mu^\beta(\kappa n_-) | p_d, \lambda_d \rangle = \sum_i \varepsilon_{d'}^{*\beta} V_{\beta\alpha}^{(i)} \varepsilon_d^\alpha H_i^g(x, \xi_d, t_d), \quad (4.34)$$

$$-4 \frac{(n_-)_\alpha \cdot (n_-)_\beta}{P \cdot n_-} \int \frac{d\kappa}{2\pi} e^{ix\kappa 2P_d \cdot n_-} \langle p_{d'}, \lambda_{d'} | F^{\alpha\mu}(-\kappa n_-) \tilde{F}_\mu^\beta(\kappa n_-) | p_d, \lambda_d \rangle = \sum_i \varepsilon_{d'}^{*\beta} A_{\beta\alpha}^{(i)} \varepsilon_d^\alpha \tilde{H}_i^g(x, \xi_d, t_d) \quad (4.35)$$

where $\tilde{F}^{\alpha\beta} = \frac{1}{2} \varepsilon^{\alpha\beta\gamma\delta} F_\gamma$ and the tensors $V^{(i)}, A^{(i)}$ are as for the quarks given in Eqs. 4.14 and 4.15.

The Q^2 behavior of the amplitudes and the selection rules for photon and meson helicity in $ed \rightarrow ed\gamma$ and $ed \rightarrow edM$ respectively, remain the same. This is because they depend only on the hard scattering kernel and do not depend on the target spin. All distributions appear in Compton scattering. Pion exchange does not contribute here, in contrast to the nucleon case where it gives information about \tilde{E}_p^g . The interference term gives for higher Q^2 information about linear combinations of GPDs weighted with the electromagnetic form factors $G_{1,2,3}(t)$.

4.3 Deuteron wave function

The wave function describes the physical state of the deuteron. It can be expanded in terms of s - and d -wave functions. We adopt the notation given in [138]:

$$\psi_M(\vec{r}) = \frac{u(r)}{r} \mathcal{Y}_{01}^{1M}(\theta, \phi) + \frac{w(r)}{r} \mathcal{Y}_{21}^{1M}(\theta, \phi), \quad (4.36)$$

where $u(r)/r$ and $w(r)/r$ are the radial wave functions and $\mathcal{Y}_{LS}^{JM}(\theta, \phi)$ the spin spherical harmonics [138]

$$\mathcal{Y}_{LS}^{JM}(\theta, \phi) = \sum_{m_L, m_S} \langle J, M_d | L, m_L; S, m_S \rangle Y_{LM_d}(\theta, \phi) | S, m_S \rangle. \quad (4.37)$$

Y_{LM} are the spherical harmonics (given in Appendix B) and $\langle J, M_d | L, m_L; S, m_S \rangle$ are the Clebsch-Gordon coefficients. $|S, m_S\rangle$ represents the deuteron state with spin S and its third component m_S . The reduced radial wave functions $u(r)$ and $w(r)$ give the probabilities for the s - and d -state, respectively, which are given by

$$P_s = \int_0^\infty u^2(r) dr, \quad P_d = \int_0^\infty w^2(r) dr. \quad (4.38)$$

Altogether they need to fulfill

$$P_s + P_d = 1. \quad (4.39)$$

Due to short range repulsion the radial wave function $u(r)/r$ is significantly reduced at $r < 1$ fm. For a given local potential the radial wave functions can be obtained from the coupled Schrödinger equation [123]

$$\left(\frac{d^2}{dr^2} - \gamma^2\right) u(r) = \bar{m}(V_{00}(r)u(r) + V_{02}(r)w(r)) \quad (4.40a)$$

$$\left(\frac{d^2}{dr^2} - \gamma^2 - \frac{6}{r^2}\right) w(r) = \bar{m}(V_{20}(r)u(r) + V_{22}(r)w(r)), \quad (4.40b)$$

where \bar{m} is twice the reduced mass of the proton and the neutron

$$\bar{m} = \frac{2m_p m_n}{m_p + m_n}. \quad (4.41)$$

In momentum space the deuteron wave function is given by

$$\Psi_d^{M_d}(\vec{q}_r) = \psi_0(q_r)\mathcal{Y}_{01}^{1M_d}(\vartheta, \phi) + \psi_2(q_r)\mathcal{Y}_{21}^{1M_d}(\vartheta, \phi), \quad (4.42)$$

where q_r is the relative momentum of the deuteron. The normalization is given by

$$\int_0^\infty dq_r q_r^2 (\psi_0^2(q_r) + \psi_2^2(q_r)) = 1. \quad (4.43)$$

The s - and d -wave functions $\psi_0(q_r)$ and $\psi_2(q_r)$ are also obtained by a coupled Schrödinger equation

$$\psi_0(q_r) = -\frac{\bar{m}}{\gamma^2 + q_r^2} \int dq'_r q_r'^2 (V_{00}(q_r, q'_r)\psi_0(q'_r) + V_{02}(q_r, q'_r)\psi_2(q'_r)) \quad (4.44a)$$

$$\psi_2(q_r) = -\frac{\bar{m}}{\gamma^2 + q_r^2} \int dq'_r q_r'^2 (V_{20}(q_r, q'_r)\psi_0(q'_r) + V_{22}(q_r, q'_r)\psi_2(q'_r)), \quad (4.44b)$$

which can be solved by matrix inversion [140] and are linked by a Fourier transform. The variable γ of Eq. 4.42 is given by [123]

$$\gamma^2 = \frac{4m_p^2 m_n^2 - (m_d^2 - m_p^2 - m_n^2)^2}{4m_d^2}. \quad (4.45)$$

We have plotted the numerical solution from Schiavilla [?] for the s - and d -waves which are depicted in Fig. 4.3 in configuration and momentum space. These will also be used in our numerical calculation of the cross section.

4.3.1 Deuteron potential

To determine the wave function we need to know the potential of the deuteron. The interaction between the two nucleons is in lowest order composed of an attractive central potential, which depends only on the distance \vec{r} between the two nucleons. Since there is no spin singlet state of the deuteron, the potential is strongly spin dependent. Thus there is a term for the potential depending on certain combinations of the nucleon spins. Applying parity and time reversal, the potential has the form

$$V(r) = -\left(\frac{\vec{s}_p \cdot \vec{s}_n}{\hbar} - \frac{1}{4}\right) V_1(r) + \left(\frac{\vec{s}_p \cdot \vec{s}_n}{\hbar} + \frac{3}{4}\right) V_2(r), \quad (4.46)$$

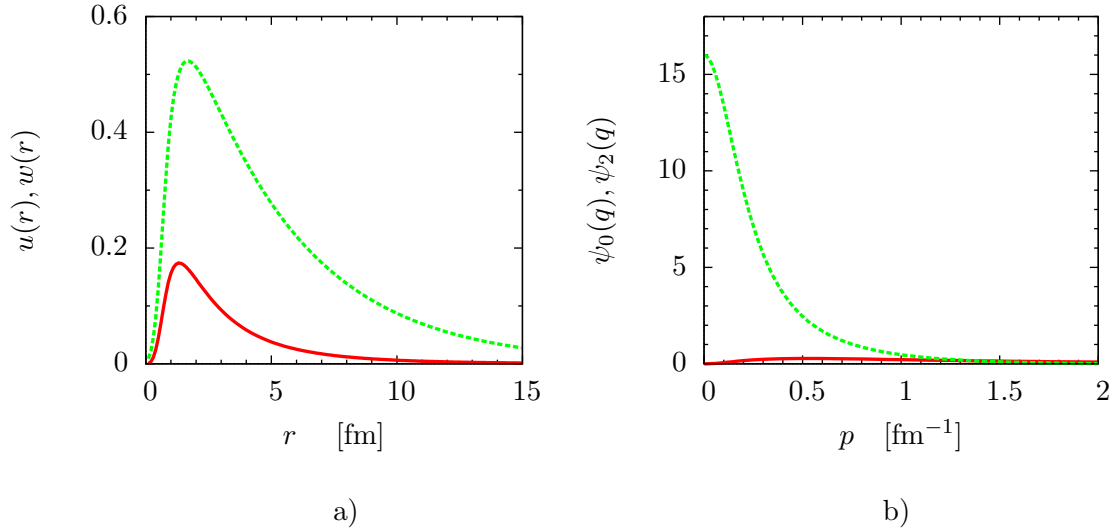


Figure 4.3: Deuteron wave function including the Argonne v_{18} potential in a) configuration space and in b) momentum space including the s -wave (green, dashed line) and d -wave (red, solid line).

with V_i giving separately the singlet and triplet behaviors, and \vec{s}_p and \vec{s}_n being the proton and neutron spin, respectively [127].

Wave functions with mixed orbital angular momentum states result from a non-central potential. This is called tensor potential. It depends on \vec{r} instead of r . Without loss of generality the tensor contribution to the inter-nucleon potential can be chosen to be of the form $V_T(r)S_{12}$, where $V_T(r)$ gives the force, the radial dependence and magnitude while the tensor character is given by

$$S_{12} = \frac{3(\vec{s}_p \cdot \vec{r})(\vec{s}_n \cdot \vec{r})}{r^2} - \vec{s}_p \cdot \vec{s}_n. \quad (4.47)$$

This leads to a deformation of the order of a few percent. The exchange of a virtual pion gives rise to the tensor potential. Due to parity conservation and the intrinsic negative parity of the pion there are two possibilities to conserve the total angular momentum, either the emitting and receiving nucleons must recoil with $l = 1$ or they must reverse their initial spin direction. Besides the deuteron potential becomes repulsive at short distances. This prevents the nucleus from getting too dense which is especially important in heavier nuclei.

The two bound nucleons inside the deuteron are not on their mass-shell. Therefore the calculation of the binding energy, which is needed for relativistic corrections of the potential, involves off-shell nucleon-nucleon interactions. This off-shellness is empirically underestimated and can only be provided from theory [141]. Despite a lot of work it has not been possible to assess the off-shell problem to the binding energy of a nucleus. Progress on that problem was made in nuclear few-body physics, *e.g.* by the Nijmegen [142, 143] and Argonne [?] groups.

In this thesis we are using the deuteron wave functions including the Argonne v_{18} potential [?, 144], which we will briefly discuss here.

4.3.1.1 Argonne v_{18} potential

The Argonne v_{18} potential [144] consists of a charge independent part with 14 operator components, three additional charge dependent operators and one charge asymmetric operator,

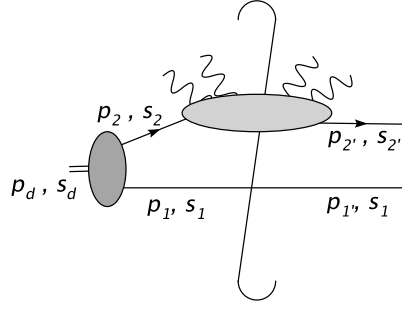


Figure 4.4: Deuteron cross section in the case where the deuteron breaks up.

with an electromagnetic interaction. This electromagnetic interaction contains the Coulomb potential, the Darwin-Foldy potential which gives a correction to central potential, vacuum polarization and magnetic moment terms with finite size effects, and in total 40 adjustable parameters. The Argonne v_{18} potential fits np , pp , low-energy nucleon-nucleon scattering parameters and deuteron properties.

The strong interaction potential is given in terms of S , I , I_3 which are spin, isospin and the third component of the isospin of a nucleon-nucleon pair, respectively. The predominant isospin conserving part of the nucleon-nucleon interaction is written as a linear combination of components proportional to the two isoscalars 1 and $\vec{\tau}_i \cdot \vec{\tau}_j$, [145], but moreover it also contains isospin breaking terms. Charge symmetry breaking terms are required for isovector ($\tau_{i,z} + \tau_{j,z}$) and isotensor ($3\tau_{i,z}\tau_{j,z} - \vec{\tau}_i \cdot \vec{\tau}_j$) structures. The full nucleon-nucleon interaction is the sum of a (dominant) isoconserving strong interaction, electromagnetic interaction and finally additional isospin-breaking terms.

4.4 Deuteron state

The deuteron state is represented by $|\Psi_d^{M_d}\rangle$, where M_d is the projection of the total angular momentum along the z -axis. In terms of the partial wave basis, the deuteron state in the basis of total helicity is given by

$$\begin{aligned} |\Psi_d^{M_d}\rangle &= |I\rangle \sum_{L=0,2} \int_0^\infty dq_r q_r^2 |q_r(L, 1) 1 M_d\rangle \psi_L(q_r) \\ &= |I\rangle \sum_{L=0,2} \int_0^\infty dq_r q_r^2 |1 M_d\rangle \psi_L(q_r). \end{aligned} \quad (4.48)$$

$|I\rangle$ represents the isospin state of the deuteron. The deuteron state projected to momentum space is [146]

$$\langle \hat{q} | \Psi_d^{M_d} \rangle = \Psi_d^{M_d}(\vec{q}_r), \quad (4.49)$$

where $\hat{q}_r = \vec{q}_r/|q_r|$ represents the angular dependence. Now $\Psi_d^{M_d}(\vec{q}_r)$ can be expressed in terms of the spin spherical harmonics and the deuteron wave function (Eq. 4.42) in momentum space. In the following formulas isospin will be omitted, since it is zero for the deuteron and does not effect the following calculations.

As mentioned in Sec. 4.1, the deuteron has $J = 1$ as well as $S = 1$, while the orbital angular momentum can either be zero or two. Expanding the wave function in terms of orbital angular momentum leads to

$$\begin{aligned} \Psi_d^{M_d}(\vec{q}_r) &= Y_{00}(\hat{q}_r) |1M_d\rangle \psi_0(q_r) \\ &+ \left\{ \sqrt{\frac{(2-M_d)(3-M_d)}{20}} Y_{2,M_d-1}(\hat{q}_r) |11\rangle \right. \\ &\quad - \sqrt{\frac{(2-M_d)(2+M_d)}{10}} Y_{2,M_d}(\hat{q}_r) |10\rangle \\ &\quad \left. + \sqrt{\frac{(2+M_d)(3+M_d)}{20}} Y_{2,M_d+1}(\hat{q}_r) |1-1\rangle \right\} \psi_2(q_r). \end{aligned} \quad (4.50)$$

We can separate for the single components of M_d

$$\begin{aligned} \Psi_d^1(\vec{q}_r) &= Y_{00} |11\rangle \psi_0(q_r) + \left(\sqrt{\frac{1}{10}} Y_{20} |11\rangle - \sqrt{\frac{3}{10}} Y_{21} |10\rangle + \sqrt{\frac{3}{5}} Y_{22} |1-1\rangle \right) \psi_2(q_r), \\ \Psi_d^0(\vec{q}_r) &= Y_{00} |10\rangle \psi_0(q_r) + \left(\sqrt{\frac{3}{10}} Y_{2-1} |11\rangle - \sqrt{\frac{2}{5}} Y_{20} |10\rangle + \sqrt{\frac{3}{10}} Y_{21} |1-1\rangle \right) \psi_2(q_r), \\ \Psi_d^{-1}(\vec{q}_r) &= Y_{00} |1-1\rangle \psi_0(q_r) + \left(\sqrt{\frac{3}{15}} Y_{2-2} |11\rangle - \sqrt{\frac{3}{10}} Y_{2-1} |10\rangle \right. \\ &\quad \left. + \sqrt{\frac{1}{10}} Y_{20} |1-1\rangle \right) \psi_2(q_r). \end{aligned} \quad (4.51)$$

The states $|1M_d\rangle$ in the Eq. 4.51 describing the deuteron are obtained from the coupling of the two nucleons using Clebsch-Gordon coefficients. In general this is

$$|1M_d\rangle = C(s_p, s_n, S, m_p, m_n, M_d) |s_p m_p\rangle |s_n m_n\rangle \quad (4.52)$$

and more explicitly we have

$$|11\rangle = \left| \frac{1}{2} \frac{1}{2} \right\rangle \left| \frac{1}{2} \frac{1}{2} \right\rangle = \left| \frac{1}{2} \frac{1}{2} \right\rangle, \quad (4.53)$$

$$\begin{aligned} |10\rangle &= \frac{1}{\sqrt{2}} \left(\left| \frac{1}{2} \frac{1}{2} \right\rangle \left| \frac{1}{2} -\frac{1}{2} \right\rangle + \left| \frac{1}{2} -\frac{1}{2} \right\rangle \left| \frac{1}{2} \frac{1}{2} \right\rangle \right) \\ &= \frac{1}{\sqrt{2}} \left(\left| \frac{1}{2} -\frac{1}{2} \right\rangle + \left| -\frac{1}{2} \frac{1}{2} \right\rangle \right), \end{aligned} \quad (4.54)$$

$$|1-1\rangle = \left| \frac{1}{2} -\frac{1}{2} \right\rangle \left| \frac{1}{2} -\frac{1}{2} \right\rangle = \left| -\frac{1}{2} -\frac{1}{2} \right\rangle, \quad (4.55)$$

$$\begin{aligned} |00\rangle &= \frac{1}{\sqrt{2}} \left(\left| \frac{1}{2} \frac{1}{2} \right\rangle \left| \frac{1}{2} -\frac{1}{2} \right\rangle - \left| \frac{1}{2} -\frac{1}{2} \right\rangle \left| \frac{1}{2} \frac{1}{2} \right\rangle \right) \\ &= \frac{1}{\sqrt{2}} \left(\left| \frac{1}{2} -\frac{1}{2} \right\rangle - \left| -\frac{1}{2} \frac{1}{2} \right\rangle \right), \end{aligned} \quad (4.56)$$

the state $|00\rangle$ is of course not relevant in the deuteron case.

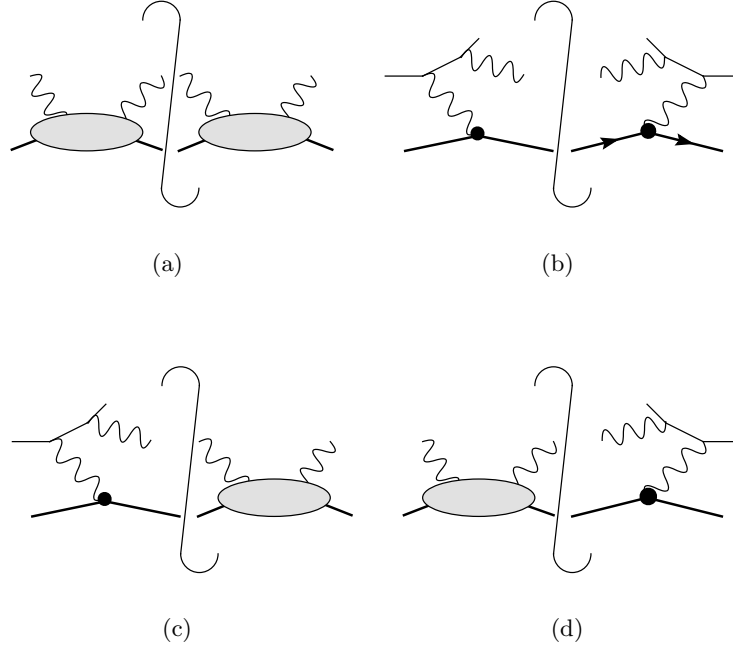


Figure 4.5: This figure shows the structure of the upper blob of the deuteron cross section from Fig. 4.4 which includes the active quark only for a) Compton scattering, b) Bethe–Heitler process and c,d) the two appearing graphs in the interference term.

4.5 Electron-deuteron cross section

For the cross section we need the matrix element $|\langle pn|\mathcal{O}|d\rangle|^2$ where the operator describes the upper blob in Fig. 4.4, which is shown in detail in Fig. 4.5. We express the state $\langle pn|$ by its spin state and average over the deuteron polarization and obtain

$$\begin{aligned} \frac{1}{3} \sum_{M_d=M_{d'}} \sum_{m_1=m_{1'}} \langle S m_S(pn)|\mathcal{O}|d\rangle \langle S m_S(pn)|\mathcal{O}|d\rangle^* \\ = \frac{1}{3} \sum_{M_d=M_{d'}} \sum_{m_1=m_{1'}} \langle S m_S(pn)|\mathcal{O}|d\rangle \langle d|\mathcal{O}|S m_S(pn)\rangle, \quad (4.57) \end{aligned}$$

where m_1 is the polarization of the spectator nucleon. The spectator nucleon does not change its spin. Now $|S m_S(pn)\rangle$ is the state of the proton and the neutron representing their spins. The operator \mathcal{O} contains the GPDs in case of nucleon DVCS, nucleon form factors in case of BH or both when considering the interference term. Now we insert the coupled state of the two nucleons from Eq. 4.52 and the explicit form of the deuteron state from Eq. 4.51 and sum over the deuteron polarization as well as the spectator nucleon polarization

$$\frac{1}{3} \sum_{M_d=M_{d'}} \sum_{m_1=m_{1'}} \langle S m_S(pn)|\mathcal{O}|d\rangle \langle d|\mathcal{O}|S m_S(pn)\rangle$$

$$\begin{aligned}
&= \frac{1}{3} \left\{ \left[\left\langle m_{2'} \left| \mathcal{O} \left| \frac{1}{2} \right. \right\rangle \left\langle \frac{1}{2} \left| \mathcal{O} \right| m_{2'} \right\rangle \left((Y_{00}\psi_0)^2 + \frac{3}{20} (Y_{21}\psi_2)^2 + \frac{1}{10} (Y_{20}\psi_2)^2 \right. \right. \right. \\
&\quad \left. \left. \left. + \sqrt{\frac{1}{10}} Y_{00} Y_{20} \psi_0 \psi_2 \right) \right]_{(m_d=1)} \right. \\
&\quad + \left[\left\langle m_{2'} \left| \mathcal{O} \left| -\frac{1}{2} \right. \right\rangle \left\langle -\frac{1}{2} \left| \mathcal{O} \right| m_{2'} \right\rangle \left(\frac{3}{5} (Y_{22}\psi_2)^2 + \frac{3}{20} (Y_{21}\psi_2)^2 \right) \right]_{(m_d=1)} \\
&\quad + \left[\left\langle m_{2'} \left| \mathcal{O} \left| \frac{1}{2} \right. \right\rangle \left\langle \frac{1}{2} \left| \mathcal{O} \right| m_{2'} \right\rangle \left(\frac{1}{2} (Y_{00}\psi_0)^2 + \frac{1}{5} (Y_{20}\psi_2)^2 \right. \right. \\
&\quad \left. \left. + \frac{3}{10} (Y_{2-1}\psi_2)^2 - \sqrt{\frac{1}{5}} Y_{00} Y_{20} \psi_0 \psi_2 \right) \right]_{(m_d=0)} \\
&\quad + \left[\left\langle m_{2'} \left| \mathcal{O} \left| -\frac{1}{2} \right. \right\rangle \left\langle -\frac{1}{2} \left| \mathcal{O} \right| m_{2'} \right\rangle \left(\frac{1}{2} (Y_{00}\psi_0)^2 + \frac{1}{5} (Y_{20}\psi_2)^2 \right. \right. \\
&\quad \left. \left. + \frac{3}{10} (Y_{2-1}\psi_2)^2 - \sqrt{\frac{1}{5}} Y_{00} Y_{20} \psi_0 \psi_2 \right) \right]_{(m_d=0)} \\
&\quad + \left[\left\langle m_{2'} \left| \mathcal{O} \left| \frac{1}{2} \right. \right\rangle \left\langle \frac{1}{2} \left| \mathcal{O} \right| m_{2'} \right\rangle \left(\frac{3}{20} (Y_{2-1}\psi_2)^2 + \frac{3}{5} (Y_{2-2}\psi_2)^2 \right) \right]_{(m_d=-1)} \\
&\quad + \left. \left[\left\langle m_{2'} \left| \mathcal{O} \left| -\frac{1}{2} \right. \right\rangle \left\langle -\frac{1}{2} \left| \mathcal{O} \right| m_{2'} \right\rangle \left((Y_{00}\psi_0)^2 + \frac{1}{10} (Y_{20}\psi_2)^2 + \frac{3}{20} (Y_{2-1}\psi_2)^2 \right. \right. \right. \\
&\quad \left. \left. \left. + \sqrt{\frac{1}{10}} Y_{00} Y_{20} \psi_0 \psi_2 \right) \right]_{(m_d=-1)} \right\}, \quad (4.58)
\end{aligned}$$

where the subscript $2'$ labels the final-state active nucleon. We are left with the wave functions, the spherical harmonics and a matrix element with only one free parameter $m_{2'}$. Mixing terms involving the matrix elements $\langle m_{2'} | \mathcal{O} | \frac{1}{2} \rangle \langle -\frac{1}{2} | \mathcal{O} | m_{2'} \rangle$ or $\langle m_{2'} | \mathcal{O} | -\frac{1}{2} \rangle \langle \frac{1}{2} | \mathcal{O} | m_{2'} \rangle$ occur for all contributions of M_d , but they always cancel each other and so they do not appear in the final result. Rearranging Eq. 4.58 leads to the simpler form

$$\begin{aligned}
&\frac{1}{3} \sum_{M_d=M_{d'}} \sum_{m_1=m_{1'}} \langle S m_S(pn) | \mathcal{O} | d \rangle \langle d | \mathcal{O} | S m_S(pn) \rangle \\
&= \left(\left\langle m_{2'} \left| \mathcal{O} \left| \frac{1}{2} \right. \right\rangle \left\langle \frac{1}{2} \left| \mathcal{O} \right| m_{2'} \right\rangle + \left\langle m_{2'} \left| \mathcal{O} \left| -\frac{1}{2} \right. \right\rangle \left\langle -\frac{1}{2} \left| \mathcal{O} \right| m_{2'} \right\rangle \right) \\
&\quad \times \left(\psi_0^2 \frac{1}{2} (Y_{00})^2 + \psi_2^2 \left(\frac{1}{10} |Y_{20}|^2 + \frac{1}{5} |Y_{21}|^2 + \frac{1}{5} |Y_{22}|^2 \right) + \psi_0 \psi_2 \frac{1}{3} \left(\sqrt{\frac{1}{10}} - \sqrt{\frac{1}{5}} \right) Y_{00} Y_{20} \right). \quad (4.59)
\end{aligned}$$

For simplicity let us now take into account the s -wave ψ_0 of the deuteron only, where we have $L = 0$. In this case Eq. 4.58 simplifies to

$$\frac{1}{3} \sum_{M_d=M_{d'}} \sum_{m_1=m_{1'}} \langle S m_S(pn) | \mathcal{O} | d \rangle \langle S m_S(pn) | \mathcal{O} | d \rangle^* \Big|_{L=0}$$

$$= Y_{00}^2 \psi_0^2 \frac{1}{2} \left(\left\langle m_{2'} \left| \mathcal{O} \left| \frac{1}{2} \right\rangle \right\rangle \left\langle \frac{1}{2} \left| \mathcal{O} \left| m_{2'} \right\rangle \right\rangle + \left\langle m_{2'} \left| \mathcal{O} \left| -\frac{1}{2} \right\rangle \right\rangle \left\langle -\frac{1}{2} \left| \mathcal{O} \left| m_{2'} \right\rangle \right\rangle \right). \quad (4.60)$$

Only certain spin combination can contribute because the spin of the nucleon taking place in the interaction has to conserve its spin. In the case of a s -wave there is no orbital angular momentum that could balance a spin flip of the nucleon. Furthermore the final-state photon is real and therefore we have in leading order only transverse photons. Thus we are left with

$$\begin{aligned} & \frac{1}{3} \sum_{M_d=M_{d'}} \sum_{m_1=m_{1'}} \langle S m_S(pn) | \mathcal{O} | d \rangle \langle S m_S(pn) | \mathcal{O} | d \rangle^* \Big|_{L=0} \\ &= Y_{00}^2 \psi_0^2 \frac{1}{2} \left(\left\langle \frac{1}{2} \left| \mathcal{O} \left| \frac{1}{2} \right\rangle \right\rangle \left\langle \frac{1}{2} \left| \mathcal{O} \left| \frac{1}{2} \right\rangle \right\rangle + \left\langle -\frac{1}{2} \left| \mathcal{O} \left| -\frac{1}{2} \right\rangle \right\rangle \left\langle -\frac{1}{2} \left| \mathcal{O} \left| -\frac{1}{2} \right\rangle \right\rangle \right) \end{aligned} \quad (4.61)$$

which describes scattering off an unpolarized nucleon.

In the center-of-mass frame of the electron-deuteron system the deuteron moves along the z -axes. Thus the polar angle ϑ_d of the deuteron is zero, which implicates that the spherical harmonics Y_{21} and Y_{22} disappear. In this kinematic regime only the two contributions in Eq. 4.58 involving Y_{00}^2 and Y_{20}^2 survive. The d -wave ψ_2 is suppressed compared to ψ_0 , especially for very low energy values the d -wave is negligible [123], which can be seen very clearly in Fig. 4.3. The term containing ψ_2 is further suppressed by a factor of $1/5$ compared to the term containing ψ_0 , as seen in Eq. 4.59. Hence the s -wave contribution strongly dominates.

For our calculation of the total cross section we can decompose the differential cross section into the phase space element, the flux factor and the scattering off one of the nucleons. Electron-deuteron scattering includes two possibilities, either the proton or the neutron acts as the active quark. To start with we choose scattering off the proton and keep the neutron as a spectator nucleon. Then the neutron spin is fixed. Since the s -wave contribution strongly dominates, we neglect the d -wave contribution. Averaging over the deuteron spin leads to

$$\begin{aligned} & \frac{1}{3} \sum_{M_d=M_{d'}} \sum_{m_n=m_{n'}} \frac{d\sigma(ed \rightarrow ep\gamma n)}{dQ^2 dy_d d\psi_{e'} dt_d dx_p d\psi_n dt_p d\phi_p} \\ &= \Phi_4^d F_{ed} \sum_{\text{spins}}' |\mathcal{T}_{ep}|^2 C^2(s_p, s_n, S, m_p, m_n, m_S) \eta_d \psi_0^2(q) Y_{00}^2(\hat{q}) \\ &\approx \frac{1}{4} \frac{x_p}{(2\pi)^3} \frac{1}{2} \eta_d \psi_0^2(q) Y_{00}^2 \frac{d\sigma(ep \rightarrow ep'\gamma)}{dQ^2 dy_p dt_p d\phi_p \psi_e}, \end{aligned} \quad (4.62)$$

where η_d is a correction factor for relativistic effects in the deuteron wave function. This is needed because we are using a non-relativistic wave function in our numerical computations. It ensures that in the case where the deuteron wave function is replaced by a δ -function we have the relation

$$\begin{aligned} \int \frac{d\sigma(ed \rightarrow enp\gamma)}{dQ^2 dy_d d\psi_{e'} dt_d dx_p d\psi_n dt_p d\phi_p} dt_d dx_p d\psi_n &= \frac{d\sigma(ep \rightarrow ep'\gamma)}{dQ^2 dy_p dt_p d\phi_p \psi_e} \\ &+ \frac{d\sigma(en \rightarrow en'\gamma)}{dQ^2 dy_n dt_n d\phi_n \psi_e}. \end{aligned} \quad (4.63)$$

To obtain η_d we substitute $dt_d dx_p d\psi_n$ by d^3q_r , t_p by q_r and the wave function by a δ -function

$$\frac{d^3p_n}{2E_n} = \frac{1}{4} dt_d dx_p d\psi_n = \frac{d^3q_r}{8E_n}, \quad (4.64)$$

$$t_d = m_d^2 + m_n^2 - \sqrt{4m_d^2 m_n^2 + m_d^2 q_r^2}, \quad (4.65)$$

$$\psi_0^2 = 4\pi\delta(|\vec{q}_r|), \quad (4.66)$$

while x_p is approximately 1/2. Taking into account for the moment only the scattering process off the proton and using the abbreviation $d\Gamma^5 = dQ^2 dy_d d\psi_{e'} dt_p d\phi_p$ leads to

$$\begin{aligned} \int \frac{d\sigma_{ed}}{d\Gamma^5 d^3p_{q_r}} d^3q_r &= \int d^3q_r \frac{1}{4E_n} \frac{1}{32(2\pi)^4} \eta_d 4\pi\delta(|\vec{q}_r|) \\ &\stackrel{!}{=} \frac{d\sigma_{ep}}{d\Gamma^5}. \end{aligned} \quad (4.67)$$

Therefrom we get

$$\eta_d = \frac{1}{\sqrt{s}} 16(2\pi)^3 \left(\frac{1}{2}(s - m_d^2) + 2m_d m_n \right). \quad (4.68)$$

Eq. 4.62 includes the differential cross section for scattering off a proton which is well-known and given *e.g.* in [79],

$$\frac{d\sigma(ep \rightarrow ep'\gamma)}{dQ^2 dy_p dt_p d\phi_p d\psi_{e'}} = \frac{1}{F_{ep}} \Phi_3^p |\mathcal{T}_{ep}|^2. \quad (4.69)$$

For the total cross section we need in addition the scattering off a neutron.

Since the deuteron is a loosely bound particle, the cross section of the electron-deuteron scattering should be approximately equal to the sum of the scattering off a proton plus scattering off a neutron. Therefore we determine the total cross sections of all of these processes and compare the results.

The deuteron can be used as a quasi-free neutron target. From the interference term of Eq. 3.110 being proportional to

$$F_1 \mathcal{H} + \xi(F_1 + F_2) \tilde{\mathcal{H}} - \frac{t}{4m_p^2} F_2 \mathcal{E} \quad (4.70)$$

it is obvious that in proton DVCS the GPDs H^q and \tilde{H}^q dominate, because the form factor F_1 is much bigger than F_2 . But for the neutron the situation changes, F_1 is much smaller than F_2 and hence the leading term is $F_2 \mathcal{E}$. The GPD E^q is basically unknown and unconstrained and thus the least known GPD accessible in DVCS. A measurement of neutron DVCS allows a flavor decomposition of GPDs. Moreover E^q and H^q enter Ji's sum rule on equal footing which gives an interesting insight on the nucleon orbital angular momentum. Thus neutron DVCS and therefore deuteron DVCS is highly relevant to reach new information on the GPDs. First experimental constraints on the GPD E^q expressed in terms of a constraint on the quark angular momentum are given in [?, ?].

To calculate nucleon DVCS we need the corresponding GPDs as an input. Thus we start by giving a model for these GPDs.

4.6 Modeling nucleon GPDs

In this section we are presenting the model assumptions we use for the nucleon GPDs, implemented in $e d \rightarrow e' \gamma p n$ cross section. As in the pion case we use the double distribution ansatz. Therefore we need the parton distributions and the form factors of the nucleons. For the GPDs H and E we need the unpolarized nucleon PDFs, in the case of \tilde{H} and \tilde{E} the polarized PDFs are involved. In this case we take into account only a t_p -dependent model, because such a model is more realistic.

4.6.1 Unpolarized nucleon PDFs

In [147] Pumplin *et al* give a model for the unpolarized parton distribution functions of a quark in the nucleon (CTEQ6M). Describing the data at a value of a low energy input scale $Q_0 = 1.3 \text{ GeV}$ the functional form of the unpolarized distribution is

$$x q(x, Q_0) = A_0 x^{A_1} (1-x)^{A_2} e^{A_3 x} (1 + e^{A_4 x})^{A_5}, \quad (4.71)$$

with independent parameters for the different parton flavor combinations $u_v = (u - \bar{u})$, $d_v = (d - \bar{d})$ and $\bar{u} + \bar{d}$, including the assumption $s = \bar{s} = 0.2(\bar{u} + \bar{d})$ at Q_0 . PDFs of higher Q are determined by evolution equations. But for energies at experiments we consider in this work, no further evolution is necessary. To distinguish \bar{u} and \bar{d} distributions the ratio is parametrized as

$$\frac{\bar{d}(x, Q_0)}{\bar{u}(x, Q_0)} = A_0 x^{A_1} (1-x)^{A_2} + (1 + A_3 x)(1-x)^{A_4}. \quad (4.72)$$

All numbers A_i are given in Appendix C.3.

To obtain a t_p -dependent GPD, without using the t_p -factorized ansatz, we adopt the formalism used for the pion. The t_p -dependent PDFs are constructed by making an exponential ansatz [104]

$$q(x, t_p) = q(x) e^{t_p f_q(|x|)}, \quad (4.73)$$

where the function $f_q(x)$ is given by

$$f_q(x) = \alpha'(1-x)^3 \log \frac{1}{x} + B_q(1-x)^3 + A_q x(1-x)^2, \quad (4.74)$$

with $A_u = 1.22$, $A_d = 2.59$, $B_u = 0.59$ and $B_d = 0.59$.

In analogy the ansatz for the GPD E can be taken by the PDF

$$e^q(x, t_p) = e^q(x) e^{t_p g_q(|x|)} \quad (4.75)$$

where $e^q(x)$ is the forward limit $e^q(x) = E^q(x, t_p = 0)$. It is normalized in a way that it gives the contribution of the quark flavor q to the anomalous magnetic moment

$$\int_0^1 dx e^q(x, t_p = 0, \mu) = \kappa_q. \quad (4.76)$$

The function $e^q(x)$ can be approximated by

$$e^q(x) = N_q \kappa_q x^{-\alpha} (1-x)^{\beta_q} \quad (4.77)$$

including

$$N_q = \frac{\Gamma(2 - \alpha + \beta_q)}{\Gamma(1 - \alpha)\Gamma(1 + \beta_q)}, \quad (4.78)$$

while $g_q(x)$ has the same form as $f_q(x)$ in Eq. 3.140,

$$g_q(x) = \alpha'(1-x)^3 \log \frac{1}{x} + D_q(1-x)^3 + C_q x(1-x)^2. \quad (4.79)$$

The free parameters are given in Appendix C.4 and are taken from [148].

4.6.2 Polarized nucleon PDFs

A parametrization for the polarized PDFs is *e.g.* given by Blümlein and Böttcher [149, 150]. At an input scale of $Q_0^2 = 4.0 \text{ GeV}^2$ they are parametrized as

$$x\Delta f_i(x, Q_0^2) = \eta_i A_i x^{a_i} (1-x)^{b_i} \left(1 + \gamma_i x + \rho_i x^{\frac{1}{2}}\right). \quad (4.80)$$

There are two factors controlling the behaviors of x , namely x^{a_i} controlling the low- x behavior and $(1-x)^{b_i}$ for large x . The A_i are the normalization constants

$$A_i^{-1} = \left(1 + \gamma_i \frac{a_i}{a_i + b_i + 1}\right) B(a_i, b_i + 1), \quad (4.81)$$

$$B(a, b) = \frac{\Gamma(a)\Gamma(b)}{\Gamma(a+b)}, \quad (4.82)$$

where $B(a, b)$ is the Euler-Beta function. They are chosen in a way that they fulfill the condition $\eta_i = \int_0^1 dx \Delta q_i(x, Q_0^2)$. The parameters needed to determine the polarized parton densities are given in Appendix C.5. The polarized valence distributions read

$$\Delta u_v(x) = \Delta u(x) - \Delta \bar{u}(x), \quad (4.83)$$

$$\Delta d_v(x) = \Delta d(x) - \Delta \bar{d}(x), \quad (4.84)$$

$$\frac{1}{6}\Delta \bar{Q}(x) = \Delta \bar{q}(x) = \Delta \bar{u}(x) = \Delta \bar{d}(x) = \Delta s(x) = \Delta \bar{s}(x). \quad (4.85)$$

We would like to implement a t_p -dependence in the parton distribution as we did for the unpolarized distribution, by using the ansatz

$$\Delta q_v(x, t_p) = \Delta q_v(x) e^{t_p \tilde{f}^q(x)} \quad (4.86)$$

with the profile function $\tilde{f}^q(x)$ being equal to $f^q(x)$ in Eq. 4.74.

4.6.3 Nucleon Compton form factors

The electron-proton cross section is parametrized by the Compton form factors (CFF), which themselves contain the GPDs. They are a key ingredient of the cross section and therefore presented below. Recalling the definition of the Compton form factors from Eqs. 3.90 and 3.91 as well as the integrals I^q , $I^{\bar{q}}$ and \tilde{I}^q , $\tilde{I}^{\bar{q}}$ from Eqs. 3.120 and 3.121 we can now compose the CFF of the nucleon

$$\begin{aligned} \mathcal{H}(x, \xi, t) &= \sum e_q^2 (I^q + I^{\bar{q}}) \\ &= \frac{4}{9} (I^u + I^{\bar{u}}) + \frac{1}{9} (I^d + I^{\bar{d}}), \end{aligned} \quad (4.87)$$

which contain the parton distribution functions. This can be done in an analogue way for the GPDs $\tilde{\mathcal{H}}$ and \mathcal{E} while for $\tilde{\mathcal{E}}$ we have

$$\tilde{\mathcal{E}} = I^q + I^{\bar{q}}. \quad (4.88)$$

$\tilde{\mathcal{E}}$ has no imaginary part since it is only defined between $-\xi$ and ξ and does not exceed the poles. For the GPD $\tilde{\mathcal{E}}$ we take the parametrization

$$\lim_{t \rightarrow m_\pi^2} \tilde{\mathcal{E}}^{u-d}(x, \xi, t) = \frac{\theta(|x| \leq \xi)}{2\xi} \phi\left(\frac{x + \xi}{2\xi}\right) \frac{2m_p f_\pi g_{\pi NN}}{m_\pi^2 - t}, \quad (4.89)$$

with the pion decay constant $f_\pi = 0.131$ GeV and the coupling $g_{\pi NN} = 14.7$ as before. Here we implement the pion distribution amplitude, given by [106]

$$\phi(z) = 6z(1-z). \quad (4.90)$$

4.7 Theoretical and kinematical cuts for CLAS

We perform the numerical integration including kinematical and boundary conditions of the CLAS experiment at JLab after the upgrade. At CLAS the limits on Q^2 are given by

$$Q_{\min}^2 = 1 \text{ GeV}^2 \quad Q_{\max, \text{JLab}}^2 = 8 \text{ GeV}^2. \quad (4.91)$$

For the integration we take a minimal value of

$$Q_{\min}^2 = 2 \text{ GeV}^2. \quad (4.92)$$

For the momentum transfer between the nucleons involved in the electron-nucleon scattering part, we have the boundary conditions

$$\begin{aligned} t_{p,0} &= \frac{1}{2s_p} \left[-Q^2(s_p + m_p^2) + (s_p - m_p^2) \right. \\ &\quad \left. \left(t_d - s_p + \sqrt{Q^4 + (s_p - t_d)^2 + 2Q(s_p + t_d)} \right) \right] \\ &\approx \frac{x_B(t_d(x_B - x_p) + m_p^2 x_p)}{(x_B - x_p)x_p}, \end{aligned} \quad (4.93)$$

$$\begin{aligned} t_{p,1} &= \frac{1}{2s_p} \left[-Q^2(s_p + m_p^2) + (m_p^2 - s_p) \right. \\ &\quad \left. \left(s_p - t_d + \sqrt{Q^4 + (s_p - t_d)^2 + 2Q(s_p + t_d)} \right) \right] \\ &\approx -\frac{Q^2 x_p}{x_B} \end{aligned} \quad (4.94)$$

in their exact form and in the Bjorken limit. This shows that the minimum value $t_{p,0}$ is function linear in t_d . We will see the importance of this t_d -dependence in Sec. 4.8.

The main contribution to the cross section is coming from values of x_p around 0.5, depicted in Fig. 4.7. Therefore we need to impose no constraints on x_p .

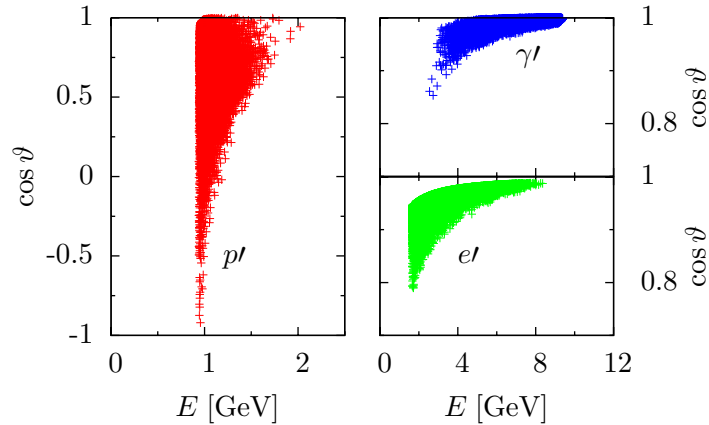


Figure 4.6: Distribution of the energy versus the cosine of the scattering angle for the scattered protons, electrons and photons.

The variable y is constrained by the experiment

$$0.15 < y < 0.85. \quad (4.95)$$

The upper cut on y is due to the detectability of the electron. The angle of the scattered electron is given by

$$\sin^2 \frac{\vartheta_{e'}}{2} = \frac{Q^2}{4E_e^2(1-y)} \quad (4.96)$$

which shows that the angle gets large for large values of y . These cannot be detected anymore.

Experimental cuts for x_B are

$$0.1 < x_B < 0.6. \quad (4.97)$$

Finally we have to constrain t_d . Due to $\cos \vartheta_d < |1|$ we get a minimum value for t_d

$$t_{d,0} = - \frac{x_p(m_d^2 - m_n^2 - m_d^2 x_p)}{1 - x_p}. \quad (4.98)$$

We take an upper cut of $t_{d,\max} = -0.5 \text{ GeV}^2$ which will be discussed in more detail in Sec. 4.8.

To get an idea how the energies and scattering angles of the final-state particles are distributed we plot these values as shown in Fig. 4.6. These points are created within the vegas routine in the numerical program. The plots show that the scattered protons are spread over a wide scattering range having a small energy, while the scattered electron and photon both have a large energy and small scattering angle.

4.8 Cross section results

Since the deuteron is a loosely bound particle, its cross section should be approximately equal to the sum of the corresponding proton and neutron cross sections. Therefore we start with

giving the results for the nucleon (N) cross sections

$$\int \frac{d\sigma_{eN}}{dt_N dQ^2 dy_N d\phi_N d\psi_{e'}} dt_N dQ^2 dy_N d\phi_N d\psi_{e'} = \int \frac{1}{F_{eN}} \Phi_3^N |\mathcal{T}_{eN}|^2 dt_N dQ^2 dy_N d\phi_N d\psi_{e'}. \quad (4.99)$$

The scattering amplitudes of the proton were given in Sec. 3.3.2.1 and are obtained for the neutron by replacing the form factors and GPDs. Adopting the boundary conditions from electron-deuteron scattering in Sec. 4.7 for electron-proton scattering for Q^2 , x_B and y , with an upper cut of t_p at -0.5 GeV^2 , the results are:

	proton	neutron
DVCS	18.5 pb	7.9 pb
BH	103.6 pb	21.8 pb
BCA	-5.1 pb	-0.2 pb

(T.4.1)

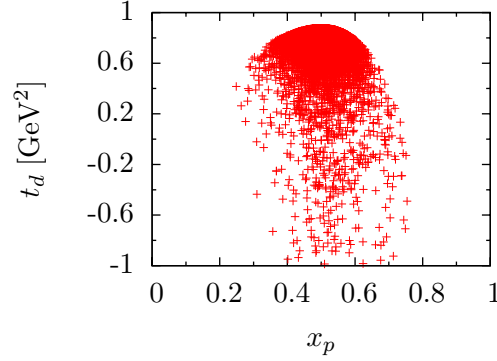
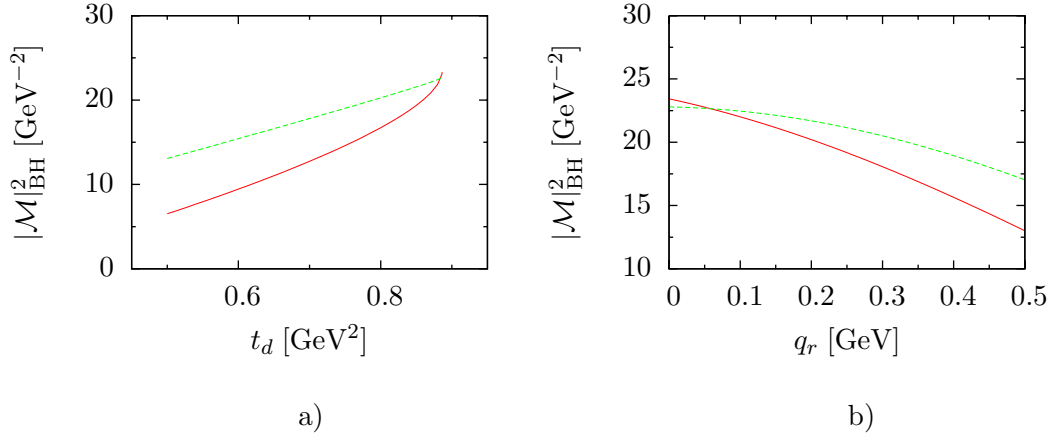
We see that the Bethe–Heitler contribution for the proton strongly dominates while it is much smaller in the neutron case.

Now we integrate out the differential electron-deuteron cross section as given in Eq. 4.62. In this calculation we require $s_p > 4 \text{ GeV}^2$. In electron-deuteron scattering the electron scatters either off the proton or the neutron and we give these results separately. They have to be added to obtain the complete electron-deuteron cross section.

deuteron:	proton	neutron
DVCS	18.6 pb	8.0 pb
BH	74.9 pb	17.0 pb
BCA	-3.6 pb	-0.8 pb

(T.4.2)

Here we see, that the DVCS cross sections are in good agreement with the results for DVCS off a nucleon, while the Bethe–Heitler cross section is suppressed. Therefore we consider the Bethe–Heitler amplitude in more detail. It reveals an implicit dependence on t_d . This is because the Bethe–Heitler amplitude depends on $\xi_p = x_B^p / (2 - x_B^p)$ and $(t_p - t_{p,0}) / t_p$ and these variables than again depend on t_d and x_p . So we see that the implemented BH amplitude of electron-nucleon scattering exhibits a t_d -dependence. This has to be treated with care. In electron-deuteron scattering t_d is the virtuality of the active nucleon, which we chose for this discussion to be the proton. Approaching the on-shell proton leads to $t_d \rightarrow m_p^2$. First of all we show in Fig. 4.7 the distribution of t_d and x_p and see that x_p is scattered around 0.5, while the dominating contribution of t_d is given for $t_d > 0.4 \text{ GeV}^2$. We show in Fig. 4.8 a) the t_d -dependence of the squared Bethe–Heitler amplitude for two different beam energies. Because we expect that the off-shell effect is weaker for higher center-of-mass energies we show the t_d -dependence for $s = 50 \text{ GeV}^2$ and additionally for $s = 500 \text{ GeV}^2$. The plot confirms that the BH amplitude decreases stronger for $s = 50 \text{ GeV}^2$. It shows very clearly the steep dependence on t_d . In addition to that we show in Fig. 4.9 the t_d -dependence for the variables x_B^p and $(t_p - t_{p,0}) / t_p$ appearing in the Bethe–Heitler amplitude as shown in Eq. 3.106. Here we can see that the t_d -dependence of x_B^p is very weak for large s , but is significantly stronger for small s . In the case of $(t_p - t_{p,0}) / t_p$ there is in both cases a clear t_d -dependence, but it is again

Figure 4.7: Distribution of t_d and x_p in electron-deuteron scattering.Figure 4.8: Bethe–Heitler amplitude squared in the relevant range of t_d and q_r for $Q^2 = 2.25 \text{ GeV}^2$, $\psi_{e'} = \psi_n = 0$, $x_B = 0.15$, $x_p = 0.5$ and $t_p = -0.41 \text{ GeV}^2$. The solid line is the t_d -dependence at a center-of-mass energy of $s = 50 \text{ GeV}^2$ and the dashed line of $s = 500 \text{ GeV}^2$.

stronger for $s = 50 \text{ GeV}^2$. Hence the Bethe–Heitler part of the cross section decreases due to the decrease of $(t_p - t_{p,0})/t_p$, which plays an important role due to the factor of $(t_p - t_{p,0})/t_p$ in the Bethe–Heitler amplitude. In contrast to this there is no such term in the DVCS case, hence we get no deviation from electron-proton scattering in the DVCS cross section.

There is a simple connection between t_d and the relative momentum of the deuteron q_r given by

$$t_d = m_d^2 + m_n^2 - \sqrt{4m_d^2m_n^2 + m_d^2q_r^2}. \quad (4.100)$$

Thus we can also consider the squared amplitude of the Bethe–Heitler process depending on the relative momentum q_r instead of t_d . We show the same plots as for t_d also for q_r . The dependence is weak for a higher center-of-mass energy, which is shown in Fig. 4.8 b). We show the Bethe–Heitler term up to $q_r = 0.5$, because we need to keep q_r small compared to m_d . In addition to that we also present the q_r -dependence of x_B^p and $(t_p - t_{p,0})/t_p$ which also shows that the q_r -dependence is stronger for a lower energy as depicted in Fig. 4.10. To keep the off-shell effect small we have to keep the relative momentum of the deuteron small which is

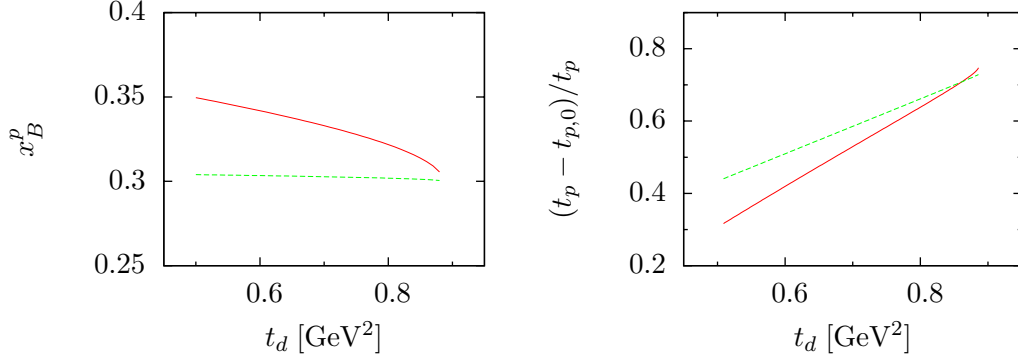


Figure 4.9: Dependence of x_B^p and $t_{p,\min}$ on t_d for $Q^2 = 2.25 \text{ GeV}^2$, $\psi_{e'} = \psi_n = 0$, $x_B = 0.15$, $x_p = 0.5$ and $t_p = -0.41 \text{ GeV}^2$. The solid line is the t_d -dependence at a center-of-mass energy of $s = 50 \text{ GeV}^2$ and the dashed line of $s = 500 \text{ GeV}^2$.

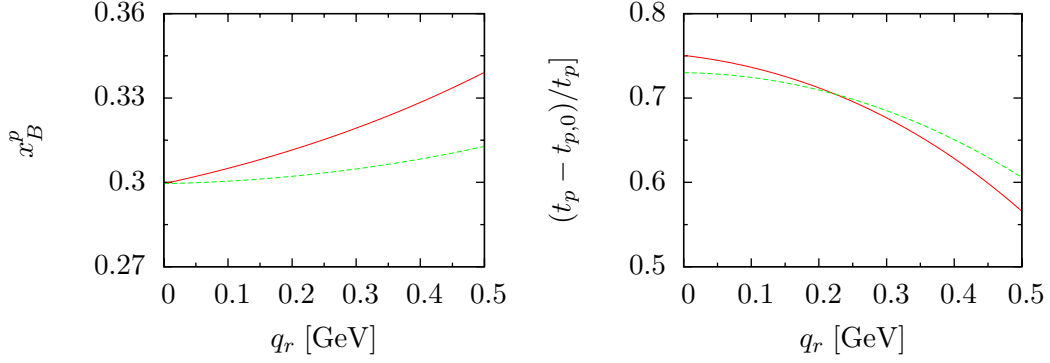


Figure 4.10: Bethe–Heitler amplitude squared and $t_{p,\min}$ in the relevant range of q_d for $Q^2 = 2.25 \text{ GeV}^2$, $\psi_{e'} = \psi_n = 0$, $x_B = 0.15$, $x_p = 0.5$ and $t_p = -0.41 \text{ GeV}^2$. The solid line is the t_d -dependence at a center-of-mass energy of $s = 50 \text{ GeV}^2$ and the dashed line of $s = 500 \text{ GeV}^2$.

equivalent of having t_d close to m_p^2 .

To limit this t_d - or q_r -dependence we replace the deuteron wave function by a narrow gaussian distribution, which should then reduce this effect and lead to bigger values for the Bethe–Heitler contribution to the cross section. By inserting a gaussian distribution, f_{G1} , normalized in the same way as the deuteron wave function

$$f_{G1}(|\vec{p}_{q_r}|^2) = \frac{1}{\sqrt{0.0004431}} \exp\left[\frac{-|\vec{p}_{q_r}|^2}{0.02 \text{ GeV}^2}\right], \quad (4.101)$$

and taking a minimum value for t_d of 0.8 GeV^2 we obtain

	proton	neutron
DVCS	19 pb	8.3 pb
BH	100.8 pb	20.5 pb
BCA	-4.3 pb	-0.7 pb

(T.4.3)

These results are already much closer to those in table T.4.1. Now we reduce the width of the gaussian distribution further

$$f_{G2}(|\vec{p}_{q_r}|^2) = \frac{1}{\sqrt{0.00015666}} \exp\left[\frac{-|\vec{p}_{q_r}|^2}{0.01 \text{ GeV}^2}\right]$$

and get

	proton	neutron
DVCS	19.5 pb	8.2 pb
BH	104.2 pb	22.5 pb
BCA	-4.9 pb	-0.5 pb

(T.4.4)

This shows that DVCS and BH are in good agreement with scattering off a single nucleon. Moreover, the cross section reaches very high numbers equivalent to 300 million events per year which is a very good starting point for an analysis.

When neglecting off-shell effects we have the result that the electron-deuteron scattering is approximately equal to the sum of electron-proton and electron-neutron scattering. Although we have seen that the off-shell effects are not negligible in the Bethe–Heitler case they do not effect DVCS. Thus, regarding the GPDs, we can still treat the off-shell nucleon inside the deuteron as on-shell and adopt the on-shell GPDs. Thus we have a process where we can test the GPDs of the neutron. As in the case of $ep \rightarrow e' \pi \gamma n$ we can now implement different models for the GPDs and compare our results to experimental data, when available, to see the liability of the models. We have seen how significantly the Bethe–Heitler cross section depends on the off-shellness, hence we have to keep the virtuality of the proton (or neutron) very small.

HERMES offers another possibility to measure electron-deuteron scattering. Data are already taken but not yet analyzed. Therefore the computation of the cross section can in the near future also be made for the HERMES experiment.

Chapter 5

Summary and outlook

In this work we have investigated two exclusive processes, $ep \rightarrow e' \pi \gamma n$ and $ed \rightarrow epn \gamma$. They give us the possibility to access GPDs, which are important objects to further reveal the inner structure of hadrons.

After an overview of the general framework we introduced GPDs. We then showed how GPDs are related to the well known form factors and PDFs. For our studies we implemented models for GPDs, in particular for the pion and the nucleons. At the end of Chapter 2 we examined different processes giving the opportunity to access GPDs. We summarized the different quark and flavor combinations of GPDs occurring in each process and showed how they can be related using isospin symmetry.

In Chapter 3 we analyzed the exclusive process $ep \rightarrow e' \pi \gamma n$. We introduced the kinematics and derived the differential cross section in terms of a pion GPD convoluted with the hard scattering kernel. Even though it is non-trivial to extract the GPDs from data, relevant experiments are performed at DESY and JLab. We numerically computed cross sections and asymmetries using four different models and found that the asymmetries display sizable differences for the distinct models. For phenomenological applications, it is important to assess to which extent the cross section and asymmetry measurements are influenced by the design of an experiment, in particular its luminosity, and the imposed kinematical constraints.

The last section in Chapter 3 focused on the result of the cross section of this exclusive electron-proton scattering process, where we have taken into account the two different experiments, HERMES at DESY and CLAS at JLab. For HERMES the luminosity is low and the detector is placed behind the colliding point. Thus the particles that should be detected must be located in a small range of forward angles and have energies greater than a threshold energy. Slow pions are especially difficult to detect. Implementing these constraints we obtain a very small event rate per year. It would thus not be possible to reach the statistical accuracy required for the measurements. In contrast to that, the CLAS detector at JLab is a 4π detector and covers the region around the target, thus not many events are lost. Although the beam energy will only be 11 GeV after the planned JLab upgrade, the high luminosity makes it possible to detect several 10^4 events per year. Here we studied in detail how the cross section changed when varying the kinematical constraints and to what extent the results depend on the implemented models for the GPD. The values for the cross sections and the corresponding event rates show that it is possible to measure this cross section at CLAS. In addition to the cross section we have computed weighted asymmetries. These are easier to measure because acceptance and efficiency uncertainties of the detector cancel to a large

extent. We got reasonable values for both, the beam polarization and beam charge asymmetries. Experimental results of electroproduction of photons off protons at HERMES show that the beam polarization is larger than the beam charge asymmetry. The results we obtained for BCA and BPA show the same behavior. Our work clearly shows that this measurement can significantly help to constrain the GPD of the pion, which gives a unique insight into the structure of the pion.

In Chapter 4 we investigated the process $ed \rightarrow ep\gamma n$ after a brief discussion of the deuteron. We showed analytically how to derive the differential cross section by implementing the nucleon form factors, the nucleon GPDs and the deuteron wave function. This process was studied for the CLAS detector at JLab. We computed the total cross section which is supposed to be approximately equal to the sum of the processes $ep \rightarrow e'p'\gamma$ and $en \rightarrow e'n'\gamma$. The deuteron target can be used as a quasi-free neutron target. There is an obvious interest in neutron DVCS because it allows a flavor decomposition of GPDs. Measurements are mandatory since neutrons are more sensitive to the d quarks than protons.

Our results show that off-shell effects play an important role for the Bethe–Heitler cross section. Due to a kinematic factor in the Bethe–Heitler amplitude, its cross section is significantly suppressed. We found that this effect can be limited by replacing the deuteron wave function with a narrow gaussian distribution. In that case the result was then approximately equal to the sum of electron-proton and electron-neutron scattering. But we also saw, that the off-shell effects influence only the Bethe–Heitler process and not DVCS. Therefore it is still possible to use the on-shell GPDs for the off-shell nucleons inside the deuteron. Electron-deuteron scattering provides a substantive way to investigate the GPDs of the neutron, which is of special interest for the very reason that the neutron is an instable particle. It leads to a better comprehension of the nucleon properties as for example the composition of the nucleon spin.

Using the results of Chapter 4 it is possible to implement further models for nucleon GPDs. Then these models can be elaborated by comparing to future data. Besides the CLAS experiment, we will focus our attention in the near future on the HERMES experiment. At HERMES data of electron-deuteron scattering were already taken. Therefore, the calculation will be made for the HERMES experiment as well. Once the data are analyzed a comparison with our calculations can be made and the implemented models can be improved.

Appendix A

Light-cone coordinates

To describe deep inelastic processes it is useful to introduce light-cone coordinates. The coordinate system is chosen in a way, that the momenta of the target $(p_p)_\mu$ and of the hard probe q_μ possess only non vanishing components in time and in one space dimension, usually the z -axis. It is useful to define two light-like four-vectors

$$n_+ = \frac{1}{\sqrt{2}} \begin{pmatrix} 1 \\ 0 \\ 0 \\ 1 \end{pmatrix}, \quad n_- = \frac{1}{\sqrt{2}} \begin{pmatrix} 1 \\ 0 \\ 0 \\ -1 \end{pmatrix}, \quad (\text{A.1})$$

with $(n_+)^2 = (n_-)^2 = 0$, and $n_+ \cdot n_- = 1$. These vectors are unit vectors on the light-cone. In general every four-vector can be decomposed according to

$$a_\mu = (a \cdot n_+)(n_-)_\mu + (a \cdot n_-)(n_+)_\mu + (a_\perp)_\mu. \quad (\text{A.2})$$

Light-cone vector components are defined through

$$a^\mu = [a^+, a^-, \vec{a}_T] = \left[\frac{a^0 + a^3}{\sqrt{2}}, \frac{a^0 - a^3}{\sqrt{2}}, a^1, a^2 \right], \quad (\text{A.3})$$

where a^1 and a^2 are the transverse components. Furthermore, it is valid in each frame of reference, that $a^+ = a \cdot n_-$, $a^- = a \cdot n_+$.

Appendix B

Spherical harmonics

Analytic expressions for the spherical harmonics needed in Chapter 4 are

$$Y_{00}(\hat{q}) = \frac{1}{\sqrt{4\pi}}, \quad (\text{B.1})$$

$$Y_{20}(\hat{q}) = \sqrt{\frac{5}{16\pi}} (3 \cos^2 \theta - 1), \quad (\text{B.2})$$

$$Y_{21}(\hat{q}) = -\sqrt{\frac{15}{8\pi}} \cos \theta \sin \theta e^{i\phi}, \quad (\text{B.3})$$

$$Y_{22}(\hat{q}) = \sqrt{\frac{15}{32\pi}} \sin 2\phi e^{i2\phi}. \quad (\text{B.4})$$

To obtain those functions including negative quantum number m the simple relation

$$Y_{l,-m} = (-)^m Y_{l,m}^* \quad (\text{B.5})$$

can be used.

Appendix C

Details for PDF fits

The partonic parametrization of the valence quarks from Glück, Reya and Schienbein[107] include the parameters

$$\begin{aligned} N &= 1.21 + 0.487s + 0.009s^2, \\ \alpha &= 0.517 - 0.020s, \\ A &= -0.037 - 0.578s, \\ B &= 0.241 + .0251s, \\ D &= 0.383 + 0.624s \end{aligned} \tag{C.1}$$

and for sea-quarks

$$\begin{aligned} \alpha &= 1.147, \\ a &= 0.309 - 0.134\sqrt{s}, \\ A &= 0.219 - 0.054s, \\ C &= 1.100 - 0.452s, \\ E &= 4.521 + 1.583s, \\ \beta &= 1.241, \\ b &= 0.893 - 0.264\sqrt{s}, \\ B &= -0.593 + 0.240s, \\ D &= 3.526 + 0.491, \\ E' &= 3.102. \end{aligned} \tag{C.2}$$

Free parameters for the unpolarized PDFs used for the numeric calculations from [147] we needed for the unpolarized PDF $q(x)$ using the following parameters:

	A_0	A_1	A_2	A_3	A_4	A_5
u_v	1.7199	0.5526	2.9009	-2.3502	1.6123	1.5917
d_v	1.4473	0.6160	4.9670	0.8408	0.4031	3.0000
$\bar{u} + \bar{d}$	0.0616	-0.2990	7.7170	-0.5283	4.7539	0.6137
\bar{d}/\bar{u}	33657.8	4.2676	14.8586	17.0000	8.6409	-

(C.3)

and for the unpolarized PDF $e(x)$, taken from [148] the parameters are:

	β_q	C_q	D_q	α
u	3.99 ± 0.22	1.22 GeV^{-2}	$(0.38 \pm 0.11) \text{ GeV}^{-2}$	0.55
d	$\beta_u + 1.6$	2.59 GeV^{-2}	$-(0.75 \pm 0.05) \text{ GeV}^{-2}$	0.55

(C.4)

Free parameters for the polarized PDFs used for the numeric calculations from [149] are:

	η_i	a_i	b_i	γ_i
u_v	0.926	0.197	2.403	21.34
d_v	-0.341	0.19	3.24	30.8
\bar{q}	-0.353	0.367	8.51	0

(C.5)

Bibliography

- [1] E. Rutherford *Phil. Mag.* **21** (1911) 669.
- [2] E. Rutherford *Phil. Mag.* **37** (1919) 581.
- [3] J. Chadwick and M. Goldhaber, “A nuclear photo-effect – disintegration of the dipion by gamma rays,” *Nature* **134** (1934) 237–238.
- [4] C. D. Anderson, “The positive electron,” *Phys. Rev.* **43** (Mar, 1933) 491–494.
- [5] S. H. Neddermeyer and C. D. Anderson, “Note on the nature of cosmic-ray particles,” *Phys. Rev.* **51** (May, 1937) 884–886.
- [6] J. C. Street and E. C. Stevenson, “New evidence for the existence of a particle of mass intermediate between the proton and electron,” *Phys. Rev.* **52** (Nov, 1937) 1003–1004.
- [7] C. M. G. Lattes, H. Muirhead, G. P. S. Occhialini, and C. F. Powell, “Processes involving charged mesons,” *Nature* **159** (1947) 694–697.
- [8] G. D. Rochester and C. C. Butler, “Evidence for the existence of new unstable elementary particles,” *Nature* **160** (1947) 855–857.
- [9] R. P. Feynman, “Photon-hadron interactions,”. Reading 1972, 282p.
- [10] M. Fritzsche, H. Gell-Mann and L. H. *Phys. Lett.* **B47** (1973) 365.
- [11] Y. L. Dokshitzer, D. Diakonov, and S. I. Troian, “Hard processes in quantum chromodynamics,” *Phys. Rept.* **58** (1980) 269–395.
- [12] A. H. Müller, “Perturbative QCD at high-energies,” *Phys. Rept.* **73** (1981) 237.
- [13] H. D. Politzer, “Asymptotic freedom: An approach to strong interactions,” *Phys. Rept.* **14** (1974) 129–180.
- [14] M. Gell-Mann and Y. Neeman, “Current-generated algebras,” *Annals Phys.* **30** (1964) 360–369.
- [15] Y. Ne’eman, “Derivation of strong interactions from a gauge invariance,” *Nucl. Phys.* **26** (1961) 222–229.
- [16] V. E. Barnes *et al.*, “Observation of a hyperon with strangeness minus three,” *Phys. Rev. Lett.* **12** (Feb, 1964) 204–206.

- [17] O. Nachtmann, *Elementarteilchenphysik, Phänomene und Konzepte*. Vieweg, Braunschweig, 1986.
- [18] J. J. Aubert *et al.*, “Experimental observation of a heavy particle j ,” *Phys. Rev. Lett.* **33** (Dec, 1974) 1404–1406.
- [19] S. L. Glashow, J. Iliopoulos, and L. Maiani, “Weak interactions with lepton-hadron symmetry,” *Phys. Rev. D* **2** (Oct, 1970) 1285–1292.
- [20] S. W. Herb *et al.*, “Observation of a dimuon resonance at 9.5 GeV in 400-GeV proton-nucleus collisions,”.
- [21] **CDF** Collaboration, F. Abe *et al.*, “Observation of top quark production in $\bar{p}p$ collisions,” *Phys. Rev. Lett.* **74** (1995) 2626–2631, [hep-ex/9503002](#).
- [22] D. J. Gross and F. Wilczek, “Ultraviolet behavior of non-abelian gauge theories,” *Phys. Rev. Lett.* **30** (1973) 1343–1346.
- [23] H. D. Politzer, “Reliable perturbative results for strong interactions?,” *Phys. Rev. Lett.* **30** (1973) 1346–1349.
- [24] S. D. Bass and A. De Roeck, “The spin structure of the proton and polarized collider physics,” *Nucl. Phys. Proc. Suppl.* **105** (2002) 1–27, [hep-ph/0111377](#).
- [25] M. Klein, “Structure functions in deep inelastic lepton nucleon scattering,” [hep-ex/0001059](#).
- [26] J. D. Bjorken and E. A. Paschos, “Inelastic electron proton and γ proton scattering, and the structure of the nucleon,” *Phys. Rev.* **185** (1969) 1975–1982.
- [27] J. D. Bjorken, “Asymptotic sum rules at infinite momentum,” *Phys. Rev.* **179** (1969) 1547–1553.
- [28] W. K. H. Panofsky, “Electromagnetic interactions: Low q^2 electrodynamics: Elastic and inelastic electron (and muon) scattering,”. Presented at 14th Int. Conf. on High Energy Physics, Vienna, Aug 1968.
- [29] J. C. Collins and A. Freund, “Proof of factorization for deeply virtual compton scattering in QCD,” *Phys. Rev.* **D59** (1999) 074009, [hep-ph/9801262](#).
- [30] J. C. Collins, L. Frankfurt, and M. Strikman, “Factorization for hard exclusive electroproduction of mesons in QCD,” *Phys. Rev.* **D56** (1997) 2982–3006, [hep-ph/9611433](#).
- [31] J. C. Collins, “Factorization for hard exclusive electroproduction,” [hep-ph/9907513](#).
- [32] X.-D. Ji, “Deeply-virtual compton scattering,” *Phys. Rev.* **D55** (1997) 7114–7125, [hep-ph/9609381](#).
- [33] D. Müller, D. Robaschik, B. Geyer, F. M. Dittes, and J. Horejsi, “Wave functions, evolution equations and evolution kernels from light-ray operators of QCD,” *Fortschr. Phys.* **42** (1994) 101, [hep-ph/9812448](#).

- [34] V. N. Gribov and L. N. Lipatov, "Deep inelastic e p scattering in perturbation theory," *Sov. J. Nucl. Phys.* **15** (1972) 438–450.
- [35] A. P. Bukhvostov, L. N. Lipatov, and N. P. Popov, "Parton distribution functions in perturbation theory," *Yad. Fiz.* **20** (1974) 532–548.
- [36] L. N. Lipatov, "The parton model and perturbation theory," *Sov. J. Nucl. Phys.* **20** (1975) 94–102.
- [37] G. Altarelli and G. Parisi, "Asymptotic freedom in parton language," *Nucl. Phys.* **B126** (1977) 298.
- [38] Y. L. Dokshitzer, "Calculation of the structure functions for deep inelastic scattering and e+ e- annihilation by perturbation theory in quantum chromodynamics. (in russian)," *Sov. Phys. JETP* **46** (1977) 641–653.
- [39] A. V. Efremov and A. V. Radyushkin, "Factorization and asymptotical behavior of pion form-factor in QCD," *Phys. Lett.* **B94** (1980) 245–250.
- [40] G. R. Farrar and D. R. Jackson, "The pion form-factor," *Phys. Rev. Lett.* **43** (1979) 246.
- [41] G. P. Lepage and S. J. Brodsky, "Exclusive processes in perturbative quantum chromodynamics," *Phys. Rev.* **D22** (1980) 2157.
- [42] X.-D. Ji, "Gauge invariant decomposition of nucleon spin," *Phys. Rev. Lett.* **78** (1997) 610–613, [hep-ph/9603249](#).
- [43] A. V. Radyushkin, "Scaling limit of deeply virtual compton scattering," *Phys. Lett.* **B380** (1996) 417–425, [hep-ph/9604317](#).
- [44] M. Burkardt, "Impact parameter dependent parton distributions and off- forward parton distributions for $\zeta \rightarrow 0$," *Phys. Rev.* **D62** (2000) 071503, [hep-ph/0005108](#).
- [45] F. Halzen and A. D. Martin, *Quarks and leptons : An introductory course in modern particle physics*. Wiley, New York, 1984.
- [46] C. F. Perdrisat, V. Punjabi, and M. Vanderhaeghen, "Nucleon electromagnetic form factors," [hep-ph/0612014](#).
- [47] S. Galster *et al.*, "Elastic electron - deuteron scattering and the electric neutron form-factor at four momentum transfers $5\text{-fm}^{-2} < q^2 < 14\text{-fm}^{-2}$," *Nucl. Phys.* **B32** (1971) 221–237.
- [48] S. Platchkov *et al.*, "Deuteron $a(Q^2)$ structure function and the neutron electric form-factor," *Nucl. Phys.* **A510** (1990) 740–758.
- [49] L. N. Hand, D. G. Miller, and R. Wilson, "Electric and magnetic form factors of the nucleon," *Rev. Mod. Phys.* **35** (Apr, 1963) 335–349.
- [50] G. Hohler *et al.*, "Analysis of electromagnetic nucleon form-factors," *Nucl. Phys.* **B114** (1976) 505.

- [51] K. M. Hanson, J. R. Dunning, M. Goitein, T. Kirk, L. E. Price, and R. Wilson, "Large-angle quasielastic electron-deuteron scattering," *Phys. Rev. D* **8** (Aug, 1973) 753–778.
- [52] J. Litt *et al.*, "Measurement of the ratio of the proton form-factors, $g(e) / g(m)$, at high momentum transfers and the question of scaling," *Phys. Lett.* **B31** (1970) 40–44.
- [53] C. Berger, V. Burkert, G. Knop, B. Langenbeck, and K. Rith, "Electromagnetic form-factors of the proton at squared four momentum transfers between 10-fm^{-2} and 50 fm^{-2} ," *Phys. Lett.* **B35** (1971) 87.
- [54] W. Bartel *et al.*, "Measurement of proton and neutron electromagnetic form-factors at squared four momentum transfers up to $3\text{- GeV}/c^2$," *Nucl. Phys.* **B58** (1973) 429–475.
- [55] R. C. Walker *et al.*, "Measurements of the proton elastic form factors for $1 \leq q^2 \leq 3$ $(\text{gev}/c)^2$ at slac," *Phys. Rev. D* **49** (Jun, 1994) 5671–5689.
- [56] I. A. Qattan *et al.*, "Precision rosenbluth measurement of the proton elastic form factors," *Phys. Rev. Lett.* **94** (2005) 142301, [nucl-ex/0410010](#).
- [57] L. Andivahis *et al.*, "Measurements of the electric and magnetic form factors of the proton from $q^2=1.75$ to 8.83 $(\text{gev}/c)^2$," *Phys. Rev. D* **50** (Nov, 1994) 5491–5517.
- [58] J. J. Murphy, Y. M. Shin, and D. M. Skopik, "Proton form factor from 0.15 to 0.79 fm^{-2} ," *Phys. Rev. C* **9** (Jun, 1974) 2125–2129.
- [59] R. G. Arnold *et al.*, "Measurement of elastic electron scattering from the proton at high momentum transfer," *Phys. Rev. Lett.* **57** (Jul, 1986) 174–177.
- [60] R. C. Walker *et al.*, "Measurement of the proton elastic form-factors for $Q^2 = 1\text{-GeV}/c^2 - 3\text{-GeV}/c^2$," *Phys. Lett.* **B224** (1989) 353–353.
- [61] S. Rock *et al.*, "Measurement of elastic electron-neutron scattering and inelastic electron-deuteron scattering cross sections at high momentum transfer," *Phys. Rev. D* **46** (Jul, 1992) 24–44.
- [62] A. Lung *et al.*, "Measurements of the electric and magnetic form factors of the neutron from $q^2=1.75$ to 4.00 $(\text{gev}/c)^2$," *Phys. Rev. Lett.* **70** (Feb, 1993) 718–721.
- [63] H. Anklin *et al.*, "Precision measurement of the neutron magnetic form-factor," *Phys. Lett.* **B336** (1994) 313–318.
- [64] E. E. W. Bruins *et al.*, "Measurement of the neutron magnetic form factor," *Phys. Rev. Lett.* **75** (Jul, 1995) 21–24.
- [65] H. Anklin *et al.*, "Precise measurements of the neutron magnetic form factor," *Phys. Lett.* **B428** (1998) 248–253.
- [66] G. Kubon *et al.*, "Precise neutron magnetic form factors," *Phys. Lett.* **B524** (2002) 26–32, [nucl-ex/0107016](#).

- [67] **CLAS** Collaboration, W. K. Brooks and J. D. Lachniet, “Precise determination of the neutron magnetic form factor to higher Q^2 ,” *Nucl. Phys.* **A755** (2005) 261–264, [nucl-ex/0504028](#).
- [68] P. Mulders, “Transverse momentum dependence in structure functions in hard scattering processes,” (private notes, Amsterdam, 2000).
- [69] P. J. Mulders and R. D. Tangerman, “The complete tree-level result up to order $1/Q$ for polarized deep-inelastic lepton production,” *Nucl. Phys.* **B461** (1996) 197–237, [hep-ph/9510301](#).
- [70] R. L. Jaffe and X.-D. Ji, “Chiral odd parton distributions and polarized Drell-Yan,” *Phys. Rev. Lett.* **67** (1991) 552–555.
- [71] R. L. Jaffe and X.-D. Ji, “Chiral odd parton distributions and Drell-Yan processes,” *Nucl. Phys.* **B375** (1992) 527–560.
- [72] J. C. Collins, D. E. Soper, and G. Sterman, “Factorization of hard processes in QCD,” *Adv. Ser. Direct. High Energy Phys.* **5** (1988) 1–91, [hep-ph/0409313](#).
- [73] R. L. Jaffe, “Spin, twist and hadron structure in deep inelastic processes,” [hep-ph/9602236](#).
- [74] K. Goeke, M. V. Polyakov, and M. Vanderhaeghen, “Hard exclusive reactions and the structure of hadrons,” *Prog. Part. Nucl. Phys.* **47** (2001) 401–515, [hep-ph/0106012](#).
- [75] **H1** Collaboration, C. Adloff *et al.*, “Measurement of deeply virtual compton scattering at HERA,” *Phys. Lett.* **B517** (2001) 47–58, [hep-ex/0107005](#).
- [76] **HERMES** Collaboration, A. Airapetian *et al.*, “The beam-charge azimuthal asymmetry and deeply virtual compton scattering,” *Phys. Rev.* **D75** (2007) 011103, [hep-ex/0605108](#).
- [77] **HERMES** Collaboration, F. Ellinghaus, “Beam-charge asymmetry associated with DVCS at HERMES,” *Nucl. Phys.* **A711** (2002) 171–174, [hep-ex/0207029](#).
- [78] S. Stepanyan *et al.*, “Observation of exclusive deeply virtual compton scattering in polarized electron beam asymmetry measurements,” *Phys. Rev. Lett.* **87** (Oct, 2001) 182002.
- [79] M. Diehl, “Generalized parton distributions,” *Phys. Rept.* **388** (2003) 41–277, [hep-ph/0307382](#).
- [80] A. V. Belitsky and A. V. Radyushkin, “Unraveling hadron structure with generalized parton distributions,” [hep-ph/0504030](#).
- [81] M. Burkardt, “Impact parameter space interpretation for generalized parton distributions,” *Int. J. Mod. Phys.* **A18** (2003) 173–208, [hep-ph/0207047](#).
- [82] A. V. Radyushkin, “Generalized parton distributions,” [hep-ph/0101225](#).
- [83] M. V. Polyakov and C. Weiss, “Skewed and double distributions in pion and nucleon,” *Phys. Rev.* **D60** (1999) 114017, [hep-ph/9902451](#).

- [84] I. V. Musatov and A. V. Radyushkin, “Evolution and models for skewed parton distributions,” *Phys. Rev.* **D61** (2000) 074027, [hep-ph/9905376](#).
- [85] A. H. Compton, “The spectrum of scattered x-rays,” *Phys. Rev.* **22** (Nov, 1923) 409–413.
- [86] X.-D. Ji and J. Osborne, “One-loop corrections and all order factorization in deeply virtual compton scattering,” *Phys. Rev.* **D58** (1998) 094018, [hep-ph/9801260](#).
- [87] A. V. Radyushkin, “Nonforward parton densities and soft mechanism for form factors and wide-angle compton scattering in QCD,” *Phys. Rev.* **D58** (1998) 114008, [hep-ph/9803316](#).
- [88] A. D. Martin and T. D. Spearman, *Elementary particle theory*. North-Holland, 1970, Amsterdam.
- [89] I. V. Anikin, A. E. Dorokhov, A. E. Maximov, L. Tomio, and V. Vento, “Off-diagonal quark distribution functions of the pion within an effective single instanton approximation,” [hep-ph/9905332](#).
- [90] W. Broniowski and E. Ruiz Arriola, “Impact-parameter dependence of the generalized parton distribution of the pion in chiral quark models,” *Phys. Lett.* **B574** (2003) 57–64, [hep-ph/0307198](#).
- [91] L. Theussl, S. Noguera, and V. Vento, “Generalized parton distributions of the pion in a bethe- salpeter approach,” *Eur. Phys. J.* **A20** (2004) 483–498, [nucl-th/0211036](#).
- [92] J. Fleischer, A. Leike, T. Riemann, and A. Werthenbach, “Electroweak one-loop corrections for $e^+ e^-$ annihilation into t anti- t including hard bremsstrahlung,” *Eur. Phys. J.* **C31** (2003) 37–56, [hep-ph/0302259](#).
- [93] A. V. Belitsky, D. Müller, A. Kirchner, and A. Schäfer, “Twist-three analysis of photon electroproduction off pion,” *Phys. Rev.* **D64** (2001) 116002, [hep-ph/0011314](#).
- [94] A. V. Belitsky, D. Müller, L. Niedermeier, and A. Schäfer, “Leading twist asymmetries in deeply virtual compton scattering,” *Nucl. Phys.* **B593** (2001) 289–310, [hep-ph/0004059](#).
- [95] A. V. Belitsky, D. Müller, and A. Kirchner, “Theory of deeply virtual compton scattering on the nucleon,” *Nucl. Phys.* **B629** (2002) 323–392, [hep-ph/0112108](#).
- [96] B. Pire and L. Szymanowski, “Hadron annihilation into two photons and backward VCS in the scaling regime of QCD,” *Phys. Rev.* **D71** (2005) 111501, [hep-ph/0411387](#).
- [97] B. Pire and L. Szymanowski, “QCD analysis of $\bar{p}N \rightarrow \gamma^* \pi$ in the scaling limit,” *Phys. Lett.* **B622** (2005) 83–92, [hep-ph/0504255](#).
- [98] J. P. Lansberg, B. Pire, and L. Szymanowski, “Hard exclusive electroproduction of a pion in the backward region,” [hep-ph/0701125](#).
- [99] W. Broniowski and E. R. Arriola, “Pion photon transition distribution amplitudes in the spectral quark model,” [hep-ph/0701243](#).

- [100] J. P. Lansberg, B. Pire, and L. Szymanowski, “Exclusive meson pair production in $\gamma^*\gamma$ scattering at small momentum transfer,” *Physical Review D (Particles and Fields)* **73** (2006), no. 7, 074014.
- [101] J. P. Lansberg, B. Pire, and L. Szymanowski, “Transition distribution amplitudes,” arXiv:0709.2567 [hep-ph].
- [102] N. Kivel, M. V. Polyakov, and M. Vanderhaeghen, “DVCS on the nucleon: Study of the twist-3 effects,” *Phys. Rev.* **D63** (2001) 114014, hep-ph/0012136.
- [103] M. Vanderhaeghen, P. A. M. Guichon, and M. Guidal, “Hard electroproduction of photons and mesons on the nucleon,” *Phys. Rev. Lett.* **80** (Jun, 1998) 5064–5067.
- [104] M. Diehl, “Generalized parton distributions from form factors,” *Nucl. Phys. Proc. Suppl.* **161** (2006) 49–58, hep-ph/0510221.
- [105] W. Koepf, L. L. Frankfurt, and M. Strikman, “The nucleon’s virtual meson cloud and deep inelastic lepton scattering,” *Phys. Rev.* **D53** (1996) 2586–2598, hep-ph/9507218.
- [106] M. Diehl, W. Kugler, A. Schäfer, and C. Weiss, “Exclusive channels in semi-inclusive production of pions and kaons,” *Phys. Rev.* **D72** (2005) 034034, hep-ph/0506171.
- [107] M. Glück, E. Reya, and I. Schienbein, “Pionic parton distributions revisited,” *Eur. Phys. J.* **C10** (1999) 313–317, hep-ph/9903288.
- [108] P. J. Sutton, A. D. Martin, R. G. Roberts, and W. J. Stirling, “Parton distributions for the pion extracted from Drell-Yan and prompt photon experiments,” *Phys. Rev.* **D45** (1992) 2349–2359.
- [109] **The Jefferson Lab F(π) Collaboration**, J. Volmer *et al.*, “New results for the charged pion electromagnetic form-factor,” *Phys. Rev. Lett.* **86** (2001) 1713–1716, nucl-ex/0010009.
- [110] **QCDSF/UKQCD Collaboration**, D. Brömmel *et al.*, “The pion form factor from lattice QCD with two dynamical flavours,” *Eur. Phys. J.* **C51** (2007) 335–345, hep-lat/0608021.
- [111] P. A. Boyle, J. M. Flynn, A. Jüttner, C. T. Sachrajda, and J. M. Zanotti, “Hadronic form factors in lattice QCD at small and vanishing momentum transfer,” *JHEP* **05** (2007) 016, hep-lat/0703005.
- [112] **JLQCD Collaboration**, S. Hashimoto *et al.*, “Pion form factors in two-flavor QCD,” *PoS LAT2005* (2006) 336, hep-lat/0510085.
- [113] **HERMES Collaboration**, A. Airapetian *et al.*, “Measurement of the beam spin azimuthal asymmetry associated with deeply-virtual compton scattering,” *Phys. Rev. Lett.* **87** (2001) 182001, hep-ex/0106068.
- [114] **CLAS Collaboration**, S. Stepanyan *et al.*, “First observation of exclusive deeply virtual compton scattering in polarized electron beam asymmetry measurements,” *Phys. Rev. Lett.* **87** (2001) 182002, hep-ex/0107043.

- [115] N. Kivel, M. V. Polyakov, and M. Vanderhaeghen, “Deeply virtual compton scattering on the nucleon: Study of the twist-3 effects,” *Phys. Rev. D* **63** (May, 2001) 114014.
- [116] R. T. Birge and D. H. Menzel, “The relative abundance of the oxygen isotopes, and the basis of the atomic weight system,” *Phys. Rev.* **37** (Jun, 1931) 1669–1671.
- [117] H. C. Urey, F. G. Brickwedde, and G. M. Murphy, “A hydrogen isotope of mass 2,” *Phys. Rev.* **39** (Jan, 1932) 164–165.
- [118] W. Bleakney and A. J. Gould, “The relative abundance of hydrogen isotopes,” *Phys. Rev.* **44** (Aug, 1933) 265–268.
- [119] G. N. Lewis, M. S. Livingston, and E. O. Lawrence, “The emission of α -particles from various targets bombarded by deuterons of high speed,” *Phys. Rev.* **44** (Jul, 1933) 55–56.
- [120] E. Fermi, “An attempt of a theory of beta radiation,” *Z. Phys.* **88** (1934) 161–177.
- [121] E. Fermi, “Trends to a theory of beta radiation. (in italian),” *Nuovo Cim.* **11** (1934) 1–19.
- [122] Kessler *et al.*, “The deuteron binding energy and the neutron mass,” *Phys. Lett* **255** (1999) 221.
- [123] R. Schiavilla *et al.*, “Weak capture of protons by protons,” *Phys. Rev.* **C58** (1998) 1263, [nucl-th/9808010](#).
- [124] G. M. Murphy and H. Johnston, “The nuclear spin of deuterium,” *Phys. Rev.* **46** (Jul, 1934) 95–98.
- [125] I. I. Rabi, J. M. B. Kellogg, and J. R. Zacharias, “The magnetic moment of the deuteron,” *Phys. Rev.* **46** (Aug, 1934) 163–165.
- [126] J. M. B. Kellogg, I. I. Rabi, N. F. Ramsey, and J. R. Zacharias, “An electrical quadrupole moment of the deuteron,” *Phys. Rev.* **55** (Feb, 1939) 318–319.
- [127] K. Krane, *Introductory Nuclear Physics*. John Wiley, 1987.
- [128] F. Cano and B. Pire, “Deeply virtual compton scattering on the deuteron,” *Nucl. Phys.* **A711** (2002) 133–138, [hep-ph/0206215](#).
- [129] F. Cano and B. Pire, “Deeply virtual compton scattering on spin-1 nuclei,” *Nucl. Phys.* **A721** (2003) 789–792, [hep-ph/0211444](#).
- [130] F. Cano and B. Pire, “Deep electroproduction of photons and mesons on the deuteron,” *Eur. Phys. J.* **A19** (2004) 423–438, [hep-ph/0307231](#).
- [131] E. R. Berger, F. Cano, M. Diehl, and B. Pire, “Generalized parton distributions in the deuteron,” *Phys. Rev. Lett.* **87** (2001) 142302, [hep-ph/0106192](#).
- [132] A. Kirchner and D. Müller, “Predictions for deeply virtual compton scattering on a spin-one target,” [hep-ph/0202279](#).
- [133] A. Kirchner and D. Müller, “Deeply virtual compton scattering off nuclei,” *Eur. Phys. J.* **C32** (2003) 347–375, [hep-ph/0302007](#).

- [134] V. Guzey and M. Strikman, “DVCS on spinless nuclear targets in impulse approximation,” *Phys. Rev.* **C68** (2003) 015204, [hep-ph/0301216](#).
- [135] **HERMES** Collaboration, A. Airapetian *et al.*, “Double-spin asymmetries in the cross section of ρ_0 and phi production at intermediate energies,” *Eur. Phys. J.* **C29** (2003) 171–179, [hep-ex/0302012](#).
- [136] **HERMES** Collaboration, P. di Nezza and R. Fabbri, “Hard exclusive electroproduction of two pions off proton and deuteron at HERMES,” *AIP Conf. Proc.* **675** (2003) 313–317, [hep-ex/0211008](#).
- [137] R. G. Arnold, C. E. Carlson, and F. Gross, “Polarization transfer in elastic electron scattering from nucleons and deuterons,” *Phys. Rev. C* **23** (Jan, 1981) 363–374.
- [138] M. Garcon and J. W. Van Orden, “The deuteron: Structure and form factors,” *Adv. Nucl. Phys.* **26** (2001) 293, [nucl-th/0102049](#).
- [139] M. Diehl, “Generalized parton distributions with helicity flip,” *Eur. Phys. J.* **C19** (2001) 485–492, [hep-ph/0101335](#).
- [140] M. I. Haftel and F. Tabakin, “Nuclear saturation and the smoothness of nucleon-nucleon potentials,” *Nucl. Phys.* **A158** (1970) 1.
- [141] R. Machleidt, F. Sammarruca, and Y. Song, “The non-local nature of the nuclear force and its impact on nuclear structure,” *Phys. Rev.* **C53** (1996) 1483–1487, [nucl-th/9510023](#).
- [142] V. G. J. Stoks, R. A. M. Klomp, M. C. M. Rentmeester, and J. J. de Swart, “Partial-wave analysis of all nucleon-nucleon scattering data below 350 MeV,” *Phys. Rev. C* **48** (Aug, 1993) 792–815.
- [143] V. G. J. Stoks, R. A. M. Klomp, C. P. F. Terheggen, and J. J. de Swart, “Construction of high-quality nn potential models,” *Phys. Rev. C* **49** (Jun, 1994) 2950–2962.
- [144] R. B. Wiringa, V. G. J. Stoks, and R. Schiavilla, “An accurate nucleon-nucleon potential with charge independence breaking,” *Phys. Rev.* **C51** (1995) 38–51, [nucl-th/9408016](#).
- [145] J. Carlson and R. Schiavilla, “Structure and dynamics of few-nucleon systems,” *Rev. Mod. Phys.* **70** (1998) 743–842.
- [146] I. Fachruddin, C. Elster, and W. Gloeckle, “New forms of deuteron equations and wave function representations,” *Phys. Rev.* **C63** (2001) 054003, [nucl-th/0101009](#).
- [147] J. Pumplin *et al.*, “New generation of parton distributions with uncertainties from global QCD analysis,” *JHEP* **07** (2002) 012, [hep-ph/0201195](#).
- [148] M. Diehl, T. Feldmann, R. Jakob, and P. Kroll, “Generalized parton distributions from nucleon form factor data,” *Eur. Phys. J.* **C39** (2005) 1–39, [hep-ph/0408173](#).
- [149] J. Blumlein and H. Bottcher, “QCD analysis of polarized deep inelastic scattering data and parton distributions,” *Nucl. Phys.* **B636** (2002) 225–263, [hep-ph/0203155](#).

- [150] J. Blumlein and H. Bottcher, “QCD analysis of polarized scattering data and new polarized parton distributions,” *Acta Phys. Polon.* **B33** (2002) 3725–3730, hep-ph/0206286.

Acknowledgments

At this point I would like to take the opportunity to thank those, who supported me during my PhD.

First of all I would like to thank Dr. Markus Diehl for providing this interesting topic, his supervision and continuous support.

I would like to thank Prof. Dr. Jochen Bartels for his co-supervision and for refereeing my thesis.

Thanks a lot to Alessandro Bacchetta, Dirk Brömmel and Wolfgang Kugler for proof-reading my thesis and for many fruitful discussions and helpful suggestions. Many thanks to Dirk and Wolfgang for their continuous support regarding computer related problems.

Special thanks to my family for their mental support during the whole time and to Sonja Birnschein for her trust in me and sharing my problems and happiness during my PhD.

I am very thankful to Dirk for spending the whole time with me, for his patience, support and love.